# UNDERSTANDING AND QUANTIFYING IMPACTS OF THE CONTINUUM ON NUCLEAR STRUCTURE

By

Joshua Wylie

A DISSERTATION

Submitted to
Michigan State University
in partial fulfillment of the requirements
for the degree of

Physics — Doctor of Philosophy

2025

## ABSTRACT

With the opening of new facilities, such as the Facility for Rare Isotope Beams, exotic nuclei will be increasingly accessible. Many exotic nuclei are strongly coupled to the continuum resulting in interesting structure formations, such as halo nuclear states or nuclear resonances.

In this thesis, the Gamow Shell Model framework is used to describe nuclei as Open Quantum Systems. This framework is a configuration-interaction shell model implemented in the Berggren basis which includes bound, resonant, and scattering states on equal footing. Two case studies are presented to highlight the impact of continuum effects on nuclear structure. Spectroscopic Factors are calculated for $^{8,9}$C, $^{8}$B, $^{8,9}$Li, and $^{8}$He using a traditional Shell Model approach (ignoring the continuum) and the Gamow Shell Model. The results from both methods are compared and demonstrate Spectroscopic Factors in these nuclei are dependent on the continuum. The newly discovered ephemeral nucleus $^{9}$N will be presented, which is unique with over half of its nucleons lying in the continuum. A projection method will be outlined to extract the continuum effects from the Gamow Shell Model to understand and directly quantify the effects of continuum coupling. Finally, a new outreach and community engagement demonstration, designed to educate the general public about nuclear structure and decays, will be discussed.

This work is dedicated to all those who strive to make science and scientific education more accessible. Without your work, I may not be where I am today.

## ACKNOWLEDGMENTS

There are countless people who have been crucial in guiding me to where I am today. That being said, I would like to thank those that have made this PhD possible. First, I would like to thank my advisor, Witold Nazarewicz, for his guidance, patience, and support. I am grateful for all the knowledge he has shared with me throughout this process, and he has instilled in me an appreciation for scientific rigor. Although initially intimidating, I have come to sincerely appreciate and value his challenges and questions, as they have pushed me to be a better scientist.

I would also like to thank my committee members: Filomena Nunes, Paul Guèye, Metin Aktulga, and Johannes Pollanen for their support and encouragement throughout my PhD. I would also like to thank Paul in particular for his unending support and investment in my future career, especially during the end of my PhD.

Although he was not an official advisor, I would like to thank Simin Wang (王思敏) for being an excellent secondary advisor and mentor to me throughout the past six years. From frequently coming into your office to emailing you in the middle of the night, I appreciate your willingness to answer my questions. Without your kindness and patience, this endeavor would have been much more difficult and overwhelming. I am also sincerely grateful to Nicolas Michel for both his technical support and his French language assistance, without which, I would have been in peril. From my time in Caen, I would like to thank Marek Płoszajczak, David Cardona Ochoa, and Alan Cruz Dassie for welcoming me and all of the helpful discussions.

Of course, I also appreciate everyone who has been a part of the research group and listened to my confused ramblings and helped me to refine and improve my work. Daniel, Eric, Kyle, and Pablo, I appreciate your willingness to offer help at a moment's notice, espe-

cially for this thesis. I would also like to thank Ante, Sudhanva, Yuanzhuo (远卓), Sylvester, Xingze (兴泽), and Josh for their support. Lastly, I would like to thank the students in the group (current and former): Aaron, An, Andrew, Bailey, Josh, Landon, Lauren, Maxwell, Mengzhi (孟之), Mookyong, and Tong (通) for their support and encouragement.

I would also like to thank all of the other wonderful friends I have made along the way: Andy, Andy, Bob, Bryan, Cami, Cavan, David, Jordan, Kelly, Lexi, Mo, Nick, Patrick, Pierre, Richard, Senora, and Sheng. To all of the Mid Michigan Runners, thank you for the encouragement and welcome distractions from physics. A special thanks to Carissa, Hannah, and Julia for being the most fantastic friends and great people to weather the bad, sad, and pandemic times with. Without you, these six years would not have been nearly as joyful.

To my family, thank you for your support and encouragement both before and during this time. I'm especially grateful to my parents, Carol and Eric, for pushing me to always be my best self. And to my Aunt Cathy and Uncle Brad, thank you for being available and supporting me throughout my entire university education. I am confident that this is the end of my educational journey; but if that were to change, I know you would be there to rely on.

I would also like to thank my partners parents, Ed and Linda, who have welcomed me into their family and encouraged me throughout this process. I extend the biggest thanks to my partner, Renee, who has been kind, understanding, and patient with me, especially while I finished this thesis. You make the bad days better, you keep me focused and motivated, and make me want to be better every day. I look forward to what comes next!

## TABLE OF CONTENTS

# Chapter 1. Introduction

Nuclear physics is a broad discipline ranging from the use of radioisotopes in medical applications to probing fundamental symmetries with atomic nuclei [1]. Underlying this broad range of topics is a dependence on nuclear structure information. While experimental data exists for approximately 3000 known isotopes [2, 3], there are many more unknown nuclei [4]. Predicting behaviors for such unknown nuclei, nuclear structure models are required. In this work, we are focused on an Open Quantum System (OQS) approach which is implemented via the Gamow Shell Model (GSM) [5]. First, we will focus on defining general nuclear attributes important to the discussions within this thesis.

## 1.1 Nuclear Structure Overview

Nuclei are self-bound clusters of nucleons which interact with each other to produce emergent phenomena. Some of these phenomena are universal to all nuclei, such as binding energy, while others, such as magic numbers and nuclear halos, appear only for particular nuclei [6, 7]. Nuclear instability must be properly represented since the mechanisms of decay are intrinsically tied to their structures.

A general quantity used to explain nuclear instability with respect to particle emission threshold is the $Q$-value. This value denotes the energy associated with removing the indicated particle(s); for example, removing one neutron $Q_n$, two protons $Q_{2p}$, or an alpha particle $Q_\alpha$. $Q$-values for one and two-nucleon decays are equal to the negative separation energy [8]. Fig. 1.1 depicts the various $Q_{n,p}$ and $Q_{2n,2p}$ values for the lithium isotopic chain; where positive ($^5$Li) and negative ($^6$Li) values correspond to prompt particle emission or a bound state, respectively. Nuclear states with energies near or above threshold will be ideal OQS candidates as these systems can be dominated by coupling to decay channels.

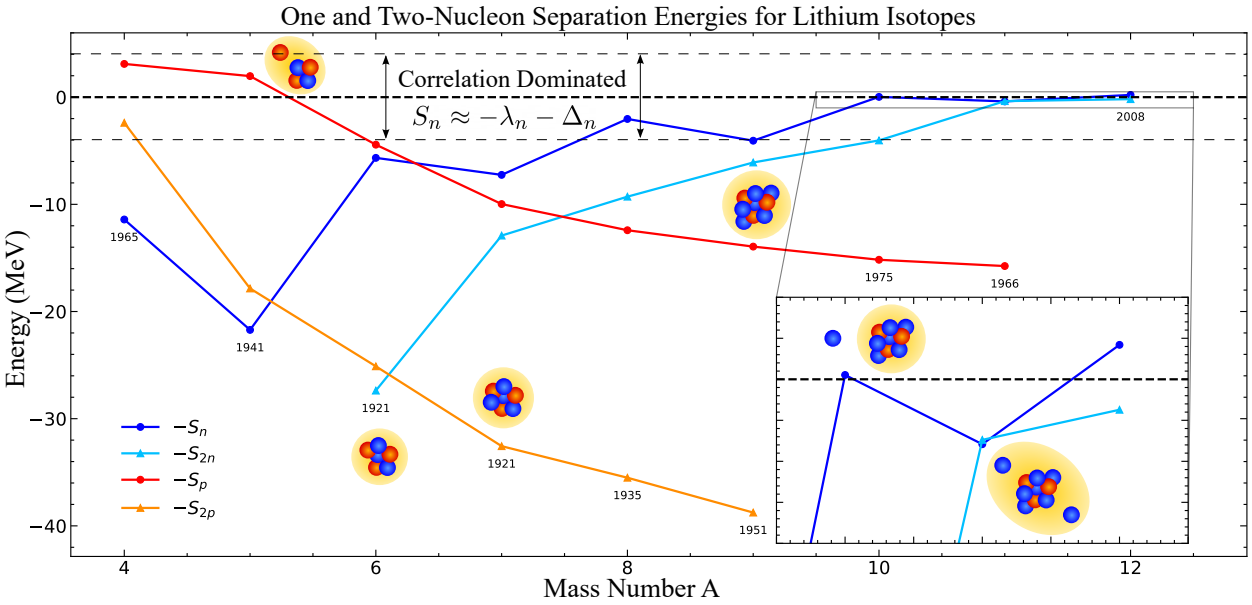


Figure 1.1: Illustration of openness in nuclear systems and the emergence of exotic phenomena at energies closer to threshold. We schematically show various isotopes of lithium ranging from a proton-resonance $^{5}$Li to neutron-unbound $^{10}$Li to two-neutron halo $^{11}$Li. Year discovered is presented for each isotope.

Describing nuclear structure requires proper treatment of all interacting nucleons in a many-body formalism, but many systems cannot be exactly calculated with current computational resources and require approximations. Depending on the region of the nuclear chart one is working in, the proper choice of model is essential, as some start from a more microscopic approach while others make assumptions to reduce dimensionality. In the lighter region of the nuclear chart ($Z \leq 20$) the widely-used theoretical approaches are *ab initio* or configuration-interaction Shell Model (SM)-based methods [9]. While each are useful in their own right, in this thesis we will focus on a variant of the SM as outlined in Sec. 2.2.

To calculate nuclei within the shell model, we define a nuclear core to which valence nucleons are added. Observables can then be calculated relative to this inert core. For example, calculated nuclei with positive $Q$-values relative to the core, or a larger subsystem, would indicate the presence of spontaneous nucleon emission for a chain of nuclei. These

particle emitting systems for a variety of emissions $\eta$ can be calculated as

$$Q_\eta = BE(N_{\text{residue}}, Z_{\text{residue}}) - BE(N, Z) \geq 0 \tag{1.1}$$

using the binding energy of the residual nucleus and decaying system respectively. Chains of nucleon emitters exist along specific isotopic and isotone lines, and are identifiable with respect to a residue. For example, there is a well-known chain of proton-emitting nuclei at the $N = 2$ isotone, relative to a $^4$He core, with $Q$ thresholds ranging from $Q_{1p}$ to $Q_{4p}$, for $^5$Li and $^8$C, respectively. Nuclei existing along these ridges are unstable and their lifetimes ($T_{1/2}$) are associated with the decay width of a state $\Gamma$:

$$T_{1/2} = \frac{\hbar \ln 2}{\Gamma}. \tag{1.2}$$

Nuclei existing in these regions can be especially challenging for some nuclear structure models which do not naturally include decays, such as a traditional SM. This dilemma motivates the need for a formalism which treats both structure and continuum states explicitly, and in our case, is accomplished in GSM.

## 1.2 Closed versus Open Quantum Systems

Quantum-mechanical systems can be divided into two groups: Closed Quantum Systems (CQS) and OQS. CQS-type problems treat an object as a completely isolated system whose properties cannot be affected by external factors. OQS-type problems allow for a system to be affected by its environment and can produce new emergent behaviors, contrary to CQS. Generally, one may recognize an OQS by identifying an isolated quantum system that undergoes an irreversible process after coupling to the environment [10]. OQS are featured

across physics from macroscopic (molecular) systems to mesoscopic (nuclear) systems and have shared phenomena in the form of resonances and scattering states. A specific example of coupling with the environment that causes alterations in the system considered is the decoherence of qubits in quantum computers [11].

In the nuclear physics context, a nucleus (the system) can undergo decay by emitting a nucleon (the irreversible process) after coupling to the continuum (the environment). OQS phenomena vary from system to system and are dependent on the environment to different degrees. The development of any techniques describing OQS can be extended in a variety of fields, but nuclei are able to produce emergent behaviors seen in larger systems while retaining far fewer degrees of freedom. One such example of interdisciplinary OQS phenomena accessible in nuclei is superradiance [12] which was first discovered in quantum optics [13]. Nuclei also are unique due to the presence of different species of fermions, and the interactions between these fermions is the interplay between strong and electro-weak forces. An example of probing unique physics with nuclei is tackling the question of non-exponential decay [14].

Theories that consistently treat nuclear OQS systems will use a formalism incorporating bound and scattering (continuum) states simultaneously [5, 15]. Experimentally, these OQS will have a resonance structure or other collective features that appear near or above threshold. For a more approachable definition of a resonance, one could define it as a specific energy which produces a substantial increase in the cross section of a nucleus, or the probability of an interaction occurring. Thus, a resonance is a local band in an energy spectrum where a projectile can alter the structure of a nucleus without being bound to or knocking another particle from the target. Essentially, a resonance is a feature in a nucleus where the lifetime is extended beyond what one might typically assume to be short-lived in the

scattering process. Additionally, understanding this continuum coupling would allow better understanding into the preference in decays of unbound states [16] as a decay could be considered the time inverse of a capturing reaction.

Although nuclear resonances like $^5$Li are the systems most commonly associated with OQS, in reality the entire nuclear landscape should be describable with one coherent framework. If one has a Hamiltonian capable of describing one nucleus, from an OQS perspective, the same Hamiltonian should also be able to describe any other nucleus by successive chains of operations like particle capture and decay [17]. A key region where these dynamics are most clearly at play are in the correlation dominated section of Fig. 1.1 around threshold. Here, as indicated by the equation $S_n \approx -\lambda_n - \Delta_n$, separation energies are on the same order of magnitude as the single-particle (s.p.) fields $\lambda_n$ and many-body effects like pairing $\Delta_n$ [17], leading to competition between these effects. Emergence of other features like nuclear halos are also associated with the competition between coupling to the environment and coupling between particles inside the system [18]. For this reason, we will explore various exotic phenomena using a continuum-informed model, GSM.

# Chapter 2. Formalism

The formalism of GSM is fundamentally similar to the implementation of the traditional SM. Where GSM differs is most obviously in its choice of basis, the Berggren basis [19], whereas standard SM codes might use a harmonic-oscillator (HO) basis. First, we outline the motivation for the Berggren basis and the necessary formalism.

## 2.1 Berggren Basis

As already highlighted, an OQS naturally allows the formation of metastable states that require decay by particle emission so an OQS must include outgoing scattering states. We shall assume that outgoing states will not be affected by short-range nuclear forces and they propagate as a plane wave when the particle is far from the residual nucleus. Ordinary quantum mechanics tends to be formulated in a Hilbert space where Hamiltonians are Hermitian, but it is not straightforward to implement decay processes in this formalism. To address this tension, Gamow extended the formalism to the complex plane by introducing an imaginary damping term ($\Gamma$) to the energy to address $\alpha$-particle emission [20]. The states in this extended framework belong to a Rigged Hilbert space [21–23] which includes states that obey the desired outgoing boundary conditions. Rigged quantum mechanics is a natural framework for intrinsically irreversible processes arising from the Hamiltonian itself, as opposed to extrinsic irreversible processes which occur due to environmental coupling and describable in a Lindbladian approach [22]. The development of this formalism is supported by the assumption of a bulk exponential decay property where the complex energy and half-life are related by:

$$E = E_0 - i\frac{\Gamma}{2} \tag{2.1}$$

with energy $E_0$ and decay width $\Gamma$ as discussed surrounding Eq. 1.2.

Berggren expanded on this framework [19] by including Siegert's resonance definition [24] and used the asymptotics for a neutral particle:

$$\mathcal{O}_l(kr) \sim e^{i(kr-\frac{l\pi}{2})}, \quad \mathcal{I}_l(kr) \sim e^{-i(kr-\frac{l\pi}{2})} \tag{2.2}$$

for outgoing and incoming waves respectively. By imposing the boundary conditions:

$$u(0) = 0; \quad u(a)\mathcal{O}_l'(ka) - u'(a)\mathcal{O}_l(ka) = 0, \quad \text{or} \quad \tilde{u}(a)\mathcal{I}_l'(\tilde{k}a) - \tilde{u}'(a)\mathcal{I}_l(\tilde{k}a) = 0, \tag{2.3}$$

where $a$ corresponds to the radius at which the nuclear potential is effectively zero (for neutrons) or has long-range Coulomb behavior (for protons), the resonant nature of the system is respected [19]. Furthermore, this formulation modifies the general properties of our complex resonant states:

$$\tilde{k} = -k^*, \quad \tilde{u}(r) = u^*(r), \quad \text{and} \quad k = \kappa - i\gamma \tag{2.4}$$

with $\kappa$ and $\gamma$ being real and imaginary momentum terms, respectively. It should be noted that there are challenges when using this formalism, mainly that the states can increase exponentially and are not normalizable. Various approaches exist for normalizing such states, see Ref. [5] for details. From this point onward, our complex energy will be represented as $E$ and complex momentum $k$, and the conjugation within the Berggren basis will be represented by a tilde.

### 2.1.1 One-body states

For the current formalism, we will work in a spherically symmetric basis. This maintains many symmetry advantages, such as easy handling of the angular momentum and spin. Decomposing the one-body wave function is standard (including spin $\chi_{s,m_s}$)

$$\psi(r,\theta,\phi) = R(r)\left[Y_{\ell,m} \otimes \chi_{s,m_s}\right]^{j}_{m}. \tag{2.5}$$

Taking advantage of the system symmetries for quantum numbers, the general one-body wave function can be rewritten as [8]

$$\psi(n,\ell,j,m_j,\vec{r}) = \frac{u_\psi(n,\ell,j,r)}{r} \sum_{m_\ell,m_s} \langle \ell m_\ell s m_s | j m_j \rangle \, Y_{\ell m_\ell}(\theta,\varphi)\chi_{s,m_s}; \tag{2.6}$$

where the angular terms are decomposed into the possible components with correct angular momentum coupling - e.g. those with $\vec{j} = \vec{\ell} + \vec{s}$ and $m_j = m_\ell + m_s$ [8].

Due to the non-Hermitian nature of the Gamow resonant states (Eq. 2.4) in the complex plane, we illustrate possible solutions to the time-independent Schrödinger equation in Fig. 2.1. The parameters used can be found in Tab. 2.1 and follow with Ref. [5]. Bound wave functions are still normalized in the conventional sense as they are square integrable. An important distinction between different states is their behavior in the asymptotic region. For example, the narrow resonance in Fig. 2.1a appears to have a similar profile to the well-bound wave function, yet when extending to a larger radius, we see oscillations appear in its tail (seen in Fig. 2.1b). Conversely, the loosely bound wave function appears to not be well-localized, but we see its convergence at a larger radius. Broad resonances have extended localizations before being quickly dominated by their diverging behavior. Lastly, antibound

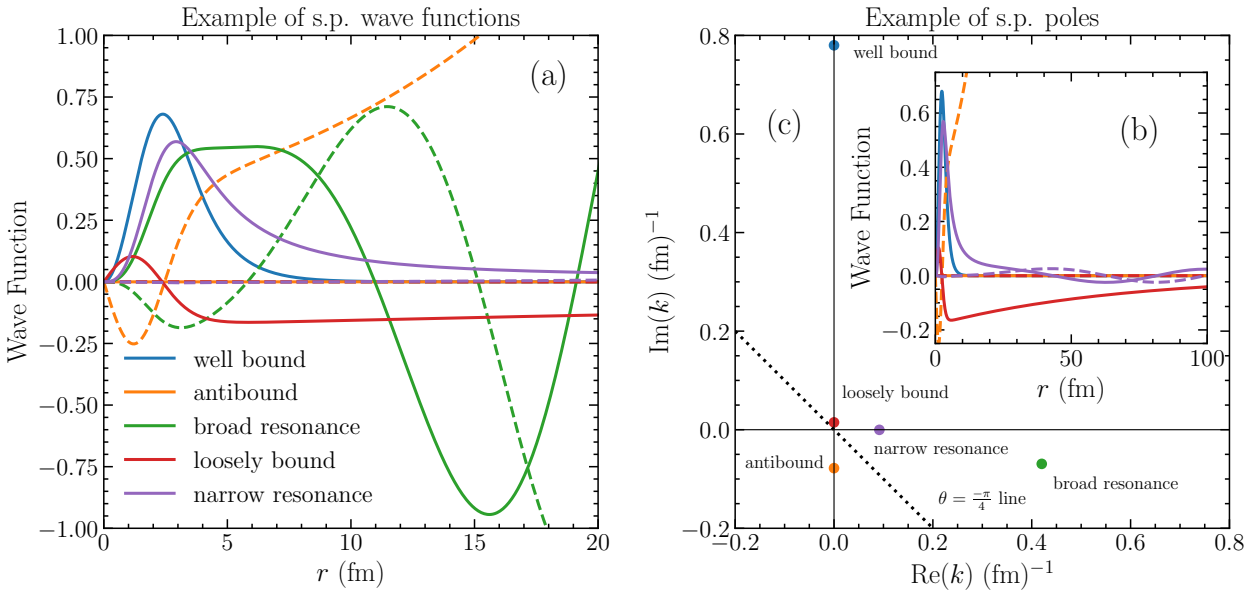


Figure 2.1: (a) Different classifications of one-body wave functions with real (solid lines) and imaginary (dashed lines) parts. (b) Radial extension of one-body wave functions (similar to (a)) for well bound, loosely bound, narrow resonance, and antibound states. (c) The locations in the complex plane of the presented wave functions in panel (a).

Table 2.1: Parameters used to generate the corresponding s.p. states in Fig. 2.1. All wave functions are for a neutron in a one-body potential of $A = 12$, diffuseness $d = 0.65$ fm, and radius $R_0 = 3$ fm along with the specified Woods-Saxon depth $V_0$ and Spin-Orbit potential strength $V_{SO}$. Additional information can be found in Chapter 2 of Ref. [5].

| Type | $V_0$ (MeV) | $V_{SO}$ (MeV) | State | $k$ (fm)$^{-1}$ |
|---|---|---|---|---|
| Well Bound | 50 | 7.5 | $0p_{3/2}$ | (0, 0.7799) |
| Loosely Bound | 43 | 0 | $1s_{1/2}$ | (0, 0.0149) |
| Narrow Resonance | 63 | 7.5 | $0d_{3/2}$ | (0.0918, -0.0003) |
| Broad Resonance | 50 | 7.5 | $0d_{3/2}$ | (0.4202, -0.0693) |
| Antibound | 40 | 0 | $1s_{1/2}$ | (0, -0.0780) |

(also called virtual) states have no sense of localization and diverge immediately. These states naturally emerge in a potential well without a barrier, leading to an enhancement in the cross section [25, 26].

States can be more clearly separated by using the energy-momentum relation $E \propto k^2$.

Bound states (positive imaginary $k$) are real and exist on the negative energy axis while scattering states, which are also real, exist on the positive energy axis. These states lie on the first, physical, Riemann Sheet. Resonant states and antibound states are complex energies and lie on a second, sometimes called non-physical, sheet. These states can be accessed by a number of methods including a deformed contour.

### 2.1.2 Berggren Completeness Relation

In order to define the completeness relation for GSM, we first demonstrate the minor differences between a Berggren basis and the more traditional real-energy (Hermitian) completeness relation from basic quantum mechanics. Generally, states in a Hermitian Hamiltonian will be square integrable and normalizable. For non-square integrable states, a Dirac $\delta$ normalization may be imposed with the condition $2\pi C^{+}(k)C^{-}(k) = 1$ where $C^{\pm}(k)$ are constants determined by Jost functions

$$J^{\pm}(k) = \pm 2ikC^{\mp}(k) \tag{2.7}$$

which can be related to the Wronskian of $u(k,r)$ [5, 27, 28]

$$J^{\pm}(k) = u(k,r)u^{\pm\prime}(k,r) - u'(k,r)u^{\pm}(k,r). \tag{2.8}$$

Here, $u^{\pm}(k,r)$ represent the solutions to the radial Schrödinger equation following incoming or outgoing boundary conditions. Details can be found in Ref. [5] for both neutral and charged particles.

Since all states are orthonormal, a completeness relation can be defined. We focus on the

simpler case of an $\ell = 0$ neutron where we consider the integral [5]

$$I(K) = \int_0^K \frac{u(k,r)u(k,r')}{2\pi C^+(k)C^-(k)} dk. \tag{2.9}$$

Due to the momentum definition in Eq. 2.4, conjugation of states are invariant to $k \to -k$ thus

$$u(k,r) = u(-k,r), \quad u^{\pm}(k,r) = u^{\mp}(-k,r), \quad \text{and} \quad C^{\pm}(k) = C^{\mp}(-k). \tag{2.10}$$

By taking advantage of these symmetries, integration bounds can be rewritten as [5, 27, 28]

$$I(K) = \int_{-K}^K \frac{u^+(k,r)u(k,r')}{2\pi C^-(k)} dk. \tag{2.11}$$

Knowing bound state poles only lie on the imaginary $k$ axis in the complex $k$-plane, this integral can be simplified with Cauchy's theorem. Introducing a contour integral along the upper half plane separates the residues from the non-resonant scattering continuum. Details can be found in Ref. [5, 27, 28], but the result is the Berggren completeness relation [5]

$$\sum_n u_n(r)u_n(r') + \int_{\mathcal{L}^+} u_k(r)u_k(r')dk = \delta(r - r'). \tag{2.12}$$

The contour $\mathcal{L}^+$ corresponds to the complex-energy scattering states, and the discrete $u_n(r)$ are bound and resonant states inside $\mathcal{L}^+$. Fig. 2.1 presents the different components which make up the poles of the $S$-matrix and are present in Eq. 2.12.

### 2.1.3 Numerical Implementation

Retaining the representation of the continuum in practical applications can be difficult as current computers cannot represent an infinite continuum of states. The contour integral contributions to the completeness relation in Eq. 2.12 is discretized as

$$\int_{\mathcal{L}^+} u(k,r)u(k,r')dk \simeq \sum_{i=1}^{N_d} u_i(r)u_i(r') \tag{2.13}$$

where $u_i(r) = \sqrt{\Delta_{k_i}}u(k_i,r)$ and $\Delta_{k_i}$ is the discretization step weight at specific momenta [5]. By ensuring that these $u_i(r)$ are orthonormal, the discretized Berggren completeness relation can be written as

$$\sum_n u_n(r)u_n(r') + \sum_{i=1}^{N_d} u_i(r)u_i(r') \simeq \delta(r-r') \tag{2.14}$$

In general, the analytic form of Eq. 2.12 would imply any arbitrary contour choice is sufficient as long as it encompasses the desired poles. With the discretized form, contours should be chosen such that they are not too close to the pole where numerical noise might lead to unwanted instability [5, 29–31]. However, the model space dimension $d$ is directly tied to the number of discretization points chosen by

$$d \propto N_s^{N_v} \tag{2.15}$$

where $N_s$ and $N_v$ are the number of states and number of valence nucleons respectively [32]. A tension exists between the number of points required for good numerical completeness and the desire to keep model spaces within a calculable range. To optimize the computational resources required, one can reduce the number of discretization points $N_d$ for the contour

or minimize the number of states considered $N_v$. By carefully choosing our contour for each partial wave $(\ell, j)$, we can minimize the number of states needed while maintaining computational stability and fidelity.

## 2.2 Gamow Shell Model

For the Berggren basis to be useful in a SM or configuration-interaction implementation, the one-body completeness relation must be generalized to a many-body form. This is a result of SM wave functions being many-body vectors, not simple one-body wave functions. In order to make the familiar Dirac notation useful in the GSM context, we must make some modifications.

### 2.2.1 GSM Completeness Relation

In order to be more amenable to SM formulations, we will work with $N$-body Slater determinants (SDs)

$$|\Psi_n\rangle = |\psi_{i_1}, ..., \psi_{i_A}\rangle = \begin{vmatrix} \psi_{i_1}(\vec{r}_1) & ... & \psi_{i_1}(\vec{r}_A) \\ \vdots & \ddots & \vdots \\ \psi_{i_A}(\vec{r}_1) & ... & \psi_{i_A}(\vec{r}_A) \end{vmatrix} \tag{2.16}$$

built from the orthonormalized one-body states ($|\psi_i\rangle$) that make up our Berggren ensemble. Therefore, any SD built from a set of states $|\psi_k\rangle$ may contain the bound, decaying resonance, and scattering s.p. states from the poles and contour. The generalization of the one-body completeness relation to a many-body representation is [5]:

$$\sum_n |\Psi_n\rangle \langle\tilde{\Psi}_n| \simeq I, \tag{2.17}$$

and the derivation starting from the real-energy Newton completeness relation can be found in Ref [5, 27]. Different state conjugations ($\tilde{\Psi}$) are implemented than in the Hilbert space

formulation as discussed in Eq. 2.4. These tilde eigenstates represent effects from the time-reversal operator [33], and the physical connection is that particle-capturing states are represented as bras and particle-emitting states as kets. Conjugate states belong to the dual space vectors, see Ref. [5, 34]. By using Eq. 2.17, we can check our system through the sum over all squared amplitudes of each configuration (not the squared absolute values like in the traditional SM)

$$\sum_n c_n^2 = 1. \tag{2.18}$$

This serves as a useful check to ensure any calculations are being handled properly.

### 2.2.2 GSM Hamiltonian

The general form of the GSM many-body Hamiltonian [31] is

$$H = \sum_i^{N_{\rm val}} \left[ \frac{\vec{p}_i^2}{2\mu_i} + U_c(i) \right] + \sum_{i=1, j>i}^{N_{\rm val}} \left[ V_{i,j} + \frac{\vec{p}_i \vec{p}_j}{M_c} \right] \tag{2.19}$$

with $N_{\rm val}$ being the number of valence nucleons and $\mu_i$ and $M_c$ being the reduced mass of the nucleon and mass of the core respectively [5]. One-body effects are accounted by the core-nucleon potential $U_c$ and two-body effects via valence nucleon interaction $V_{i,j}$. To eliminate center-of-mass motion energy contributions, the Cluster Orbital Shell Model framework (COSM) is used in Eq. 2.19 to provide a translationally invariant framework [5, 31].

The following Woods-Saxon (WS) form is used for the core-nucleon potential

$$U_c(r) = V_0 f(r) - 4V_{\ell s} \frac{1}{r} \frac{df(r)}{dr} \vec{\ell} \cdot \vec{s} + U_{\rm Coul}(r) \tag{2.20}$$

where $f(r) = -[1 + \exp{(r - R_0)/a}]^{-1}$. For neutrons, the one-body potential can be simpli-

fied by setting $U_{\rm Coul} = 0$ and obtaining

$$U_c(r) = \frac{-V_0}{1+\exp\left(\frac{r-R_0}{a}\right)} - 4V_{\ell s}\frac{1}{r}\frac{\exp\left(\frac{r-R_0}{a}\right)}{a\left[1+\exp\left(\frac{r-R_0}{a}\right)\right]^2}\vec{\ell}\cdot\vec{s} \tag{2.21}$$

with $\vec{\ell}\cdot\vec{s} = j(j+1) - \ell(\ell+1) - \frac{3}{4}$. Similarly, the same form can be used for protons along with the addition of the Coulomb term for a uniformly charged sphere of radius $R_p$

$$U_{\rm Coul}\left(r\right) = \begin{cases} \frac{Ze^2}{2R_p}\left(3 - \left(\frac{r}{R_p}\right)^2\right) & r \le R_p \\ \frac{Ze^2}{r} & r > R_p \end{cases}. \tag{2.22}$$

There are many different choices for two-body potentials in GSM, but in the context of this thesis, we only use the valence nucleon-nucleon interaction

$$V = V_c + V_{LS} + V_T + V_{\rm Coulomb} \tag{2.23}$$

with the central ($c$), spin-orbit ($LS$), tensor ($T$), and Coulomb terms. The first three terms are based on the Furutani-Horiuchi-Tamagaki (FHT) force [35, 36]. These are based on spin-isospin projectors ($\Pi_{ST}$)

$$\begin{aligned} V_c(r) &= V_c^{11} f_c^{11}(r)\Pi_{11} + V_c^{10} f_c^{10}(r)\Pi_{10} + V_c^{00} f_c^{00}(r)\Pi_{00} + V_c^{01} f_c^{01}(r)\Pi_{01}, \\ V_{LS} &= \left(\vec{L}\cdot\vec{S}\right) V_{LS}^{11} f_{LS}^{11}(r)\Pi_{11}, \\ V_T(r) &= S_{ij}\left[V_T 11 f_t^{11}(r)\Pi_{11} + V_T^{10} f_t^{10}(r)\Pi_{10}\right], \end{aligned} \tag{2.24}$$

where $\vec{L}$ is the relative orbital angular momentum, $\vec{S} = (\vec{\sigma_i} + \vec{\sigma_j})/2$, and $S_{ij} = 3(\vec{\sigma}_i\cdot\hat{r})(\vec{\sigma}_j\cdot$

$\hat{r}) - \vec{\sigma}_i \cdot \vec{\sigma}_j$ [37]. The distance between nucleons $i$ and $j$ is represented by $r_{ij}$ and $\hat{r} = \vec{r}_{ij}/r_{ij}$. Fundamentally, this interaction is based on a sum of Gaussians approach to include effective representation of a long-range term to represent pion exchange potentials and a short-range hard core term [37].

When using the FHT interaction, we note that three of the seven available terms ($V_c^{10}$, $V_c^{01}$, and $V_T^{10}$) appear at leading order in effective field theory arguments with the remaining being higher order terms [31]. When attempting to adjust these parameters for optimization, including only leading order [31] or all [37] terms may provide better reproduction of spectra, depending on the application. Regardless of the inclusion of higher order terms, this interaction has been used to successfully calculate different nuclear systems [31, 37–40].

# Chapter 3. Spectroscopic Factors and the Continuum

Experimentally probing internal features of nuclei is a difficult process, but the data obtained can elucidate significant physical insight. Measured cross sections of different direct reactions (without forming any intermediate state) is one such tool that can be used to study nuclear phenomena. Some quantities discussed commonly by nuclear physicists are non-observables (or sometimes called unobservables) and are instead dependent on the chosen framework, see Ref. [41]. Single-particle energies are such quantities originating from a mean-field (shell model) level and dictate the ordering of energy levels for a specific calculation. In the context of compatible models, these non-observables can be incredibly useful especially if tied to an approximate experimental value.

Spectroscopic factors (SFs) are another non-observable quantity which are inferred through ratios of cross section data. The SFs themselves can be derived via the number operator [8] under Racah [42] and Wigner's convention, yet for the current discussion, it is more useful to discuss SFs in the context of radial overlap integrals. The radial overlap integral can be expressed as [5]:

$$I^{a}_{bc;\ell j}(r) = \frac{1}{\sqrt{2J_a+1}} \sum\!\!\!\!\!\!\int_{\mathcal{B}} \left\langle \widetilde{\Psi^{J_a}_{a}} \left\| a^{\dagger}_{\ell j}(\mathcal{B}) \right\| \Psi^{J_b}_{b} \right\rangle \langle r\ell j \mid u_{\mathcal{B}} \rangle \tag{3.1}$$

where we consider the overlap between a decaying nucleus $a$ and its products $a \to b + c$, ultimately summing over all s.p. basis states $\mathcal{B}$. SFs are then defined as the squared norm of Eq. 3.1 [5]:

$$S = \frac{1}{2J_a+1} \sum\!\!\!\!\!\!\int_{\mathcal{B}} \left\langle \widetilde{\Psi^{J_A}_{A}} \left\| a^{\dagger}_{\ell j}(\mathcal{B}) \right\| \Psi^{J_{A-1}}_{A-1} \right\rangle^2 . \tag{3.2}$$

An additional advantage to these definitions are that using a complete set of Berggren basis states results in the SF being independent to the choice of basis, whereas other forms have basis dependence [8, 43, 44]. These SFs can be used to calculate theoretical cross sections for direct reactions [5, 43–45] and for GSM specifically

$$\sigma = \sum_{n\ell j m_j} S_{n\ell j m_j} \sigma_{\text{s.p.}}^{n\ell j m_j}. \tag{3.3}$$

These formulations are tied to the notion of the spectator approximation or the approximation that reactions are simply an $A-1$ system with a lone nucleon outside.

This chapter contains my contributions to a larger work focusing on the impact of the continuum on SFs [46].

## 3.1 Discrepancy Between Experiment and Theory

Despite being a non-observable quantity, SFs are inferred using the ratio of experimental to theoretical inclusive cross sections by [44, 47, 48]

$$R_s = \frac{\sigma_{\text{exp}}}{\sigma_{\text{th}}}. \tag{3.4}$$

Clearly, model dependence enters the calculation depending on how $\sigma_{\text{th}}$ is obtained. Regardless of the choice of the model, one could reasonably assume that these ratios would deviate about some mean value for all reaction probes across different nuclei for the chosen model. Any deviations in could be attributed to poor reproduction of specific physical behaviors within the chosen model. Indeed, this exact behavior is seen for the electron-induced knockout reactions $\left(e, e'p\right)$ for the stable nuclei considered in Fig. 3.1. However, in a sequence of papers [44, 47, 50] it was shown that, for knockout reactions in particular, there is a system-

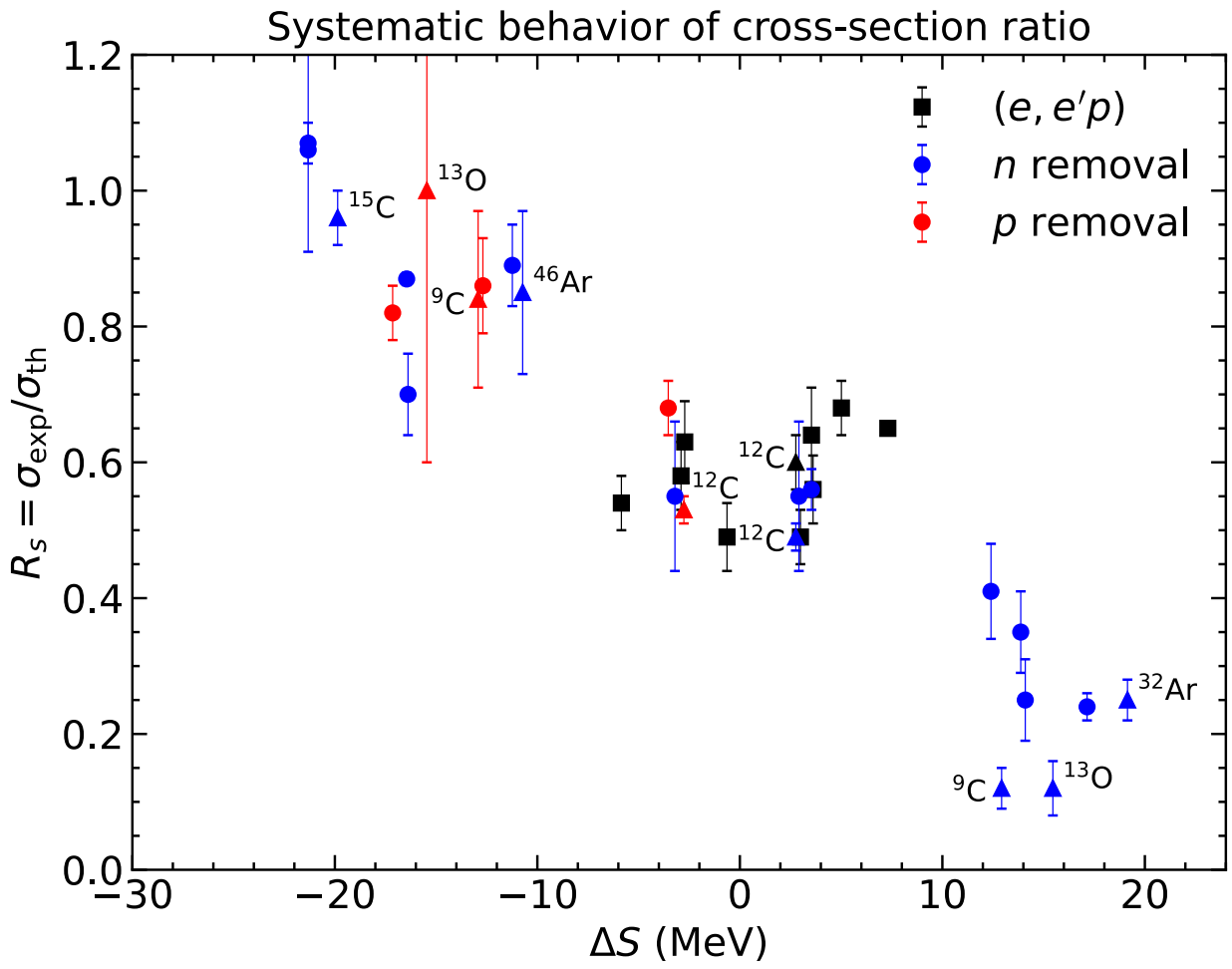


Figure 3.1: Compiled data of different $R_s$ using data in [44, 49]. We specify select nuclei (triangles) to highlight specific features, yet all available nuclear data can be found in Ref. [44].

atic linear dependence in $R_s(\Delta S)$, shown in Fig. 3.1. The quantity $\Delta S$ is calculated as the difference between the separation energy of the particle removed and its opposite species, a representation of isospin asymmetry [44, 51, 52]. For proton removal $\Delta S = S_p - S_n$ and for neutron removal $\Delta S = S_n - S_p$.

Focusing on either extreme of $\Delta S$, one can notice commonalities between the highlighted nuclei in Fig. 3.1. For exotic nuclei, like $^{9}$C, the values of $R_s$ for proton and neutron knockout span a large range unlike the stable nuclei like $^{12}$C. Additionally, when considering only a particular type of reaction, say neutron knockout, we can identify two isotopes $^{32}$Ar and $^{46}$Ar with vastly different $R_s$ seemingly tied to whether the removed neutron was in the minority or majority nucleon species [51, 52]. Lastly, some nuclei such as the halo nucleus $^{15}$C [53] are not exotic nuclei with strong isospin asymmetry, yet $^{15}$C could be considered as a core-spectator system of $^{14}$C+$n$ with the core being a magic nucleus of $N = 8$.

The source of the trend in $R_s$ is still under debate, but it is at least partially due to structural dependence on the nucleon removed. Specifically, the validity of the spectator approximation for exotic states is the center of our focus. For many cases, this approximation is reasonable particularly when removing weakly-bound nucleons from their larger system [45]. One can recognize that a large overlap indicates that the parent and daughter maintain a largely consistent structure independent of the effects of the removed particle. Removing well-bound nucleons on the other hand may require strong alterations to the original parent configuration, making the daughter's structure different and producing a small overlap. In each case, the nuclei with strong differences in the proton and neutron separation energies have $R_s$ values either near one or suppressed strongly towards zero. Nuclei with large $\Delta S$, tend to have a higher asymmetry of protons to neutrons and, in the case of light nuclei, these would be deemed "exotic" due to their shorter half-lives. At the extreme ends of the trends

identified in Fig. 3.1, many of the nuclei are located near dripline regions.

## 3.2 Continuum Impact on Spectroscopic Factors

Considering nuclei near or beyond the driplines, an OQS formulation is essential due to continuum dependence of such systems. In GSM, these SFs are determined via the spectroscopic amplitude [54, 55]

$$\mathcal{A}_{\ell j}(k_p) = \frac{\langle \Psi_A || a^+_{\ell j}(k_p) || \Psi_{A-1} \rangle}{\sqrt{2J_A+1}}; \quad \mathcal{S}^2_{\ell j} = \sum\!\!\!\!\!\!\int \mathcal{A}^2_{\ell j}(k_p), \tag{3.5}$$

which describes similarity of a parent nucleus to its one-nucleon-removed daughter, just as the traditional SM formulation in Eq. 3.2. The formulation in Eq. 3.5 improves the structure representation from previous SM calculations since it includes physics associated with unbound states. To underscore why it is an improvement, we can contrast with known issues with well-localized bases that work for well-bound nuclear states, but not for weakly-bound systems without modification. An example focuses on the descriptions of $^{9-11}$Li with localized bases. For these nuclei, localized bases overbind the unbound $^{10}$Li and the $2n$ halo $^{11}$Li despite reproducing the structure of the well-bound $^{9}$Li subsystem [56, 57]. In this case, the importance of long-range dynamics has been demonstrated to resolve these issues [58]. These problems are addressed in GSM which can describe the unbound nature of the dripline systems like $^{10}$Li [31]. Although this is an oversimplified picture, the long distance wave function behavior can inadvertently be truncated using a localized basis, and this lack of long range components is thought to bind the system [56, 57]. In essence, we can better inform and represent states when choosing a basis that allows for natural occupations and avoids any possible discontinuities by treating all possible states on the same footing. Using the Berggren basis, this can be accomplished while including continuum degrees of freedom

in GSM which is contrary to the lack of a genuine continuum in a CQS representation.

## 3.3 Parameters and Model Space

To probe the effects of the continuum on SFs, we perform a series of calculations for specific nuclei which are likely to be dependent on the continuum such as $^{8}$C, $^{8}$B, and $^{9}$C. The choice of these nuclei is based on recent experimental evidence from Ref. [49]. Although GSM does not have explicit control over continuum coupling strength, we enforce openness of the system by applying truncations on the number of valence particles allowed in the scattering continuum. For our calculations, we start with a HO basis (no continuum coupling) in a *p*-shell model space and ultimately open the system using a full Berggren basis calculation in a *psd*-model space with all four valence particles allowed to occupy the continuum for $A = 8$ nuclei. Berggren-basis calculations using a resonant $0p_{3/2}$ basis state were also performed and are denoted with the subscript "res" to better capture effects tied to width [31]. The purpose of using a resonant pole is to highlight basis independence of the calculations.

To minimize the effect of core excitations, we selected $^{4}$He as the system core due to its tight binding. The GSM Hamiltonian is as defined in Sec. 2.2.2 using the standard WS with spin-orbit one-body interaction and the FHT two-body interaction. We used the calibrated parameters for *ps*-shell model space nuclei from Ref. [31] when performing the HO basis (SM analog) and *ps* Berggren basis calculations. We performed additional calculations with a *psd*-shell model space to explore the impact of higher $\ell$ states. For the $\ell = 2$ states the, same one-body parameters were used as in Ref. [31], but we readjusted the only non-zero two-body term for homogeneous valence nucleon systems ($V_{\eta}^{ST} = V_{c}^{01}$) until the ground state (g.s.) energy of $^{8}$C was within 0.2 MeV of the experimental value [2]. This is justified as the goal of this work is to best reproduce the $^{8}$C structure to adequately address continuum effects on

SFs. After determining our parameters for the two different model spaces in the proton-rich case, we applied the same parameters to the mirror nuclei $^{8}$He, $^{8}$Li, and $^{9}$Li. In all cases, the $A = 9$ nuclei are well-bound systems and were calculated allowing only two particles to occupy continuum states ($N_{\text{cont}} = 2$). Since we focused on the continuum impact on the daughter structure, the $A = 8$ systems were calculated with varying numbers of particles in the continuum (up to the maximum of $N_{\text{cont}} = 4$).

The model space used in this work [46] included pole states for $0p_{3/2}$, $0p_{1/2}$, and (when applicable) $0d_{5/2}$. For Berggren basis calculations, we use the standard three segment contour form of Eq. 2.17 and each segment was divided into five Gauss-Legendre points. The segment geometry was chosen to be $k_{\text{peak}} = 0.3$ fm$^{-1}$, $k_{\text{mid}} = 0.4$ fm$^{-1}$, and $k_{\text{max}} = 4$ fm$^{-1}$ with imaginary components being increased when needed for resonant systems. Fig. 3.2 shows the resulting spectra for each nucleus in the full possible model space, and the energies appear to be reasonably well reproduced despite the Coulomb energy difference between mirror nuclei.

## 3.4 Impact of Continuum Coupling Calculations

As discussed above, we study the effects of continuum coupling on wave function fragmentation for $A = 9$ nuclei through knockout of well-bound and weakly-bound nucleons. For isospin-asymmetric systems, the minority species nucleons will tend to be the well-bound nucleons while the majority species nucleons will be weakly-bound or even unbound. All SFs calculated are for parent g.s. to daughter g.s. transitions.

### 3.4.1 Minority Species Nucleon Removal

First focusing on the minority species removal, we can compute the SF for $^{9}\text{C}(3/2^{-}) \rightarrow ^{8}\text{C}(0^{+}) + n$ using the four different model spaces outlined in Sec. 3.3. HO-SM calculations only in-

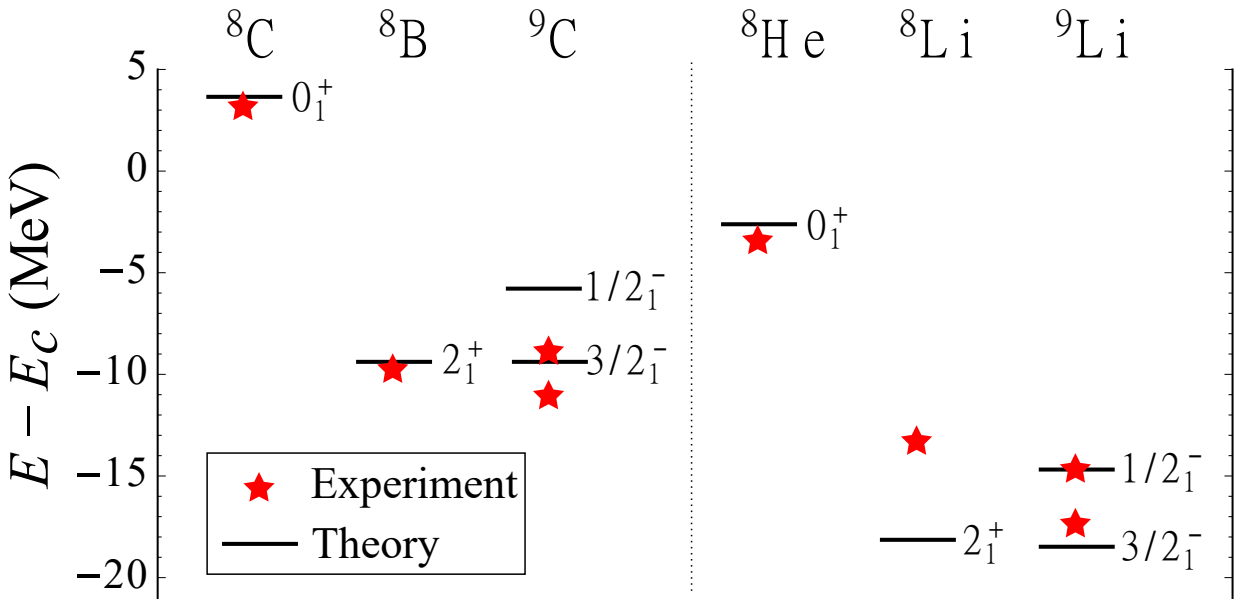


Figure 3.2: Energies of $^{8,9}$C, $^8$B, $^8$He, and $^{8,9}$Li calculated in GSM with the $psd_{\text{res}}$-model space. Figure taken from [46].

cluding $p$-poles produced a SF of $S^2 = 0.86$ whereas the GSM values range from $S^2 = 0.67$ for $ps$-shell to $S^2 = 0.48$ for $psd_{\text{res}}$-shell calculations. Similarly, for the knockout in $^9\text{Li}(3/2^-) \rightarrow ^8\text{He}(0^+) + p$ the SF ranges from $S^2 = 0.85$ for HO-SM to $S^2 = 0.48$ for $psd_{\text{res}}$-shell calculations. All SF values for the knockout of well-bound nucleons are presented in Table 3.1.

To understand the reduction of SFs with increasing continuum coupling, we focus on the changing structure across each model space. By comparing the wave function decomposition between HO-SM and GSM-$psd$ ($N_{\text{cont}} = 4$) in Fig. 3.3a, we can deduce the changes from continuum coupling. For $^8$C, we note the strong shift between HO-SM and GSM calculations where the pole locations shift slightly in energy, but the squared amplitude of the GSM occupations drop significantly. Moreover, the decrease in squared amplitude for pole configurations is then redistributed among continuum states. This change is unsurprising as $^8$C is a system beyond the proton dripline, which decays by two steps of $2p$ emission, and

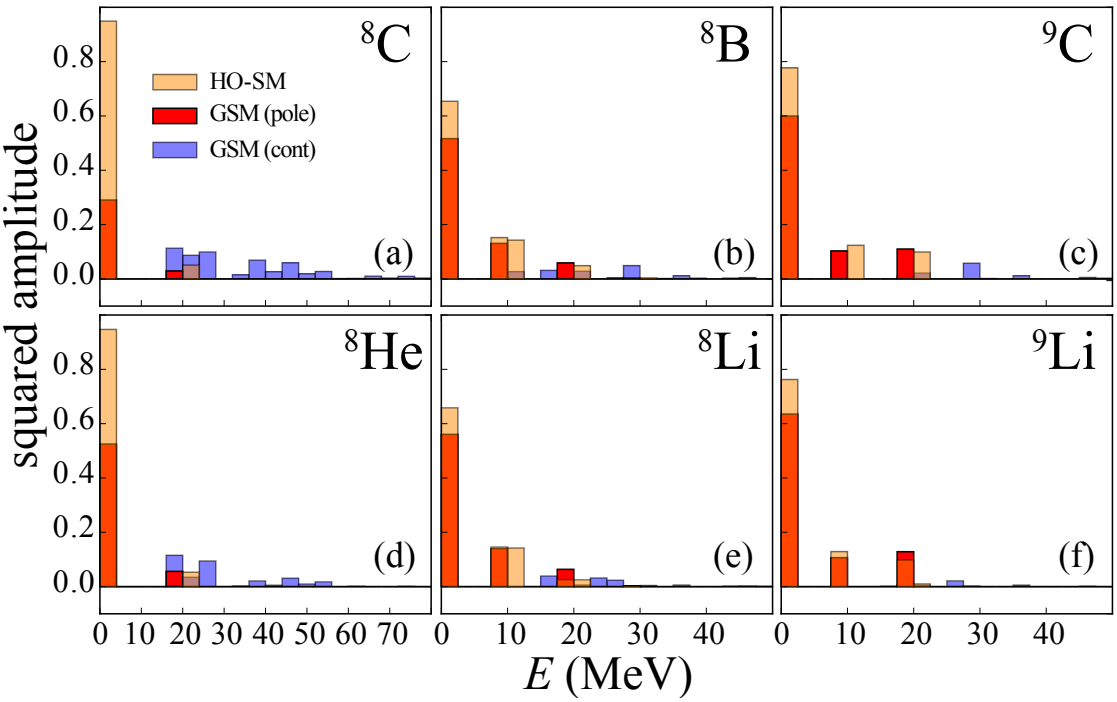


Figure 3.3: Squared amplitudes of configurations for the nuclei indicated using HO-SM and GSM. Shown are the split contributions from the GSM pole space and scattering continuum along with the occupations in the simpler HO-SM scheme. The energy presented is defined as the sum of s.p. energies for valence nucleons in each configuration relative to the lowest energy configuration. Figure taken from Ref. [46].

Table 3.1: Spectroscopic factors for the knockout of a $p_{3/2}$ nucleon from the $3/2^-$ g.s. of $^9$C and $^9$Li to the g.s. of $^8$C and $^8$He and knockout of a $p_{1/2}$ nucleon to the g.s. of $^8$B and $^8$Li. The experimental neutron and proton separation energies [2] are shown (in MeV). The Model column indicates the particular model space for the calculation as described in Sec. 3.3. $N_{\rm cont}$ is the number of particles allowed in non-resonant continuum of $A = 8$ nuclei. The last row shows the contribution from the resonant $0p_{3/2}$ state. Table taken from Ref. [46].

| Model | $N_{\rm cont}$ | $^9$C$\rightarrow^8$C $S_n = 14.22$ | $^9$Li$\rightarrow^8$He $S_p = 13.94$ | $^9$C$\rightarrow^8$B $S_p = 1.30$ | $^9$Li$\rightarrow^8$Li $S_n = 4.06$ |
|---|---|---|---|---|---|
| HO-SM | 0 | 0.86 | 0.85 | 0.95 | 0.96 |
| GSM-*ps* | 3 | 0.67 | 0.67 | 0.98 | 0.98 |
| GSM-*psd* | 3 | 0.60 | 0.67 | 0.89 | 0.88 |
| GSM-*psd* | 4 | 0.48 | 0.65 | 0.89 | 0.88 |
| GSM-$psd_{\rm res}$ | 4 | 0.48 | 0.64 | 0.84 | 0.85 |

an ideal candidate for an OQS description.

For the sake of illustration, we also provide a schematic view of how one may consider the partially-summed continuum configurations in Fig. 3.4. Partially-summed configurations are where all continuum states ($n$ excitations) for each partial wave are summed together into one general scattering contribution. For example, in our case, $0p_{3/2}$ is a resonant pole, and the $p_{3/2}$ contour is discretized by 15 points numerically, one will have 15 different configurations of $\pi\left(0p_{3/2}\right)^3\left(p^{\rm scat}_{3/2}\right)$ from $\pi\left(0p_{3/2}\right)^3\left(1p_{3/2}\right)$ to $\pi\left(0p_{3/2}\right)^3\left(16p_{3/2}\right)$. The corresponding squared amplitudes for each distinct configuration can be summed together to provide a total quantity representing discrete poles coupled with continuum states $\pi\left(0p_{3/2}\right)^3\left(p^{\rm scat}_{3/2}\right)$. Based on the schematic view, we illustrate that the change in the dominant HO-SM configuration $\pi\left(0p_{3/2}\right)^4 = 95\%$ dissipates into a distribution of continuum states. Similarly, we see the same dissipation occur in the mirror nucleus $^8$He in Fig. 3.3d. While changes in configurations between HO-SM and GSM may not be indicative on their own, when we

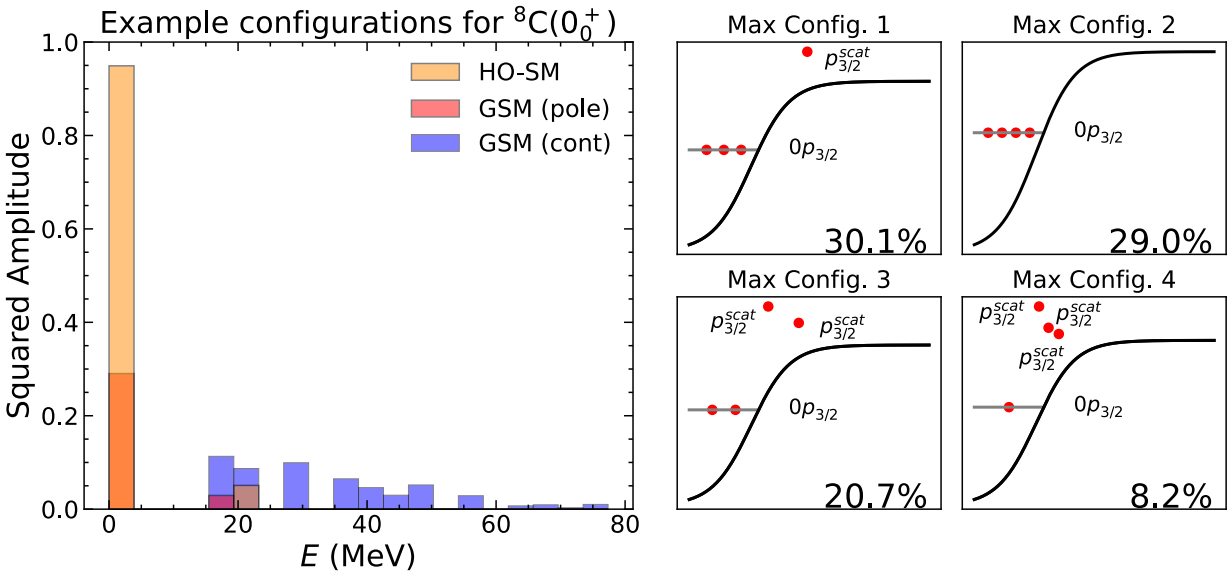


Figure 3.4: (Right) Example of the largest four partially-summed configurations contributing to the (Left) squared amplitude histogram for $^8$C [46]. We present a generic WS potential to illustrate bound versus unbound s.p. states within each configuration. The histogram bar color and meaning is the same as Fig. 3.3.

consider the location and structure of the poles in the parent nuclei $^9$C and $^9$Li, we note a three dominant pole configuration structure (in the HO-SM and GSM poles) whereas $^8$C and $^8$He only have two dominant pole configurations. This alteration and reduction of dominant configurations thus is the driving factor for the suppression of the SFs in our study.

### 3.4.2 Majority Species Nucleon Removal

We now consider the effects on SFs when removing majority species nucleons from $^9$C and $^9$Li to produce $^8$B and $^8$Li respectively. As shown in Table 3.1, increasing the available number of continuum states in our system does not produce a significant change to the SFs. In fact, the resulting SFs for weakly-bound nucleon removal saturate at a value near one, indicating that the assumption of a core-spectator system may be sufficient due to the similarities with an independent particle model approach.

Focusing on the configurations, we see in Fig. 3.3 that parent and daughter share the

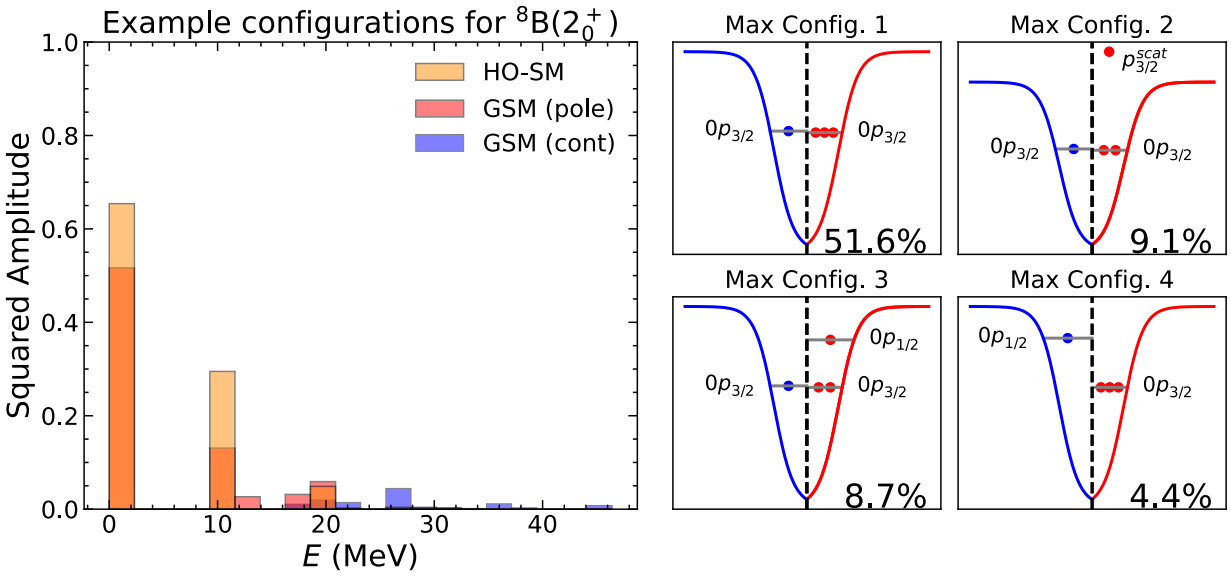


Figure 3.5: Example of largest 4 partially-summed configurations contributing to the squared amplitude histogram for $^8$B [46]. This figure follows the same labeling scheme as Fig. 3.4.

same three dominant pole configurations, indicating less structural changes due to favoring pole-space occupations. Additionally, the dissipation of these pole states into continuum contributions is mitigated, as the daughter systems from majority nucleon removal will tend towards stability (where continuum contributions are unlikely). Again, if we consider a schematic example for $^8$B, shown in Fig. 3.5, we note that only one of the dominant four partially summed configurations contains direct continuum states.

## 3.5 Conclusions

Using the GSM formalism, we have systematically explored the effects of continuum coupling on SFs. We have demonstrated [46] that continuum coupling contributions can produce strong suppression, or quenching, of SFs when removing well-bound (minority species) nucleons. Sources of this difference can be attributed to the appreciable alterations to configurations between parent and daughter nuclei. Specifically, when removing a minority species nucleon, the system moves in the direction of the dripline where continuum effects will sig-

nificantly alter the configurations. Simultaneously, we have shown that the effects of the continuum on SFs when removing weakly-bound (majority species) nucleons is rather weak and quickly saturates to a value not associated with SF suppression. Removal of majority species nucleons instead will push the remnant nucleus towards stability where continuum dominated configurations will be least likely to have substantial occupation.

Continuum coupling effects on SFs were also shown to be qualitatively consistent with GSM using another model, Shell Modle Embedded in the Continuum (SMEC) [46]. The level of openness in SMEC was controlled by altering the number of decay channels available, a different mechanism compared to GSM's indirect basis truncation approach. Further investigations into the isospin dependence of nucleon-nucleon interaction strength is needed along with probes into larger angular momentum ($\ell > 3$) systems which can also impact nucleon interactions.

# Chapter 4. Description of $^{9}$N

With the opening of the Facility for Rare Isotope Beams (FRIB) and improvements and innovations to existing radioactive ion beam facilities, nuclear experimentalists will be able to probe further into exotic regions of the nuclear chart [4, 59]. These exotic nuclei will have larger imbalances in the number of their constituent protons and neutrons and will be found closer to the nuclear driplines, as already demonstrated in recent work [60]. For lighter nuclei, the limits to the binding of these asymmetric nuclei are well defined experimentally since the driplines are known; however, beyond the dripline the limits to nuclear existence are not known experimentally and its definition is subject to debate [61].

This chapter contains my contributions to studying the structural and decaying properties of the extremely proton-rich nucleus $^{9}$N that has been observed recently [62].

## 4.1 Particle-Emitting Nuclei

For the purposes of this work, we define nuclear existence as the minimum time required to form a nuclear structure. An estimate of this time can be obtained by determining the period of a nucleon that traverses a nucleus of a given size, which for $A \approx 10$ is roughly $T_{1/2} \approx 10^{-22}\,\mathrm{s}$ or a decay width of $\Gamma \approx 4.5\,\mathrm{MeV}$ [63]. If a nucleon can traverse a nucleus within this temporal boundary, then mean-field formation can occur which is an assumption for many nuclear structure models. Another benefit to this definition is that nuclear interactions which produce resonances or bound states should lead to some alteration of an incident particle. If the length of interaction time within the compound nucleus is too short, then it is virtually indistinguishable from a scattering state or a background continuum. Nuclear resonances exist between the driplines and this ephemeral (diffuse) region of the nuclear chart, and better probing these systems experimentally can give better insight into the edges of the

nuclear landscape. These ephemeral nuclei located beyond the dripline will primarily decay by (multi-)nucleon emission.

The lightest section of the nuclear chart contains many nuclei that decay by nucleon emission and favor decay by steps of one- or two-proton ($p$ or $2p$) emission until ending at a particle-bound residue [64, 65]. Many of these nuclei, which decay by nucleon emission, have been observed, and more are likely to be discovered [66]. Currently, the list of nuclei which decay by emitting $3p$ from the ground state are: $^{7}$B, $^{13}$F, $^{17}$Na, and $^{31}$K [67–70] and $4p$ in total are: $^{8}$C and $^{18}$Mg [71, 72]. Although every nucleus is unique, these nucleon emitters share similar decay behavior. Due to nucleonic pairing, odd-$Z$ proton emitters will favor single-proton emission while even-$Z$ proton emitters tend to favor $2p$ emission [64, 65].

Focusing on a particular isotone chain ($N = 2$) we can better understand these general effects. Starting from a $^{4}$He core, one can build these nuclei by adding one proton ($^{5}$Li), two protons ($^{6}$Be), three protons ($^{7}$B), and four protons ($^{8}$C). This chain is of particular interest as $^{8}$C is a system with half of its nucleons in the continuum coupled to an $\alpha$ core. One may reasonably wonder where the boundary of proton emitters meets its ambiguous end and if there are any resonant nuclei further up this isotone chain? To address this question, we presented theoretical predictions of the structure of $^{9}$N, the next nucleus in the $N = 2$ chain and a $5p$ emitter, along with experimental observation in Ref. [62]. $^{9}$N is an interesting nucleus as over half of its constituent nucleons sit in the continuum and can be described as a $^{8}$C+$p$ system.

## 4.2 Nuclear Features

As we have highlighted, the formalism used in GSM naturally includes various complex-momentum poles of the $S$-matrix seen in Fig. 2.1. These *resonant states* are mathematical

constructs used to describe physical phenomena like *resonances* and for clarity we note the mathematical and physical distinction between the two terms. Moreover, careful definitions of features arising from nucleon interactions are paramount, as some nuclear structure features cannot be classified as resonances or bound states such as antibound states.

Examples of these features can be seen even in simple systems like the dineutron and diproton. Although the dineutron (a system of two neutrons) is not bound, it is also not a resonant or scattering state (although closely related to the latter) [25, 73, 74]. Instead, the dineutron is classified as an antibound (or virtual) state or a state with exponentially increasing asymptotics as shown in Fig. 2.1 mathematically. Such states arise naturally in $S$-matrix formalism and manifest as a enhanced cross section *and* produce a large positive value of the phase shift derivative $d\delta/dk$ near zero energy [25].

Similarly, a diproton system is neither a bound state nor resonance, and is classified as a subthreshold resonance [73, 75]. Subthreshold resonances exist in the complex-$k$ plane below the $\pi/4$ line and produce an enhanced scattering length like an antibound state. Both subthreshold resonances and antibound states can be associated as final state effects. We will focus on this distinction between these scattering features and resonances in $^{9}$N and $^{9}$He.

## 4.3 Structure of $^{9}$N

### 4.3.1 Prediction of $^{9}$N Structure

As discussed in Sec. 4.1, $^{9}$N is three neutrons away from the lightest bound nitrogen isotope and is reasonably assumed to be a $^{8}$C+$p$ resonance. To provide meaningful theoretical predictions, we built $^{9}$N as a $5p + \alpha$ system and used the same interaction parameters and model space as Sec. 3.3 [46] to ensure good reproduction of the $^{8}$C g.s., without any

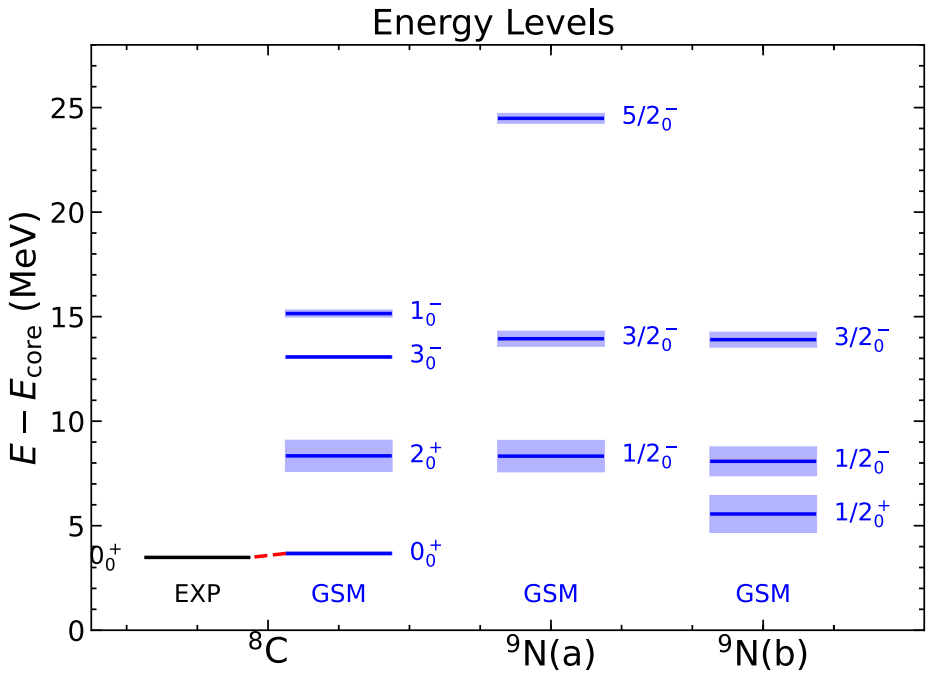


Figure 4.1: Calculated spectra using GSM. $^8$C and $^9$N(a) calculations use the same model space as Sec. 3.3 and serve as initial predictions. $^9$N(b) uses a modified model space to produce the $1/2^+$ state *after* comparison with experimental data.

experimental information for $^9$N. We then applied these parameters to $^9$N and searched for a variety of possible $J^\pi$ states. Ultimately, we obtained converged predictions as shown in Fig. 4.1 which could be compared with experimental data.

The experimental data did not contain enough statistics to provide constrained fits [62] as shown in Fig. 4.2. In particular, only a single-peak fit could be obtained with the available statistics (Fig. 4.2a), yet this required setting the magnitude of background event to 14% or lower [62] (an unreasonable assumption [76]). Consequently, we used GSM to provide new calculations with information from other nuclei to better constrain the experimental results. Specifically, we turned to the mirror partner $^9$He [77–82].

$^9$He belongs to the $N = 7$ isotone chain, which is known to contain low-lying $1/2^+$ and $1/2^-$ doublets for nuclei with low proton numbers, such as $^{11}$Be [83]. In $^{11}$Be, an intruder $s$-wave state produces the doublet $1/2^+$ and $1/2^-$ states which are bound and localized [83]. In

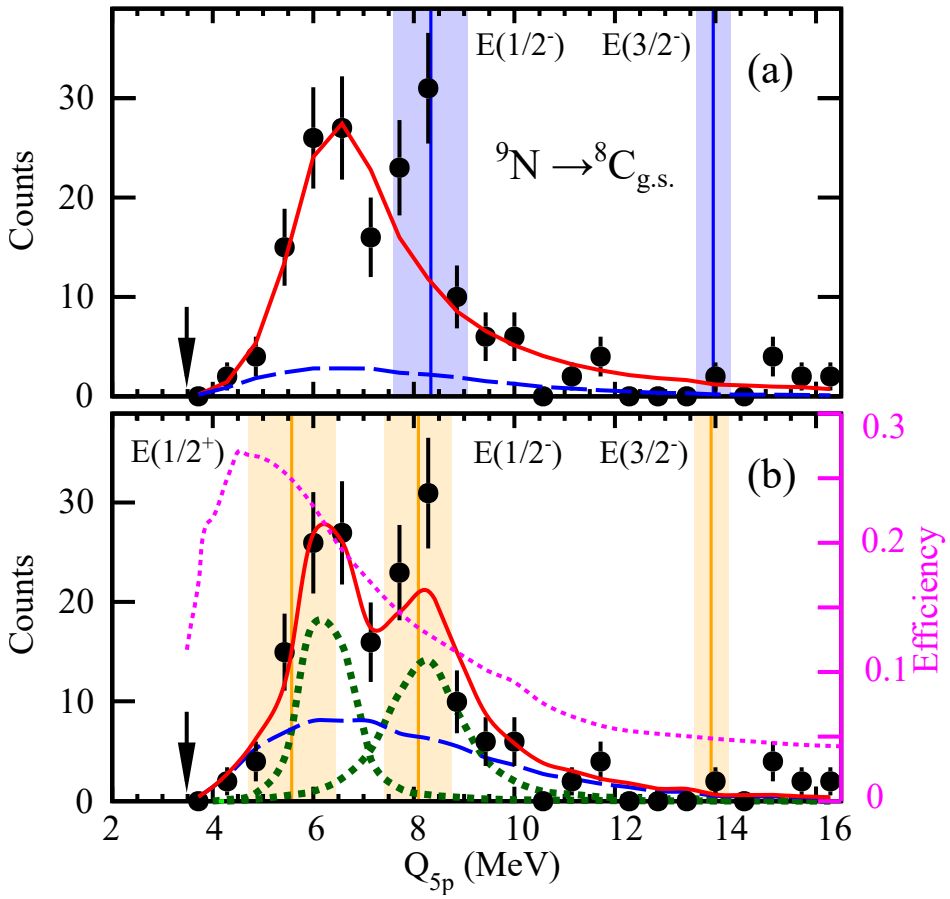


Figure 4.2: (a) Single-peak fit using an $\ell = 1$ $R$-matrix lineshape and predicted spectra using GSM overlaid as blue vertical lines (from Fig. 4.1). (b) $R$-matrix lineshape using the refined GSM energies as vertical orange lines (discussed in Secs. 4.3.2 and 4.3.3) and the corresponding GSM refined energies. Modified from Ref. [62].

$^{9}$He however, only the energy of the $1/2^{-}$ state has been consistently measured, albeit with some disagreement on its width [77–79]. In contrast to $^{11}$Be, the presence of the $1/2^{+}$ feature in $^{9}$He does not have a uniform consensus and only some works indicate its existence [77, 79–82]. We focus on investigating the exotic features in $^{9}$He and the implications for the structure of $^{9}$N in the next section.

### 4.3.2 Refinement of $^{9}$N structure using $^{9}$He

Despite using a model space which included continuum $s$-wave states, initial searches for a $1/2^{+}$ state were unsuccessful for both $^{9}$N and $^{9}$He. In the case of $^{9}$He, previous Berggren basis calculations were able to produce a $1/2^{+}$ state, yet they did so by including an additional $1s_{1/2}$ basis pole. By using this additional pole in their calculations, the $1/2^{+}$ state manifested as an artificially bound state [37, 63] and precluded these works from determining if $^{9}$He was a genuine state or antibound feature. It should be noted that it is theoretically possible to obtain the same results without including the $1s_{1/2}$ basis pole, but it requires a very dense discretization of the $s_{1/2}$ contour to meet the unitarity condition [40]. Moreover, it has been shown that including the bound $1s_{1/2}$ pole in the GSM basis can help convergence rates and accuracy for bound many-body states, yet many-body states with antibound behavior will not uniformly benefit from this speedup [30].

Great care is warranted when focusing on the unbound $1/2^{+}$ states to avoid improper handling of fragile features such as antibound states. Since reproducing antibound states without including a $1s_{1/2}$ basis pole requires a significant number of non-resonant scattering continuum states (contour discretization points), we will forgo this approach due to model space size constraints in favor of including the $1s_{1/2}$ basis pole. We checked the effects of this basis pole on the $1/2^{+}$ state by varying the depth of the WS one-body basis potential. Comparing the calculation results to experimental values for $^{9}$He [77], we find that the best

reproduction of the $1/2^+$ feature coincides with an antibound $1s_{1/2}$ basis pole just before crossing threshold. It is worth noting that this antibound state is sensitive to the placement of the $1s_{1/2}$ basis pole. This basis dependence, while not ideal, is unsurprising as the use of the $1s_{1/2}$ basis pole supplants the finer contour discretization which would otherwise be required.

After determining that the best $1/2^+$ reproduction occurs with a barely-antibound $1s_{1/2}$ basis pole, we extended this search procedure to GSM of $^9$N. Since protons cannot be antibound due to the presence of the Coulomb barrier [84], we cannot use the exact same basis as $^9$He in a proton-rich version. The behavior which best reproduced the $1/2^+$ state $^9$He was an antibound $1s_{1/2}$ pole nearest threshold; thus, we chose an analogous version for the proton basis where a narrow resonant $1s_{1/2}$ pole was selected.

We can study the effects of this basis choice by comparing these results with that of a bound basis pole and find that the energy will vary by roughly one MeV but the decay width may be strongly suppressed (see Fig. 4.3). The effect the choice of basis can have on the convergence of decay widths of many-body GSM states is well documented [29, 31, 37, 85]. As discussed in the references therein, depending on the goals of the practitioner, one may favor better energy reproduction over calculating an exact decay width as the later may require more computational resources. Since the completeness relation holds, if one chooses enough non-resonant continuum states, the resulting energies will remain albeit with different occupations than if using an artificial basis pole [85].

For a majority of many-body states, which are bound states or narrow resonances, the tension of convergence rate to reproducibility of states does not usually pose a significant dilemma (see the bound states in Fig. 4.3). However, we see in the case of near- or above-threshold states, the choice of using resonant basis poles can lead to variation in the energy

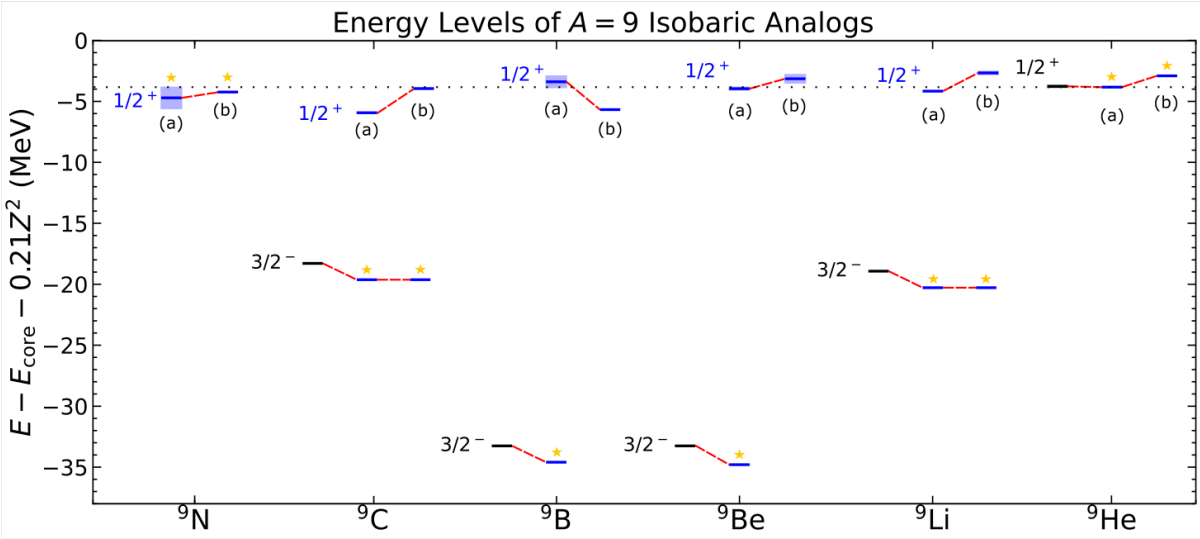


Figure 4.3: Calculation of isobaric analog states for the $A = 9$ chain scaled by a factor of $aZ^2$ where $a = 0.21$ to compensate for Coulomb energy corrections. Experimental results are shown in black and two versions of GSM results are shown in blue with an antibound (a) basis pole and bound (b) basis pole. States with a gold star above them are those with well converged energies ($\left|\langle\tilde{\Psi}|\, H\, |\Psi\rangle - E\,\langle\tilde{\Psi}|\Psi\rangle\right| \leq 10^{-3}$) and proper calculation of the expected isospin $\langle T\rangle$. Previous experimental results are shown from Refs. [2, 77], but we do not include the experimentally estimated $1/2^+$ energy for $^9$N as it was determined in this work (see Fig. 4.5) [62].

and decay width. This holds true if the contour discretization is insufficient, and computing the decay width can be unstable [31]. Despite the possible instability associated with using unbound basis poles, the widths of the $1/2^-$ state in $^9$He and $^9$N are well under control for both bound and resonant basis poles. Using an unbound basis pole causes the $^9\mathrm{N}\left(1/2^+\right)$ state to be much broader than the bound basis pole calculation (which has an unusually narrow width).

### 4.3.3 Implications of $^9$N Structure

After developing the method to reproduce the structure of $^9$He and applying it to $^9$N, we are able to investigate the dependence of the energies on the choice of basis. As discussed in the section above, we systematically vary the depth $V_0(\ell = 0)$ of the auxiliary potential to generate the Berggren basis and track the trajectory of the resulting many-body states as shown in Fig. 4.4. If we rely on the method developed for $^9$He, looking for a barely narrow-resonant $1s_{1/2}$ basis pole, we find the value for $1/2^+$ which best matches this criteria is around $V_0(\ell = 0) = 100.4$ MeV. We also note that this basis variation does not impact the trajectory of the $1/2^-$ state in a meaningful way.

Due to the demonstrated stability of the $1/2^-$ state regardless of basis in Fig. 4.4, the experimentalists utilized this GSM complex energy to constrain their anti-correlated two-peak fit (see Fig. 4.2b). By using this GSM $1/2^-$ energy as a constraint, the two-peak fit produced a significance beyond the capabilities of Monte Carlo [62]. The two-peak-plus-background hypothesis concludes that the data is highly likely to originate from $^9$N structures at a $5\sigma$ threshold. Resulting experimentally determined energies and the GSM results using the refined basis are illustrated in Fig. 4.5.

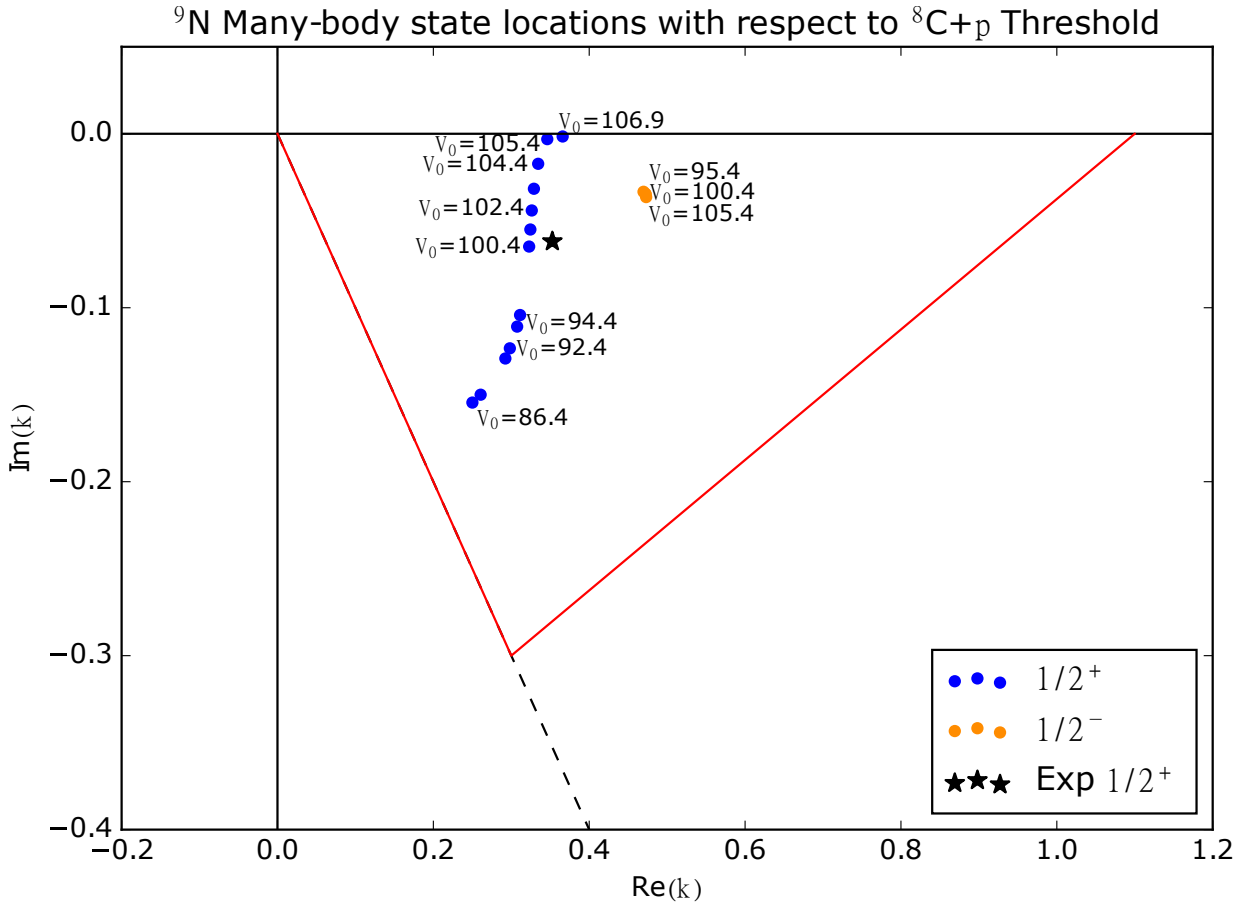


Figure 4.4: Trajectory of the many-body eigenvectors for the GSM calculation of $^{9}$N with varying WS basis depth $V_0$. We show the $\pi/4$ subthreshold boundary as a black dashed line. The experimental data point is determined by using the GSM $1/2^-$ state to constrain the two-peak fit (shown in Fig. 4.2).

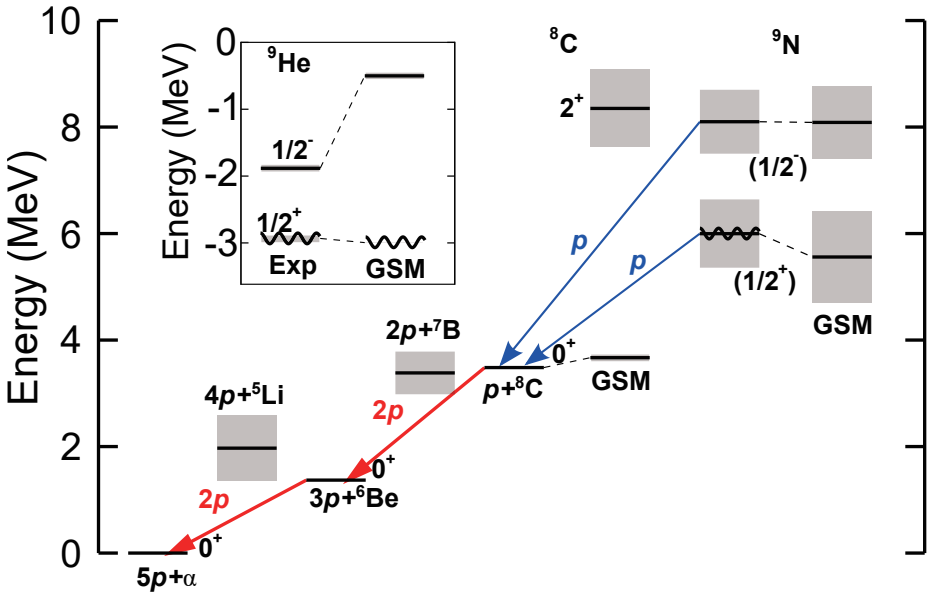


Figure 4.5: Energy spectrum for the $N = 2$ isotone decay chain relative to the $^4$He core. GSM calculations are shown alongside experimental values. Figure taken from Ref. [62].

## 4.4 Conclusions

Rare isotopes existing near or beyond the driplines are challenging systems for both experiment and theory. Of this class of nuclei, the $5p$-emitting nucleus $^9$N is a particularly interesting as over half of its constituent nucleons are unbound as its intermediate state $^8$C+$p$ contains another unbound nucleus. We provided theoretical predictions for the structure of $^9$N and this data assisted in the experimental analysis which determined the presence of $^9$N within a $\approx 5\sigma$ threshold [62].

Predicted energies for the low-lying doublet structure in $^9$N are in good agreement with the experimental energy location of these states. Furthermore, this system is interesting for mirror (isospin) symmetry as the level inversion in the $N = 7$ chain continues for $^9$N's mirror, $^9$He. Interestingly, $^9$He consists of an antibound $1/2^+$ and a real resonance $1/2^-$, and this doublet is present in $^9$N. However, the $1/2^+$ state in the proton-rich nucleus appears to be transformed into a genuine resonance rather than a scattering feature under the current

Hamiltonian and GSM framework. Unfortunately, the experimental statistics were low in this experiment and the two-peak character could not be constrained simultaneously, relying on a statistical analysis of different theoretically-informed peak profiles. Future experiments can potentially resolve this issue and more OQS model development is needed to probe these highly exotic systems where even the current GSM implementation struggles.

# Chapter 5. Projection of the Continuum

## 5.1 Motivation

Within GSM, the continuum coupling in resonances is not well quantified or understood. Other nuclear OQS models however incorporate continuum effects via explicit coupling terms. This class of continuum SM is thus complementary to GSM calculations, as was discussed for SMEC in Sec. 3.5. Essentially, one model class (GSM) incorporates the continuum in a "black box" perspective where continuum effects are introduced at a basis level; while the other model class (SMEC) has tunable parameters for direct manipulation and exploration of the continuum. Currently, there is no direct quantitative comparison between the two methods and their relation has been assumed to be valid at a theoretical level. We aim to provide quantitative evidence to support or dispute these assumptions. Ordinarily, one can explore the effects of the continuum in GSM only from the many-body structure perspective, as finer mechanisms associated with direct control of continuum coupling strength are not accessible in GSM [5, 29] without modification [38, 86]. Of course, this property of GSM is beneficial as it limits the dimensionality of the same many-body problems which would otherwise be intractable with other OQS models such as SMEC [29].

## 5.2 Shell Model Embedded in the Continuum

Before we can formulate any methods to extract quantitative continuum coupling from GSM, we must first outline the formalism for SMEC to identify possible starting points. SMEC incorporates OQS nature by dividing the system into two subspaces, a localized space ($Q$) with $A-1$ bound particles and a continuum space ($P$) with the scattering nucleon(s) in the continuum without coupling to the $Q$ space [18, 87]. This subspace picture was first outlined

by Feshbach in Refs. [88, 89] as a method to unify nuclear structure and reaction theories. Since the development of SMEC [90], it has had a long history of highlighting single-particle continuum effects [18, 90–92], including decay channel effects on exotic states [46, 93, 94], and highlighting potential effects of two-particle systems [87].

To perform SMEC calculations in the one valence nucleon case, one first needs to generate wave functions for the total function space. The $Q$ space sets are $L^2$ functions from the standard SM while the $P$ space sets are s.p. scattering states. Decays for the $A$-nucleon system will occur when the scattering states are coupled to the SM states. Both wave functions can be obtained by solving the Schrödinger equation:

$$H_{\mathrm{SM}} \left|\Phi_i\right\rangle = E_i^{(\mathrm{SM})} \left|\Phi_i\right\rangle, \quad \text{for localized space } Q \tag{5.1a}$$

$$\sum_{c'} \left(E - H_{cc'}\right) \xi_E^{c'(+)} = 0, \quad \text{for continuum space } P \tag{5.1b}$$

where Eq. 5.1a corresponds to the discrete SM calculations (CQS picture) and Eq. 5.1b to the scattering states [87]. The SM Hamiltonian (CQS) is $H_{\mathrm{SM}}$ and $H_{cc'} = H_0 + V_{cc'}$ is the coupled-channel (CC) Hamiltonian. Since the decay mechanisms are directly tied to the scattering nucleon, the channels are controlled by the nucleon's relative motion with the $A-1$ residue states $|\Phi_j^{A-1}\rangle$. One can then define projection operators for each space over their set of states

$$\hat{Q} = \sum_{i=1}^{N} \left|\Phi_i^A\right\rangle \left\langle\Phi_i^A\right|, \quad \hat{P} = \int_0^\infty dE \left|\xi_E\right\rangle \left\langle\xi_E\right| \tag{5.2}$$

such that each projection on a vector from its complement space gives

$$\hat{Q} = \left|\xi_E\right\rangle = 0, \quad \hat{P} \left|\Phi_i^A\right\rangle = 0. \tag{5.3}$$

Operators, such as the Hamiltonian, may also be projected such as $\hat{Q}H\hat{Q} = H_{QQ} = H_{SM}$ and $\hat{P}H\hat{P} = H_{PP} = H_{cc}$.

One will notice that at the current step in the formulation, we still have two distinct non-coupled spaces. Assuming that the different spaces follow $\hat{Q} + \hat{P} = I_d$, we can calculate a mixed projection

$$|\omega_i\rangle = H_{PQ} |\Phi_i\rangle \tag{5.4}$$

which produces a third wave function

$$|\omega_i^{(+)}\rangle = G_P^{(+)}(E) |\omega_i\rangle , \tag{5.5a}$$

$$G_P^{(+)}(E) = \hat{P} (E - H_{PP}) \hat{P}. \tag{5.5b}$$

Eq. 5.5b is the Green's function of a nucleon's motion in the scattering space.

We can now write the solution $|\Psi_E\rangle$ using all three function sets $\left\{|\Phi_i^A\rangle\right\}$, $\{|\xi_E\rangle\}$, and $\left\{|\omega_i^{(+)}\rangle\right\}$ by expanding $|\Psi_E\rangle = I_d |\Psi_E\rangle = \hat{Q} |\Psi_E\rangle + \hat{P} |\Psi_E\rangle$. This wave function can be operated on by

$$\hat{Q} |\Psi_E\rangle = \left(E - H_{QQ}(E)\right)^{-1} H_{QP} |\xi_E\rangle ,$$

$$\hat{P} |\Psi_E\rangle = |\xi_E\rangle + G_P^{(+)}(E) H_{PQ} \hat{Q} |\Psi_E\rangle \tag{5.6a}$$

which can be expanded to

$$|\Psi_E\rangle = |\xi_E\rangle + \sum_{i,k} \left(|\Phi_i^A\rangle + |\omega_i^{(+)}(E)\rangle\right) \langle\Phi_i^A| \left(E - \mathcal{H}_{QQ}(E)\right)^{-1} |\Phi_k^A\rangle \langle\Phi_k^A| H_{QP} |\xi_E\rangle . \tag{5.7}$$

We note that in this formalism, an energy dependent effective Hamiltonian is obtained

$$\mathcal{H}_{QQ}(E) = H_{QQ} + H_{QP}G_P^{(+)}(E)H_{PQ}. \tag{5.8}$$

which captures the effects of continuum coupling on the CQS Hamiltonian $H_{QQ}$. Therefore, $\mathcal{H}_{QQ}$ is the OQS Hamiltonian within the $Q$ space, and from this effective, energy-dependent Hamiltonian we can calculate its eigenvalues to obtain the energies $\tilde{E}_i(E)$ and resonance widths $\tilde{\Gamma}_i(E)$:

$$E_i = \tilde{E}_i(E = E_i); \quad \Gamma_i = \tilde{\Gamma}_i(E = E_i). \tag{5.9}$$

Formally, we assign the second term of Eq. 5.2 to be the continuum coupling term $W_{QQ}(E) = H_{QP}G_P^{(+)}(E)H_{PQ}$ [46]. The continuum coupling term can have different forms, but in the case of simple interactions the continuum coupling is dependent on some overall strength parameter [46, 93]. As a result, the continuum coupling strength is explicitly dependent on this parameter.

After obtaining the eigenstates of our effective Hamiltonian $|\Psi_\alpha^{J^\pi}\rangle$, which include coupling to a specific decay channel $\left[A-1 Z(K^{\pi'}) \otimes \ell_j\right]^{J\pi}$, a continuum-coupling correlation energy can be calculated to quantify the continuum-induced mixing [93, 95]

$$E^{J^\pi}_{\text{corr.},\alpha}(E) = \langle \Psi^{J^\pi}_\alpha(E)|W_{QQ}(E)|\Psi^{J^\pi}_\alpha(E)\rangle = \langle \Psi^{J^\pi}_\alpha(E)|\mathcal{H}_{QQ}(E) - H_{QQ}|\Psi^{J^\pi}_\alpha(E)\rangle\,. \tag{5.10}$$

## 5.3 Quantifying the Continuum in GSM with Projection

Aside from the work in Chs. 3 and 4, GSM has been used to study many OQS phenomena in nuclear physics from threshold effects like Wigner cusps [54] to the structure of exotic nuclei [30, 39, 72]. The differences in the formalism of coupling two spaces compared to using a holistic Rigged Hilbert Space are highlighted in Fig. 5.1. A limitation to GSM is the inability to control specific phenomena (such as the characterization of individual decay channels) and the correlation between these phenomena and the strength of continuum coupling, as both are implicitly handled in GSM. In other words, interesting many-body structural phenomena can be modeled, but we cannot directly probe or quantify the mechanisms that drive the desired behavior. This dilemma is the motivation for our work, and our goal is to follow the Feshbach projection approach of SMEC to isolate the CQS and pure-scattering continuum terms from the GSM continuum couplings.

### 5.3.1 Formalism

For well-bound systems, GSM's results can be indistinguishable from results calculated in a traditional SM as these nuclei will have little continuum dependence (recall Fig. 3.3). This conclusion is unsurprising as bound states defined in any similar basis will likely share the same spatial localization. We take advantage of this property and assume that within a GSM calculation, there must exist a subspace which is representative of the SM solutions for well-bound nuclei, see Fig. 5.2. The main question is then, how might we use this assumption to build operators to project-out the SM-like components of a full GSM calculation? There are a few possible methods we can practically do this, each with their own particular challenges,

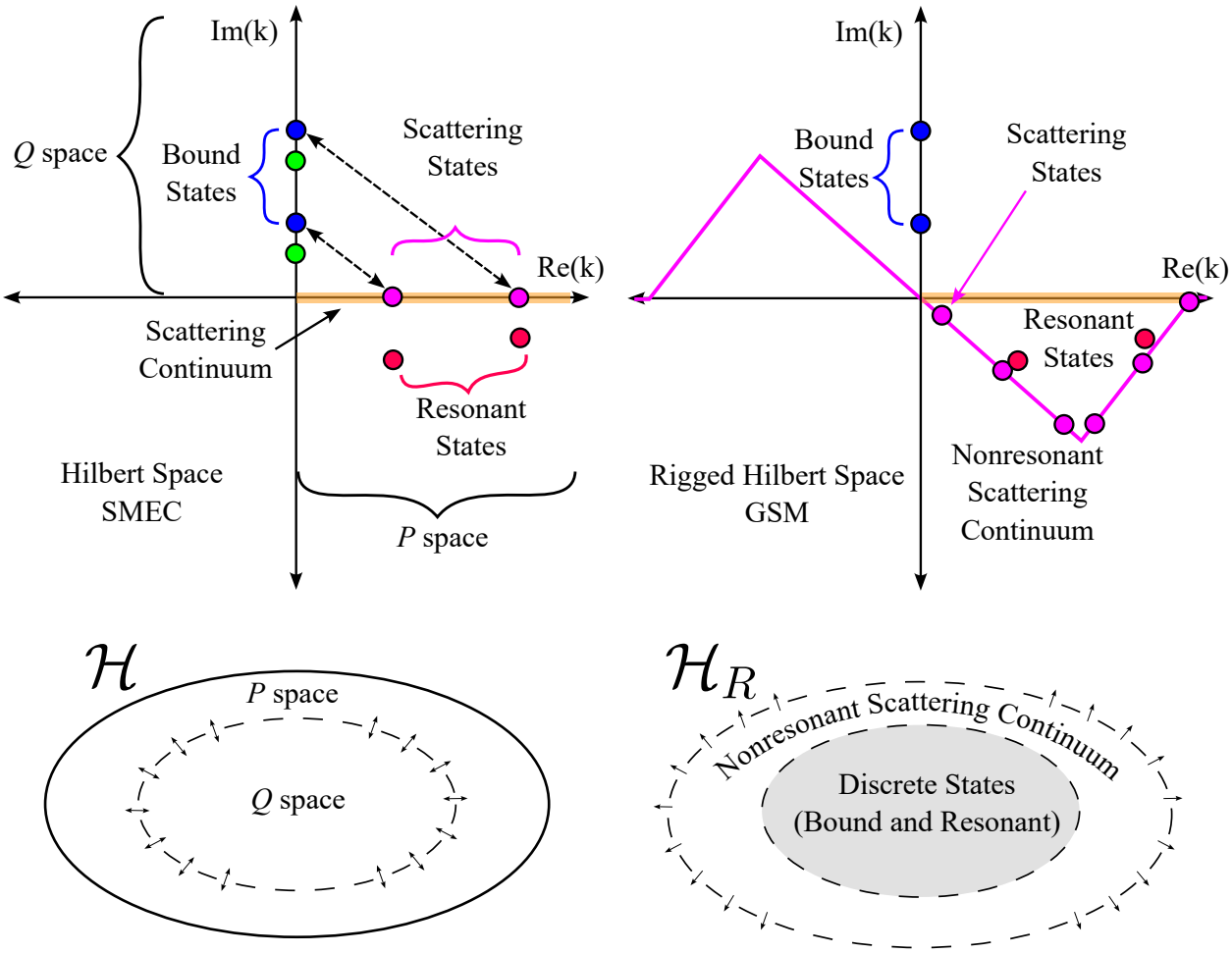


Figure 5.1: (Top) Representation of different approaches depending on choice of Hilbert Space (SMEC) or Rigged Hilbert Space (GSM) formalisms. Resonances manifest in both cases, yet the mechanisms differ by the space choice. (Bottom) We show the functional "zones" of both approaches. SMEC requires coupling between to separate spaces to produce the OQS effects. GSM's Rigged Hilbert Space contains all components for OQS, but it is difficult to disentangle the continuum coupling effects.

but we will first describe the assumptions we will use to make these operators.

To create a CQS projection operator, we must use some set of localized basis states to construct a space we believe to be entirely closed, with Dirichlet boundary conditions imposed. These boundary conditions require that outside of some domain, the wave function must be zero, such as $u(r = 0) = 0$ and $u(r = R_{\text{box}}) = 0$, and could be considered as imposing an infinite square well boundary condition where particles cannot enter or escape (decay).

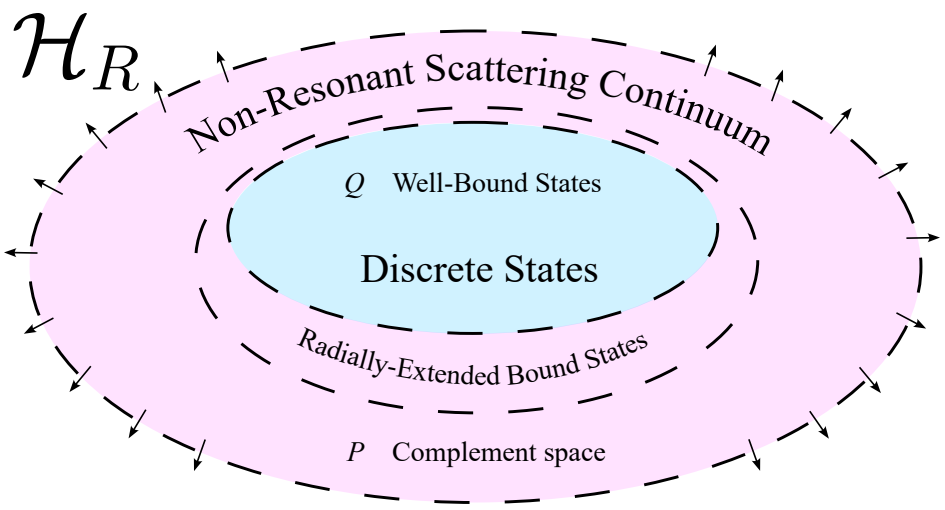


Figure 5.2: Depiction of isolating a $\mathcal{Q}$ space (blue) in GSM by accounting for states generated in a well-localized basis. The complement space is shown in violet and contains any features not captured by the $\mathcal{Q}$-space. This figure is an illustration of applying the Feshbach projection technique onto GSM as presented in Fig. 5.1.

Using these CQS states $|\Phi\rangle$, we build a general CQS projector

$$\mathcal{Q} = \sum_{i}^{N} |\Phi_i\rangle \langle\Phi_i| \tag{5.11}$$

or more generally

$$A = \begin{pmatrix} | & | & & | \\ \Phi_1 & \Phi_2 & ... & \Phi_N \\ | & | & & | \end{pmatrix}_{m\times N} \quad \text{and} \quad \mathcal{Q} = A\left(A^T A\right)^{-1} A^T \tag{5.12}$$

with vectors $\Phi$ having length $m$. Although we would expect higher energy components of our system to be associated with continuum effects, it is certainly possible to have high energy components in $\mathcal{Q}$ which happen to coincide with discretized scattering states we are attempting to isolate. This would be cases where pseudo-continuum states generated from a CQS basis are similar to select, genuine, scattering states as their boundaries coincide with

a specific radial point of a node in a scattering state $r_{\text{box}} = r_{\text{node}}$.

Since OQS by definition have features which cannot be naturally described in a CQS framework, $\mathcal{Q}$ will only act on a subspace of the OQS space; thus, there must be some complementary space where

$$I \approx \mathcal{Q} + \mathcal{P}, \rightarrow \mathcal{P} \approx I - \mathcal{Q}. \tag{5.13}$$

Here we assume that the working Berggren basis is large enough to encompass long range effects. In the above equation, $I$ represents the $A$-body Fock space of the Berggren ensemble employed in GSM. This $I$ is not a true unity operator, like one finds in a Hilbert space, as the system is built from a reference core rather than the vacuum.

From the constructed CQS and scattering-space projection operators, any GSM operator $\mathcal{O}$ can be decomposed via

$$\begin{aligned} \mathcal{O}_{\text{GSM}} &= (\mathcal{P} + \mathcal{Q})\, \mathcal{O}_{\text{GSM}}\, (\mathcal{P} + \mathcal{Q}) \\ \mathcal{O}_{\text{GSM}} &= \mathcal{Q}\mathcal{O}_{\text{GSM}}\mathcal{Q} + \mathcal{P}\mathcal{O}_{\text{GSM}}\mathcal{Q} + \mathcal{Q}\mathcal{O}_{\text{GSM}}\mathcal{P} + \mathcal{P}\mathcal{O}_{\text{GSM}}\mathcal{P}. \end{aligned} \tag{5.14}$$

Continuum coupling for specific observable quantities can be obtained by projecting their corresponding operators, such as the Hamiltonian:

$$\begin{aligned} H_{\text{GSM}} &= (\mathcal{P} + \mathcal{Q})\, H_{\text{GSM}}\, (\mathcal{P} + \mathcal{Q})\,, \\ H_{\text{GSM}} &= \underbrace{\mathcal{Q}H_{\text{GSM}}\mathcal{Q}}_{\text{CQS}} + \underbrace{\mathcal{P}H_{\text{GSM}}\mathcal{Q} + \mathcal{Q}H_{\text{GSM}}\mathcal{P}}_{\text{Coupling}} + \underbrace{\mathcal{P}H_{\text{GSM}}\mathcal{P}}_{\text{Scattering}}. \end{aligned} \tag{5.15}$$

As shown, projected energies can be associated as $E_{\mathcal{Q}\mathcal{Q}} = \mathcal{Q}H_{\text{GSM}}\mathcal{Q}$ being the CQS-like

energy, $E_{\mathcal{PP}} = \mathcal{P}H_{\rm GSM}\mathcal{P}$ being the pure-scattering energy, and $E_{\mathcal{PQQP}} = \mathcal{P}H_{\rm GSM}\mathcal{Q} + \mathcal{Q}H_{\rm GSM}\mathcal{P}$ being the continuum-continuum coupling term. For more manageable notation we will adopt the following convention:

$$\mathcal{Q}H_{\rm GSM}\mathcal{Q} = H_{\mathcal{QQ}}, \qquad \mathcal{P}H_{\rm GSM}\mathcal{P} = H_{\mathcal{PP}},$$
$$\mathcal{P}H_{\rm GSM}\mathcal{Q} = H_{\mathcal{PQ}}, \qquad \mathcal{Q}H_{\rm GSM}\mathcal{P} = H_{\mathcal{QP}}.$$

Considering the typical GSM (Rigged Hilbert space) picture, one would expect the decomposed version to be of the form of Fig. 5.3. Focusing on the $H_{\mathcal{QQ}}$ component, one would anticipate that the first Riemann energy sheet would only contain few discrete continuum contributions but have many of the bound states, assuming the localized states used in $\mathcal{Q}$ are a good representation. Additionally, in the second Riemann sheet of $H_{\mathcal{QQ}}$, some low-energy Gamow states may appear depending on the system and will be shifted onto the real axis as shown in Fig. 5.3. CQS projection essentially will capture the localized components of the resonant states with the remainder being left in the $\mathcal{P}$-space.

On the other hand, the $H_{\mathcal{PP}}$ component would be expected to contain all pure scattering terms and perhaps a weakly-bound, or severely radially extended, state. More likely, we would expect this term to instead collect more Gamow states and retain the coupling terms that are larger, towards pure continuum states. In either case, we can more easily see in the second Riemann sheets that these projected systems might still retain some resonant (Gamow) states but will only highlight the real-energy and continuum contributions respectively. The final part, which is the goal of this work, is to then extract the continuum coupling $H_{\mathcal{QP}} + H_{\mathcal{PQ}}$.

Before continuing, we explicitly define the corresponding SDs and bases to avoid any

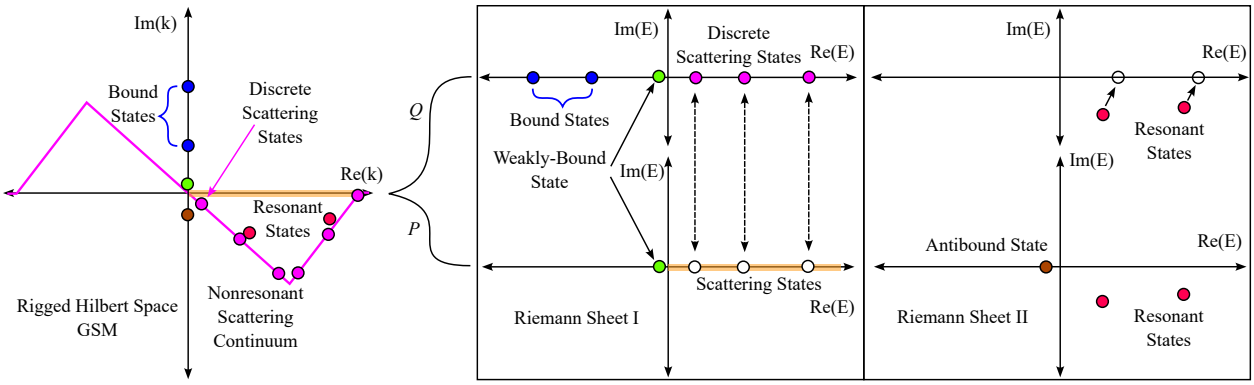


Figure 5.3: Illustration of the CQS and pure scattering components of the Hamiltonian after applying the projection operators in Eq. 5.15. The complex $k$-plane has been divided into its two energy Riemann sheets in order to highlight the behaviors we would expect to capture using the $\mathcal{Q}$ and $\mathcal{P}$ operators. Riemann Sheet I shows the projection of the physical sheet and Riemann Sheet II shows the projection onto the non-physical sheet. Resonant states are on the non-physical sheet but can be accessed via contour deformations.

confusion. Single-particle states will be referred to using a lower-case Greek letter ($|\phi\rangle$ and $|\psi\rangle$) and any many-body states will be upper-case Greek letters - $|\Phi\rangle$ and $|\Psi\rangle$ for CQS and OQS respectively. Generally, to build a nucleus we apply creation operators to add $n$ valence nucleons onto a closed shell $|c\rangle$ to form the arbitrary wave function $|\Xi_i\rangle = \left[g_1^\dagger g_2^\dagger ... g_n^\dagger\right]_i |c\rangle$. In our case we define the SDs as

$$\begin{aligned} \text{CQS} \quad & |\Phi_i\rangle = \left[a_1^\dagger a_2^\dagger ... a_n^\dagger\right]_i |c\rangle \,, i = 1, ...d, \\ \text{OQS (GSM)} \quad & |\Psi_i\rangle = \left[b_1^\dagger b_2^\dagger ... b_n^\dagger\right]_i |c\rangle \,, i = 1, ...d, \end{aligned} \tag{5.16}$$

where $a^\dagger$ and $b^\dagger$ are the creation operators for the chosen CQS and Berggren bases respectively. Here, $d$ refers to the corresponding quantum numbers for each state. Many-body basis SDs $|\Psi_i^B\rangle$ used in GSM can naturally expand a particular resonant state $|\Psi_\nu\rangle$ (an eigenstate of $H_{\text{GSM}}$) as

$$|\Psi_\nu\rangle = \sum_i c_i \, |\Psi_i^B\rangle \,. \tag{5.17}$$

Note that from now on, for clarity, any state with a $B$ superscript refers to a basis state and states with Greek letter subscripts ($|\Psi_\nu\rangle$) are specific Gamow states (eigenvectors of the Hamiltonian). We will discuss some additional notation for clarity since we will be working with two different bases. If any state or operator is surrounded by parenthesis accompanied by a subscript or just accompanied by a subscript, this indicates the operator is in that corresponding basis e.g. $I_\Psi = (I)_\Psi$ is in the GSM basis $\Psi$. This is helpful when an explicit basis state is not written like $|\Psi_i^B\rangle$.

First, we consider the operation of $\mathcal{Q}$ on a single GSM basis state

$$\mathcal{Q}\,|\Psi_j^B\rangle = \sum_i |\Phi_i^B\rangle\,\langle\Phi_i^B|\Psi_j^B\rangle = \sum_i |\Phi_i^B\rangle\,M_{ij}. \tag{5.18}$$

A transformation coefficient $M_{ij}$ arises which will allow transformations between $\Phi$ and $\Psi$ basis vectors. This can be expanded into matrix using a complete set of GSM basis vectors (in other words, the identity)

$$\mathcal{Q}I_\Psi = \left(\sum_i |\Phi_i^B\rangle\,\langle\Phi_i^B|\right)\left(\sum_j |\Psi_j^B\rangle\,\langle\tilde{\Psi}_j^B|\right) = \sum_{ij} |\Phi_i^B\rangle\,\langle\Phi_i^B|\Psi_j^B\rangle\,\langle\tilde{\Psi}_j^B| = \sum_{ij} |\Phi_i^B\rangle\,M_{ij}\,\langle\tilde{\Psi}_j^B| = M. \tag{5.19}$$

The $\mathcal{Q}$ operator can be applied in the opposite direction and has a slightly different form

$$I_\Psi\mathcal{Q} = \left(\sum_j |\Psi_j^B\rangle\,\langle\tilde{\Psi}_j^B|\right)\left(\sum_i |\Phi_i^B\rangle\,\langle\Phi_i^B|\right) = \sum_{ij} |\Psi_j^B\rangle\,\langle\tilde{\Psi}_j^B|\Phi_i^B\rangle\,\langle\Phi_i^B| = \sum_{ij} |\Psi_j^B\rangle\,\tilde{M}_{ij}\,\langle\Phi_i^B| = \tilde{M}. \tag{5.20}$$

Here $M$ and $\tilde{M}$ each denote the conjugation status of our GSM state ($|\Psi^B\rangle$ and $\langle\tilde{\Psi}^B|$). Since the proper GSM conjugation is simply time reversal (no complex conjugate in Eq. 2.10), we need this distinction as the CQS state could require a complex conjugation. In the case where we have only real wave functions, this reduces to a case where $M = \tilde{M}^T$, but the most general definition requires this distinction. The matrix $M$ is $N_{\text{CQS}} \times N_{\text{GSM}}$ and its partner's dimensions are swapped. From these expressions, we can write the projection operator $\mathcal{Q}$ in the GSM basis

$$\mathcal{Q}_\Psi = \tilde{M}\left(M\tilde{M}\right)^{-1} M \tag{5.21}$$

to create a projection operator with $N_{\text{GSM}} \times N_{\text{GSM}}$ dimensions.

Because $M$ and $\tilde{M}$ represent the overlaps between SDs in the CQS and GSM bases, we can express the overlaps as [96–98]

$$\begin{aligned} M_{i,j} = \langle\Phi_i|\Psi_j\rangle &= \langle c|\, a_{i_n} a_{i_{n-1}} ... a_{i_1} b^\dagger_{j_1} ... b^\dagger_{j_2} b^\dagger_{j_n} \,|c\rangle \\ &= \begin{vmatrix} \langle\phi_{i_1}|\psi_{j_1}\rangle & \langle\phi_{i_2}|\psi_{j_1}\rangle & ... & \langle\phi_{i_n}|\psi_{j_1}\rangle \\ \langle\phi_{i_1}|\psi_{j_2}\rangle & \langle\phi_{i_2}|\psi_{j_2}\rangle & ... & \langle\phi_{i_n}|\psi_{j_2}\rangle \\ \vdots & \vdots & \ddots & \vdots \\ \langle\phi_{i_1}|\psi_{j_n}\rangle & \langle\phi_{i_2}|\psi_{j_n}\rangle & ... & \langle\phi_{i_n}|\psi_{j_n}\rangle \end{vmatrix} \end{aligned} \tag{5.22}$$

with the second line showing the overlaps between each one-body state making up the SDs.

Likewise, we can calculate

$$\begin{aligned}\tilde{M}_{i,j} = \langle\tilde{\Psi}_i|\Phi_j\rangle &= \langle c|\, b_{i_n} b_{i_{n-1}} ... b_{i_1} a^\dagger_{j_1} ... a^\dagger_{j_2} a^\dagger_{j_n}\, |c\rangle \\ &= \begin{vmatrix} \langle\tilde{\psi}_{i_1}|\phi_{j_1}\rangle & \langle\tilde{\psi}_{i_2}|\phi_{j_1}\rangle & ... & \langle\tilde{\psi}_{i_n}|\phi_{j_1}\rangle \\ \langle\tilde{\psi}_{i_1}|\phi_{j_2}\rangle & \langle\tilde{\psi}_{i_2}|\phi_{j_2}\rangle & ... & \langle\tilde{\psi}_{i_n}|\phi_{j_2}\rangle \\ \vdots & \vdots & \ddots & \vdots \\ \langle\tilde{\psi}_{i_1}|\phi_{j_n}\rangle & \langle\tilde{\psi}_{i_2}|\phi_{j_n}\rangle & ... & \langle\tilde{\psi}_{i_n}|\phi_{j_n}\rangle \end{vmatrix}\end{aligned} \tag{5.23}$$

which is crucial to get our basis-transformed $I_\Psi \mathcal{Q} I_\Psi = \tilde{M} M$. In the following generalized notation, any reference to $\mathcal{Q}$ should be taken as $\mathcal{Q}_\Psi$.

### 5.3.2 Implementation

Since both GSM and CQS wave functions are spherically symmetric, they have the general form of Eq. 2.6 and the primary difference is the radial wave function. Use of these occupation representation $M$ and $\tilde{M}$ operators then provides a convenient feature whereby the overlaps can be pre-computed on the s.p. level and the matrices can be built by taking determinants of these scalar values. Calculating these overlaps can be reduced further as each s.p. wave function overlap would contain

$$\begin{aligned}\langle\phi_i|\psi_j\rangle = \int_{r_{\min}}^{r_{\max}} \int_0^{2\pi} \int_{-1}^{1} &\frac{u^*_\phi(n,\ell,j,r)}{r} \frac{u_\psi(n',\ell',j',r)}{r} \\ &\times \left( \sum_{m_\ell, m_s} C^{jm}_{\ell m_\ell s m_s} Y^*_{\ell m_\ell}(\theta,\varphi)\, \langle s, m_s| \right) \\ &\times \left( \sum_{m'_\ell, s'_z} C^{j'm'}_{\ell' m'_\ell s' s'_z} Y_{\ell' m'_\ell}(\theta,\varphi)\, |s, m_s\rangle \right) r^2 d(\cos\theta) d\varphi dr,\end{aligned} \tag{5.24}$$

and generally for any spherical harmonic overlap

$$\int_0^{2\pi}\int_{-1}^{1} Y^*_{\ell m_\ell}(\theta,\varphi)Y_{\ell' m'_\ell}(\theta,\varphi)d(\cos\theta)d\varphi = \delta_{\ell\ell'}\delta_{m_\ell m'_\ell}$$

which leads to the reduced form of s.p. overlaps (noting that $\langle s, m_s|s', m'_s\rangle = \delta_{ss'}\delta_{m_s m'_s}$)

$$\begin{aligned}\langle\phi_i|\psi_j\rangle = \int_{r_{\min}}^{r_{\max}} u^*_\phi(n,\ell,j,r)u_\psi(n',\ell',j',r)dr \\ \times \sum_{m_\ell,m_s;m'_\ell,m'_s} C^{\ell s j}_{m_\ell m_s m_j} C^{\ell' s' j'}_{m'_\ell m'_s m'_j}\delta_{\ell\ell'}\delta_{m_\ell m'_\ell}\delta_{ss'}\delta_{m_s m'_s} = \\ \langle u^\phi_i|u^\psi_j\rangle \sum_{m_\ell,m_s;m'_\ell,m'_s} C^{\ell s j}_{m_\ell m_s m_j} C^{\ell' s' j'}_{m'_\ell m'_s m'_j}\delta_{\ell\ell'}\delta_{m_\ell m'_\ell}\delta_{ss'}\delta_{m_s m'_s}. \quad (5.25)\end{aligned}$$

For many of the precomputed s.p. overlaps the different values of the $\delta$ functions will be zero and this binary check can prevent any need to compute the radial integrals. Up until now, we have also been assuming nucleons of the same species but inclusion of isospin $T_z$ as an extra input quantum number produces the criteria $\delta_{T_z T'_z}$ between the two overlapped s.p. states.

After the s.p. overlaps are calculated and the $M$ and $\tilde{M}$ operators are computed, GSM results can be projected. An important feature of projection operators is idempotence, or that successive operations of a projection operator produce the same result as a single operation, $\mathcal{Q}\mathcal{Q} = \mathcal{Q}$. Due to potential numerical instabilities, it will be important to check amongst different operations that idempotence holds by

$$\mathcal{I}_\Psi = \langle\Psi_\nu|\mathcal{Q}\mathcal{Q}|\Psi_\nu\rangle - \langle\Psi_\nu|\mathcal{Q}|\Psi_\nu\rangle = 0 \quad \text{or} \quad \mathcal{I}_H = \langle\Psi_\nu|\mathcal{Q}\mathcal{Q}H\mathcal{Q}\mathcal{Q}|\Psi_\nu\rangle - \langle\Psi_\nu|\mathcal{Q}H\mathcal{Q}|\Psi_\nu\rangle = 0. \quad (5.26)$$

The complement operator $\mathcal{P}$ has the same idempotent criteria. The remaining choice one must make is which CQS basis to use to generate the projection operators.

### 5.3.3 Box Basis

Our basis of choice for the purposes of this work is a so-called "box basis" or a basis whereby we impose Dirichlet boundary conditions on our system. The primary effect of this choice is that any solutions to the radial wave equation $u$ must follow the boundary conditions $u(r = 0) = u(r = r_{\text{box}}) = 0$ at the origin and the edge of the box. From the perspective of an introductory quantum mechanics course, this would be the same as working from an infinite square well in spherical coordinates where the potential is zero inside the box and infinite beyond the $r_{\text{box}}$.

Infinite wells have a well-known property that the energy excitation spectrum follows a general relation $E \propto r_{\text{box}}^{-2}$ [99, 100]. A convenient result of this feature is the level of openness in the system can be directly controlled by the box radius, and in the limit as $r_{\text{box}} \to \infty$, the energy level spacing becomes infinitesimally small, a continuum limit. Another effect of changing box radius is that the number of low-lying energy states will increase and move down from the high-energy pseudo-continuum.

A limit to this basis choice is the stability of the low-lying wave functions which coincides with the energy of the states. To maintain consistency with the GSM contour, which represents the maximum energy cutoff, we only use states with energies of 400 MeV or lower (a typical cutoff value). While this limitation does not allow for a full representation from the box basis, we have found that the use of a few states is sufficient for projection.

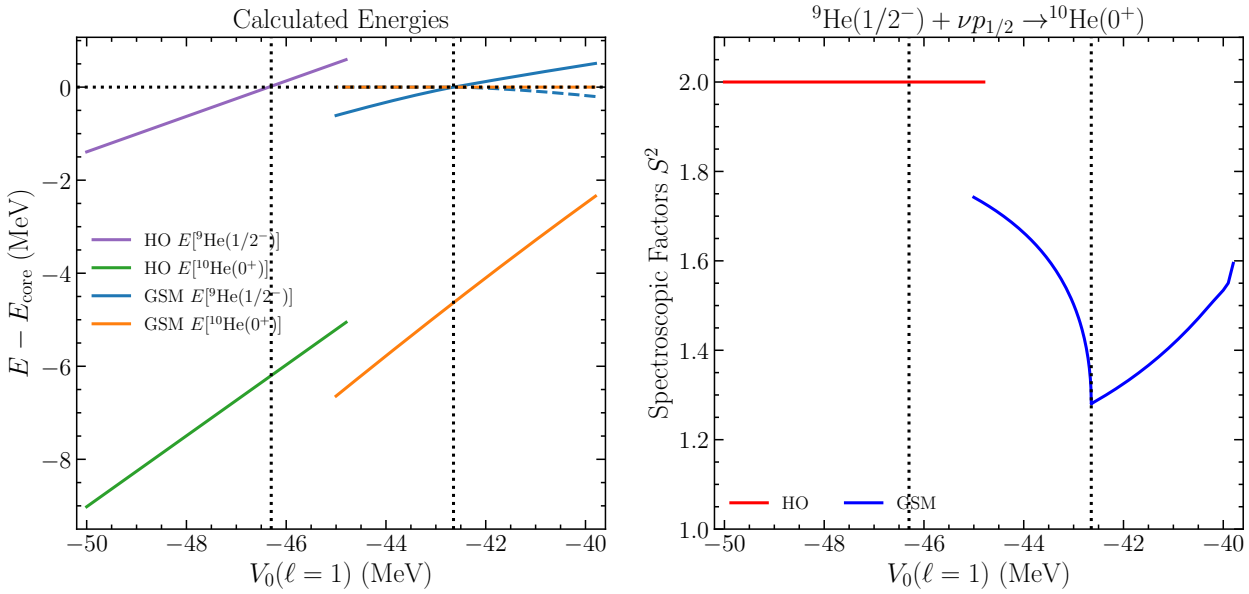


Figure 5.4: Energies for GSM and HO-SM basis calculations with respect to the WS depth $V_0$ associated with each calculation crossing threshold. Solid lines indicate real energy while dashed lines are for imaginary components (if applicable). Note the black dotted lines highlight where each calculation crosses threshold for the $^9\mathrm{He}(1/2^-)$ state. We highlight the lack of a discontinuity in the SF for HO-SM calculations.

## 5.4 Toy Problem

Before applying the projection code to realistic problems, the projection operator performance must first be benchmarked. To avoid cumbersome calculations, or potentially difficult to interpret results, we will consider a textbook example of the emergence of Wigner cusps (discontinuities in the SF) for a $^9\mathrm{He}{+}n \rightarrow ^{10}\mathrm{He}$ system as the WS depth parameter ($V_0$) is varied [5]. We show in Fig. 5.4 such effects where the SF becomes discontinuous across threshold only for the GSM (OQS) calculations. We note in Fig. 5.4 that there is a bend in the energy of $^9\mathrm{He}$ as a result of crossing threshold. This example was selected as it guarantees a system that exhibits threshold dependence. Additionally, this example is ideal for benchmarking since it uses a simplified model space consisting of only a single $0p_{1/2}$ basis pole, a $p_{1/2}$ discretized contour with 15 points per segment, and a $^8\mathrm{He}$ core.

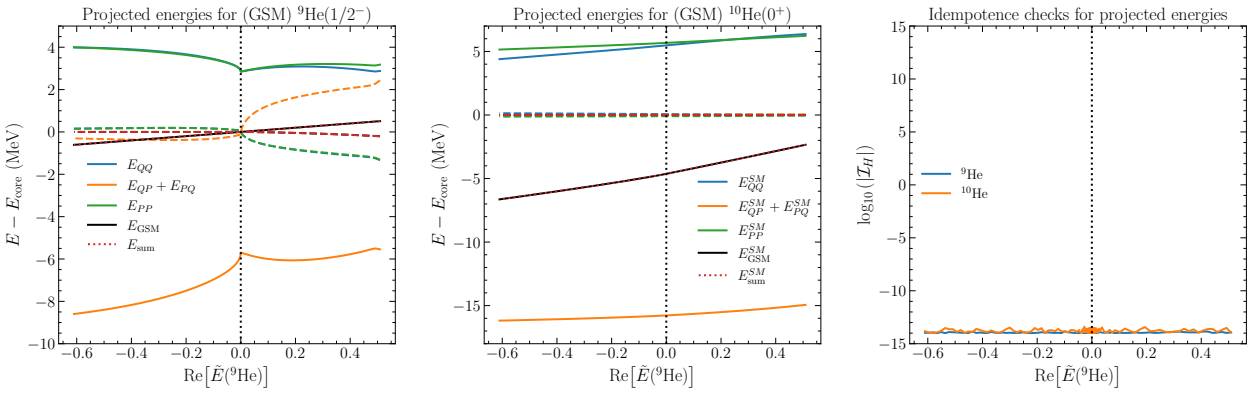


Figure 5.5: Projected energies for the considered nuclei. Solid lines indicate real energy while dashed lines are imaginary components. We show the idempotence check of Eq. 5.26 in the rightmost panel to verify the projection operators are idempotent. The projection operator $\mathcal{Q}$ was constructed using only the $0p_{1/2}$ box state at a box radius of $r_{\rm box} = 3.9$ fm.

While this model space is not a realistic representation for the structure for $^9$He or $^{10}$He, its simplicity will quickly identify if the projection operators capture threshold effects and remain idempotent.

Following the outline in Eq. 5.15, the projection operators can be applied to the Hamiltonian to obtain the projected energy components along with a check to ensure the operators are idempotent (Eq. 5.26). To start benchmarking with the simplest case, we will use only the lowest box state ($0p_{1/2}$) and a box radius of 3.9 fm to compute the projection operator. Previously, in Fig. 5.4, we noted that the GSM energies did not appear to have strong changes when crossing threshold, yet in Fig. 5.5 we can clearly see via the projected energies that effects from the continuum produce discontinuities. Moreover, we find that the continuum coupling energy is less than that of the SM or pure-scattering terms and serves as a binding effect when only considering this bound basis pole. Taking inspiration from Eq. 5.2, a similar continuum correlation energy can be obtained for each of the projected components

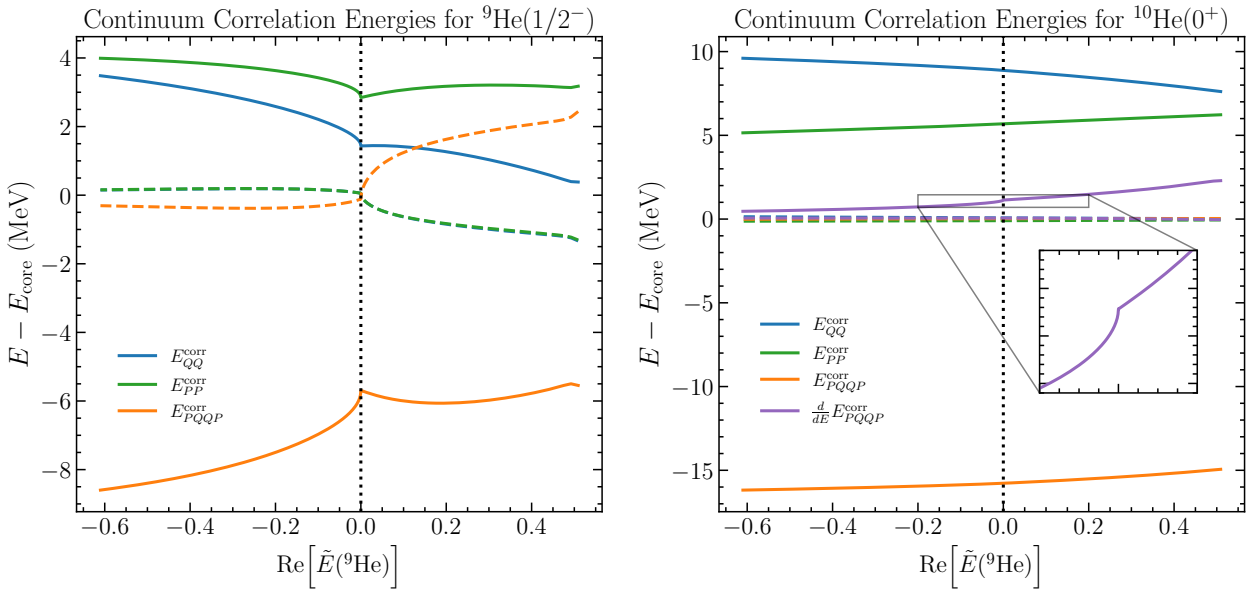


Figure 5.6: Projected continuum correlation energies for the considered nuclei. Color scheme, line styles, and box parameters are the same as in Fig. 5.5. We show the derivative of the correlation energy to highlight a discontinuity (inset) for the first order derivative in the coupling term for $^{10}$He.

(represented generically as $XX$) by

$$E^{\text{corr}}_{XX} = \langle \Psi(J^{\pi}) | H^{\text{GSM}}_{XX}(E) - H^{\text{CQS}}_{XX} | \Psi(J^{\pi}) \rangle \,. \tag{5.27}$$

In this form, the OQS and CQS components are projected onto the same subspace, allowing for a consistent description between the two quantities. This is analogous to taking the difference between the energy dependent Hamiltonian $\mathcal{H}_{QQ}(E)$ and the SM Hamiltonian $H_{QQ}$ in the SMEC formalism. In cases where the CQS effects across threshold are effectively constant, we see only slight changes in the projected continuum correlation energies as in Fig. 5.6.

As discussed in Sec. 5.3.3, the box basis has two adjustable parameters that control the representation of the $\mathcal{Q}$ space, the box radius $r_{\text{box}}$ and the number of excitations included $n$. Before applying our method to realistic systems, the effects of changing these two parameters

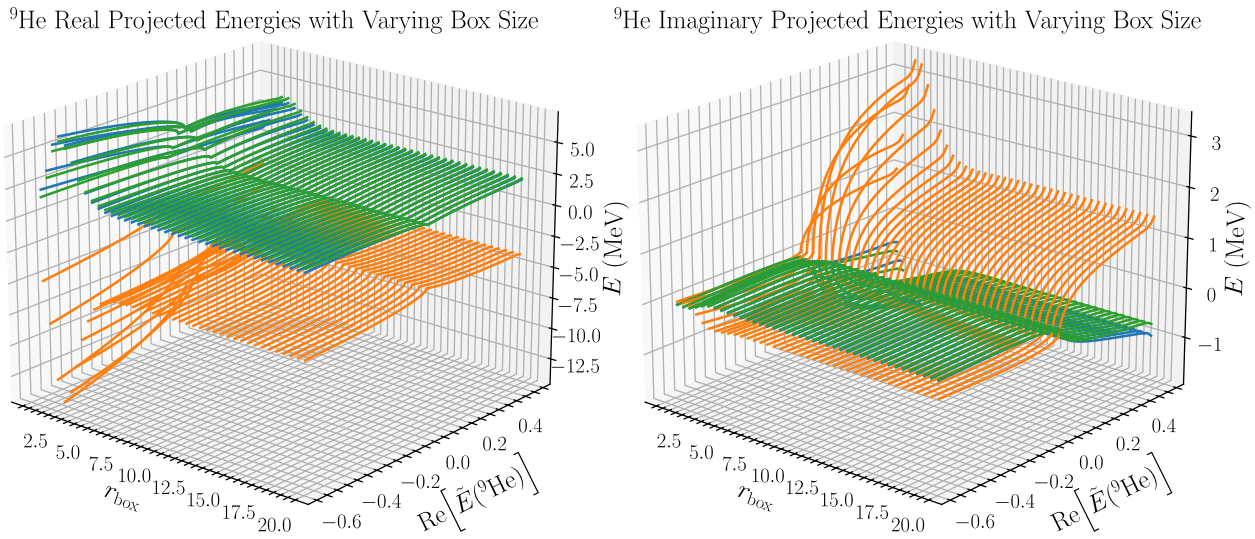


Figure 5.7: Projected energies using only the $0p_{1/2}$ bound s.p. box state at different values of box radius. Each set of lines belong to a plane corresponding to an $r_{\text{box}}$ value. The color scheme is the same as Fig. 5.5 where blue is $E_{\mathcal{QQ}}$, green is $E_{\mathcal{PP}}$, and orange is $E_{\mathcal{PQQP}}$. We see a general convergence of the values at larger box sizes.

must be benchmarked systematically. We will only focus on the impacts of the projection of the Hamiltonian only, as projecting SFs requires additional formulation of three different projection spaces corresponding to the parent, daughter, and free nucleon.

### 5.4.1 Benchmarking Box Radius Effects

Starting with the box radius, it was demonstrated in Sec. 5.3.3 that the behavior of the box basis states should follow an infinite square well. Since the box basis is generated using a WS plus Spin-Orbit (plus Coulomb for protons) potential with Dirichlet boundary conditions imposed, we should recover any bound states of the WS potential as long as $r_{\text{box}}$ extends far enough to allow the bound state(s) to form. For this toy system, there is one bound $0p_{1/2}$ pole; therefore, increasing $r_{\text{box}}$ should force the projected energies to converge to a specific value once the bound state is properly accounted for. Indeed, this is what is seen in Fig. 5.7 where the real and imaginary projected components stabilize.

While the convergence of the projection operators when using only bound states is a

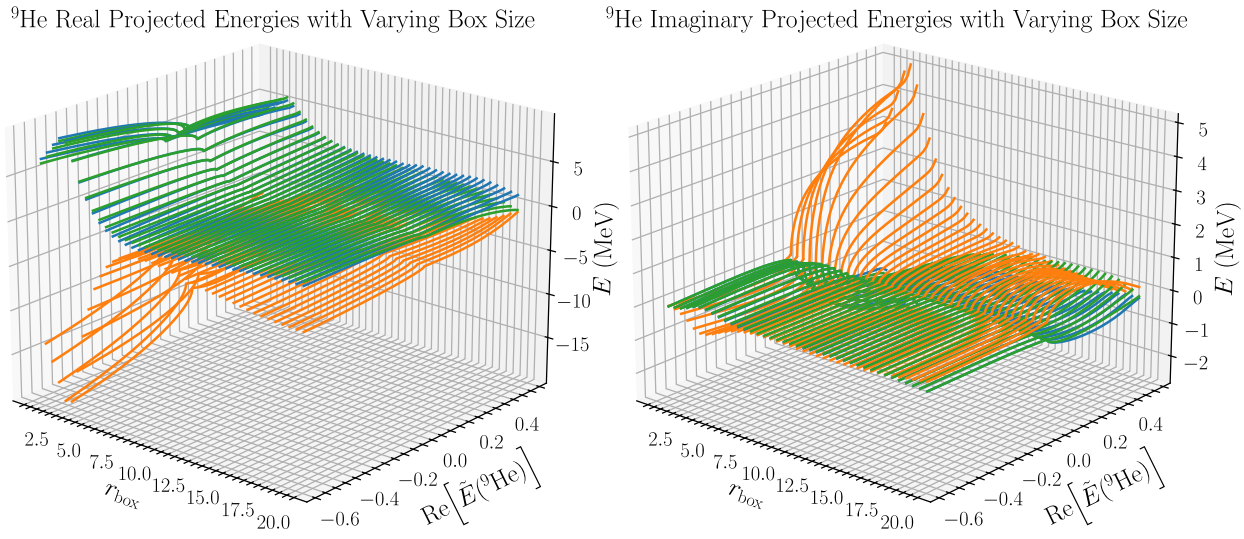


Figure 5.8: Projected energies using the lowest two box states ($0p_{1/2}$ and $1p_{1/2}$) at different values of box radius. We see that there is no convergence with increasing box radius. The color scheme is the same as Fig. 5.7.

helpful check, the question of how including higher-order box state excitations (pseudo-continuum states) will impact the projection operators still remains. In this case, one would not expect to have perfect convergence to a specific projected value as the pseudo-continuum (excited box) state will constantly change with box radius, recalling the behavior of an infinite well. Fig. 5.8 demonstrates this behavior as the inclusion of the next excited state causes fluctuations in the projected energies above threshold. For the $n = 1$ box wave function, the overall behavior does not vary significantly with $r_{\text{box}}$ since it is a pseudo-continuum state where the number of nodes of the wave function are directly tied to the infinite well representation. Despite the general line shape similarity, the fluctuations in the projected energies are a result of how well the box wave function for a given radius happens to coincide with the GSM s.p. scattering states. This is an obvious model dependence, but it is shared for many CQS models which use a fixed box boundary to represent a pseudo-continuum.

### 5.4.2 Benchmarking Box Excitation Effects

Since Sec. 5.4.1 has demonstrated that the projection operators return sensible results, so long as box radii are large enough to encompass the WS bound states, impacts and limitations on the number of box excitation states included can be investigated. Theoretically, there is no limit to the number of box state excitations one can include so long as the dimensionality of the box space does not exceed the GSM space. The same holds true for any projections onto a HO-SM calculation to obtain a continuum correlation energy from Eq. 5.27. As one can see in Eq. 5.21, if the dimensions change from $N_{\text{GSM}} > N_{\text{box}}$ to $N_{\text{GSM}} < N_{\text{box}}$ then $\mathcal{Q}_\Psi$ will project onto an overcomplete basis since the projection space exceeds the system space. In this extreme case, the calculation of Eq. 5.21 will likely result in a singular matrix or, at best, a collapse of idempotence.

In practice, numerical noise will exist and could lead to premature loss of idempotence of the projection operator. We checked this effect by performing a series of calculations of the toy model using a range of included maximum excitations. Fig. 5.9 illustrates the degree to which numerical noise impacts the projection operators. We see in this case that after including $n_{\text{max}} = 5$, the idempotence check increases orders of magnitude and it will become useless after a few more excitations are included. This problem is also present for the $^{10}$He case where the changes in the idempotence check magnitude are even sharper. Constant checking of the idempotence is imperative as Fig. 5.9 illustrates the system behavior may not provide obvious indications to the increased loss of idempotence. Thankfully, these higher excited states at the current box radius coincide with energies far above the typical GSM energy cutoff. Moreover, the goal of using box states in our projection operator were to reliably capture any CQS behavior, not have the $\mathcal{Q}$ space reproduce the genuine continuum

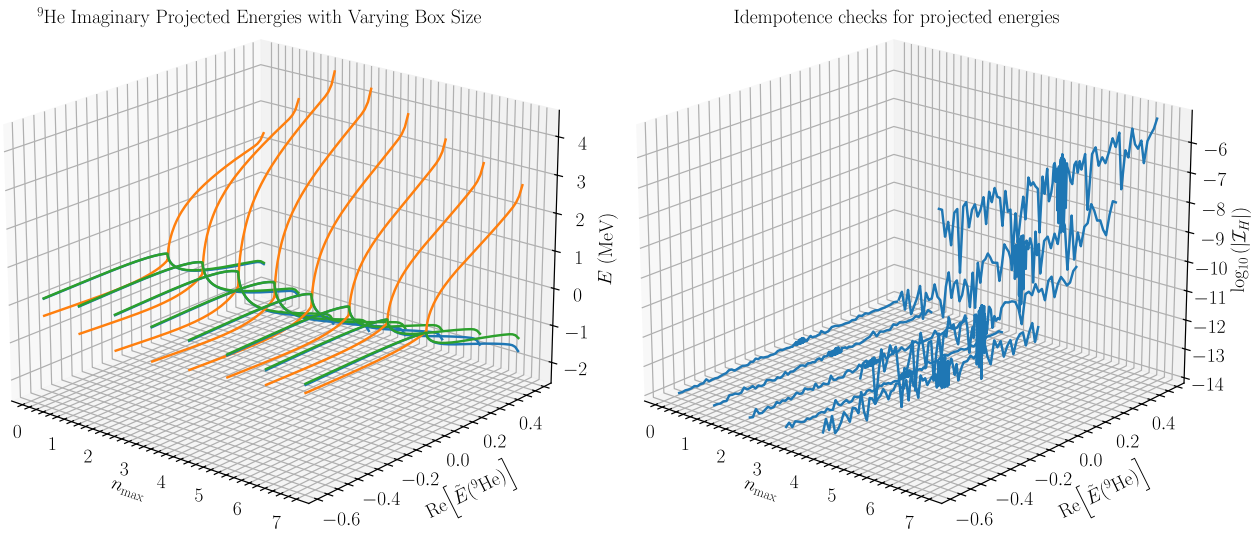


Figure 5.9: (Left) Projected imaginary energies including an increasing number of excitations from the box basis at a consistent $r_{\mathrm{box}} = 4$ fm. (Right) We note that after including more excited states, idempotence will fail.

states.

## 5.5 Realistic Nuclei

For an initial test of GSM projection in a realistic case, we selected the nuclei $^5$He and $^6$He which are constructed with valence neutron(s) on a $^4$He core. These two nuclei have been studied frequently with methods using the Berggren basis [27–29, 31, 37, 101, 102] and one-body WS and two-body FHT interactions have been calibrated for these nuclei [31, 37]. For this work, the model space will be reduced to include only $p_{1/2}$ and $p_{3/2}$ states which are necessary to reproduce the states in $^5$He and are sufficient for calculations of $^6$He. The contours will be discretized with 27 points (9 per segment) with the points $k_{\mathrm{peak}} = (0.3, -0.3)$, $k_{\mathrm{mid}} = (0.9, 0.0)$, and $k_{\mathrm{max}} = (4.0, 0.0)$. One-body and two-body parameters are taken from Ref. [31], as we will use a WS core-nucleon and FHT nucleon-nucleon interaction.

To determine the effects different thresholds have on $^5$He and $^6$He, we again vary the WS depth $V_0$ to transition from artificially bound to unbound cases as shown in Fig. 5.10. This realistic case provides a new stress-test of the projection operators as it includes different

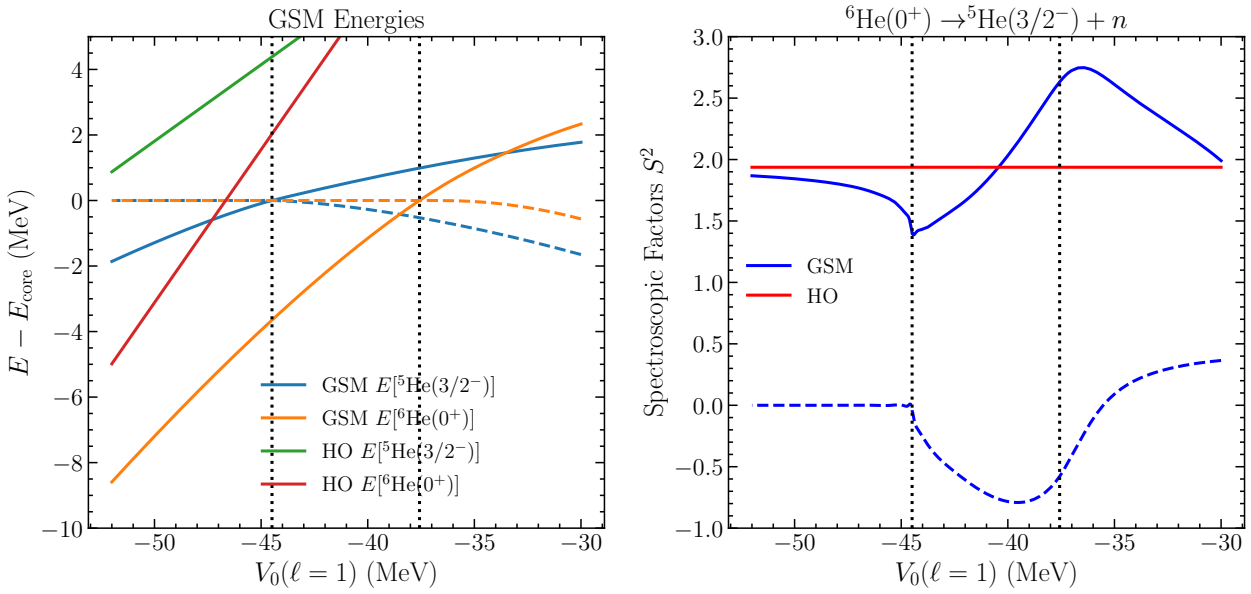


Figure 5.10: Left: Calculated energies for the ground states of $^5$He and $^6$He. We show the real (solid) and imaginary (dashed) parts as well as the two thresholds for $^5$He and $^6$He respectively as vertical dotted lines. Right: SFs calculated in GSM with varying WS depth.

$j$ basis states which compete in the structure of the $A = 6$ system. We highlight that this case also provides two thresholds to study, the transition from bound to unbound for $^5$He and for $^6$He. Furthermore, the behavior of $^6$He is that of Borromean system which decays by $2n$ emission since $^5$He is neutron unbound [40, 54, 103, 104]. At each threshold, we expect the projected components to reveal qualitative energy changes in the system as the wave functions will transition from being effectively describable with Dirichlet conditions to outgoing asymptotics. Fig. 5.11 depicts the effects of projection using only the lowest energy basis poles for the considered partial waves. Again, specific behaviors appear that were also seen in the toy problem when including only bound states in $\mathcal{Q}$, such as a coalescence of two projected components ($\mathcal{Q}$ and $\mathcal{P}$) at threshold and the binding effect of the coupling term $E_{\mathcal{PQQP}}$. This behavior continues for the excited $^6$He($2^+$) state which is shown in Fig. 5.12. The excited state of $^5$He is unbound for the entire domain of the considered $V_0$ parameter, yet the excited state in $^6$He retains the desired threshold crossing feature. For

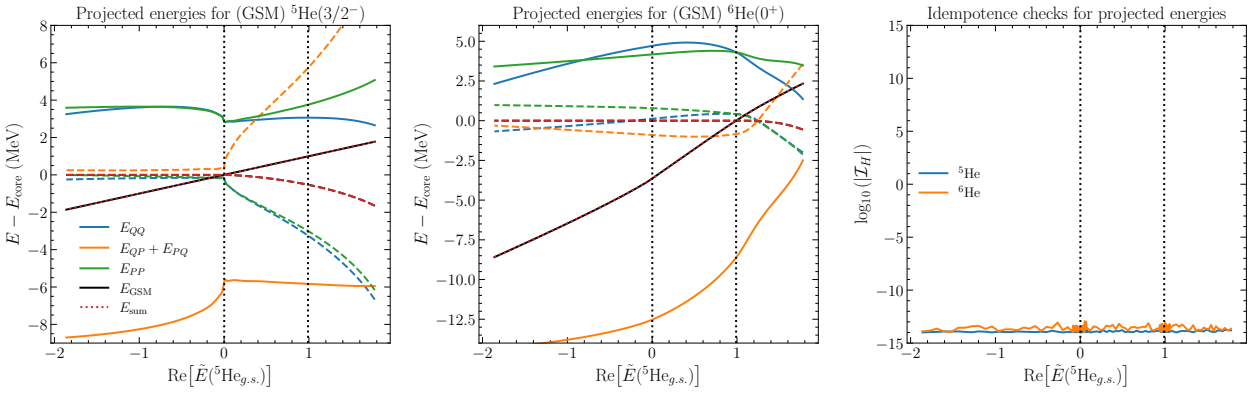


Figure 5.11: Projected ground state (g.s.) energies using the lowest box states ($0p_{1/2}$ and $0p_{3/2}$) at $r_{\rm box} = 4$ fm. We show the two thresholds for $^5$He and $^6$He respectively as vertical dotted black lines. The center and left plots use the same legend.

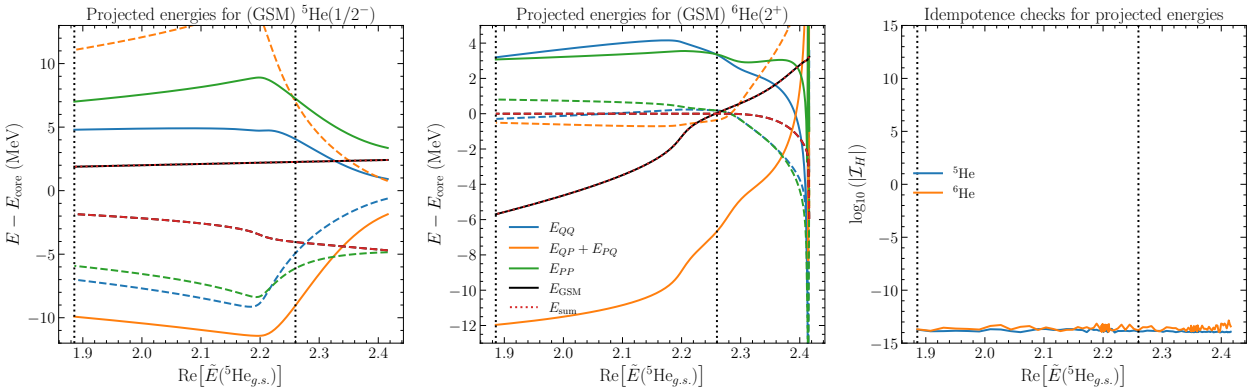


Figure 5.12: Projected first excited state energies using the lowest box states ($0p_{1/2}$ and $0p_{3/2}$) at $r_{\rm box} = 4$ fm with respect to the $^5$He g.s. energy. We show the two thresholds for $^5$He and $^6$He respectively.

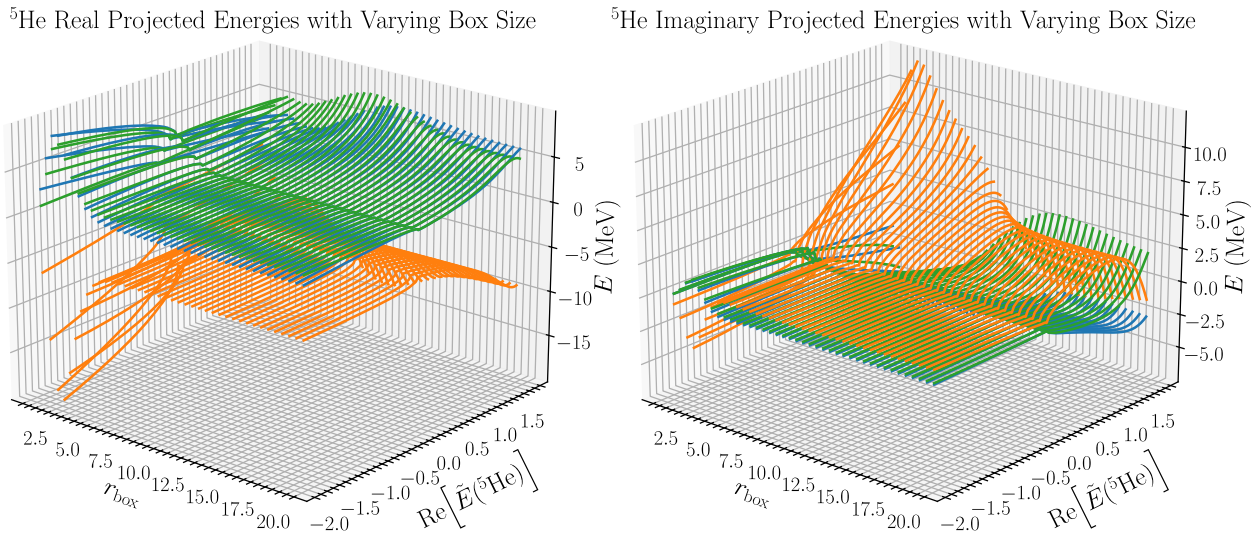


Figure 5.13: Variation of box radius from $r_{\text{box}} = 1$ to $r\text{box} = 20$ fm. Projected energies for the ground state of $^5$He were obtained using the lowest box states ($0p_{1/2}$ and $0p_{3/2}$).

the unbound $^6\text{He}(2^+)$, we note that at shallow values of $V_0$ the state was not well-converged ($|H\,|\Psi_\nu\rangle - E\,|\Psi_\nu\rangle\,| > 0.5$ MeV) and this is represented in Fig. 5.12 at larger values of $^5\text{He}_{g.s.}$. Despite the lack of convergence in the GSM calculations, the projection operators still function well and have little loss in idempotence. Moreover, ignoring the convergence issues, the resonant state clearly dissolves into the continuum due to the large imaginary term, yet the projected components still handle these sharp changes well.

We follow the toy model checks to diagnose the stability of the projection operators in this realistic case. The results of varying the box radius are plotted in Fig. 5.13 and the impact of changing the number of box excitations included in the projection operator are shown in Fig. 5.14 for the ground states only. These checks are consistent with what was observed in the toy model. Specifically, there is convergence of projected components to certain values when using only bound states in $\mathcal{Q}$ with large box radius, and a loss of idempotence is observed when including higher-lying excited box states in the projection operator. Both checks illustrate that the projection operators, even in realistic cases, can

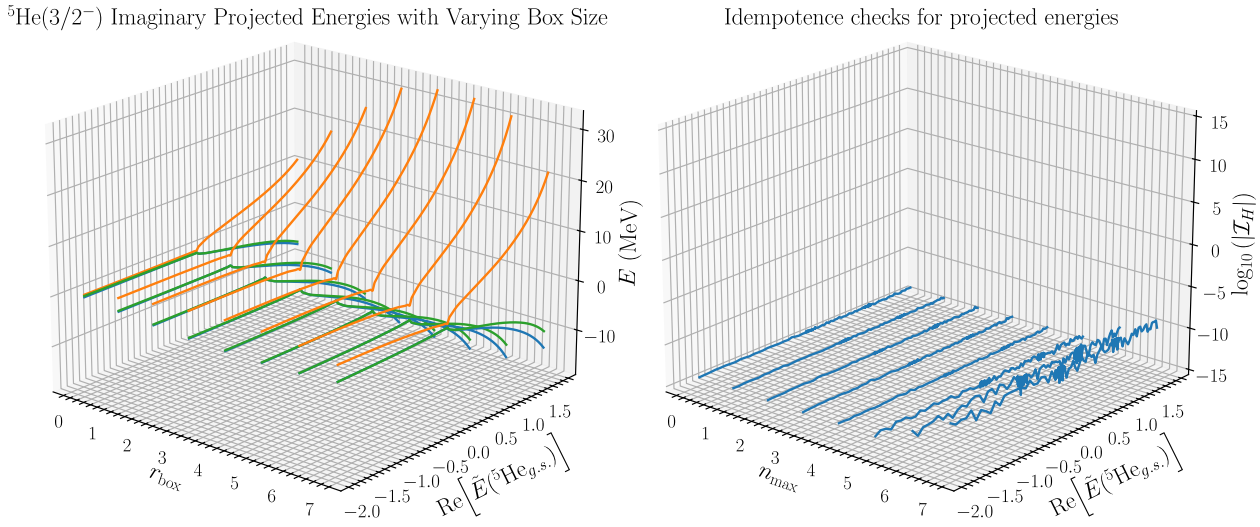


Figure 5.14: Variation of box excitations included from $n = 0$ to $n = 7$. Projected energies for the ground states were obtained using a box radius of $r_{\text{box}} = 4$ fm. To maintain readability, only the imaginary part is shown.

reliably provide quantified continuum coupling using localized states and the inclusion of pseudo-continuum states ($E > 0$ in the CQS case) is feasible but requires constant checking of the idempotence. Additionally, with any variation in either box radius or excitations included, the resulting effects on projected energies appear to pivot about the corresponding threshold of the system. This indicates that these projection operators respect the thresholds in GSM.

## 5.6 Conclusions

Using a set of states generated with Dirichlet boundary conditions, we have demonstrated that projection of continuum effects in GSM using a CQS basis is possible and determined possible limitations to this approach. In principle the choice of projection basis is arbitrary, but in practice the set of states used to generate the projection operator should vary consistently in a parameter space. Further investigations into other realistic systems should be done across different shells such as $^{17,18}$O or $^{41,42}$Ca. Investigating these systems will reveal if the behaviors noted in this work appear across the nuclear landscape, and these general

features may provide more insight into generic continuum effects. Since these systems will require different model spaces of higher $\ell$ states, one can probe other threshold effects. For example, Wigner cusps do not manifest for $\ell > 1$, but discontinuities will appear at higher order derivatives of the SFs. The order of derivative follows the trend of $\ell - 1$ so cusps appear in $\ell = 2$ states at first order derivatives and at second order for $\ell = 2$ [54, 105].

Other methods to extract continuum energy correlation factors, like in Ref. [106] which allow for direct probing of effects such as aligned states, would be complementary to this work. Direct comparison between such approaches and this projection method should be done to qualitatively understand how continuum coupling impacts nuclear structures. Additionally, combinations of OQS models can be used to provide insight into specific features. We have shown in this work that topics including SF suppression (Ch. 3) and the structure of ephemeral nuclei (Ch. 4) are strongly dependent on the continuum. Using the suite of specialized methods to extract specific aspects of continuum coupling should be used to better quantify the nature of the continuum. In the case of exotic resonant states, like antibound states, the use of these projection techniques could also be used to highlight deficiencies in a CQS basis by generating a projection operator from a chosen basis.

# Chapter 6. Hands-on Nuclear Structure and Decays

Nuclear science is an ever-evolving field which greatly benefits from new perspectives, and improving accessibility and inclusivity is crucial its continued development [1]. Simultaneously, pushes to improve the public's scientific literacy and increase engagement with students will be crucial for both maintaining public support of scientific programs and for developing future workforces. To this end, we have developed a new demonstration [107] that highlights nuclear structure and decays while aiming to be accessible to a wide audience. Nuclear phenomena are illustrated in this demonstration by layering wooden blocks with a fixed set of rules emulating nuclear shells.

Providing audiences with opportunities to engage with nuclear science can be difficult due to the microscopic size of nuclei. Constan developed [108] a method for explaining reaction mechanisms in accelerator facilities using magnetic marbles, and highlighted the possible products that can be made from the impact of two nuclei. Whittaker created a demonstration using magnetic disks to describe static nuclear properties from a quark level [109]. While both highlight crucial aspects of nuclear formation, building from the quark level and illustrating statistical reaction processes, there is a gap in the literature focusing on time-dependent processes like decay. Our demonstration seeks to address this gap by allowing nuclei to be built from a nucleon level and introducing mechanisms of decay such as $\gamma$-decay, $\beta^{\pm}$-decay, $\alpha$-emission, and nucleon emission. Fission is not explored in this demonstration as it occurs in heavy nuclei which have large numbers of nucleons, a scale that is not conducive for this demonstration.

This chapter contains work submitted to *The Physics Teacher* and is currently under

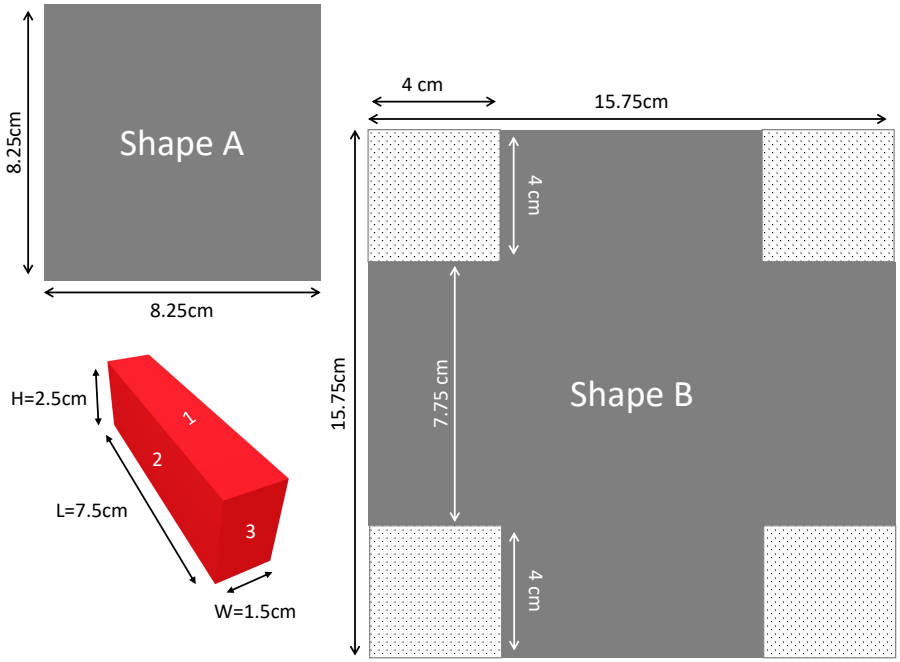


Figure 6.1: Diagram of dimensions for the required blocks and cardboard support pieces. Nuclear magic numbers are represented by shape A (for the 2 shell closure) and shape B (the 8 and 20 shell closures). Sides referenced for each block are as shown in the given label.

review [107]. Authors of that manuscript are Joshua Wylie, Pablo Giuliani, Kyle Godbey, and Sylvester Agbemava.

## 6.1 Rules

First, we define the basic properties of the demonstration before discussing the physics concepts covered. The materials required for the demonstration are 1.5cm  2.5cm  7.5cm wooden blocks, with at minimum 20 painted red (protons) and 28 painted blue (neutrons), and cardboard shapes cut to the specifications in Fig. 6.1.

The demonstration can be done individually or in a competitive format. In either case, a set of base rules exists that one must follow, and these are represented in Fig. 6.2 but are also listed (block sides are labeled in Fig. 6.1):

1. Protons: Must lay on side 1, be spaced $\approx$ 2 cm apart, and be parallel to each other.

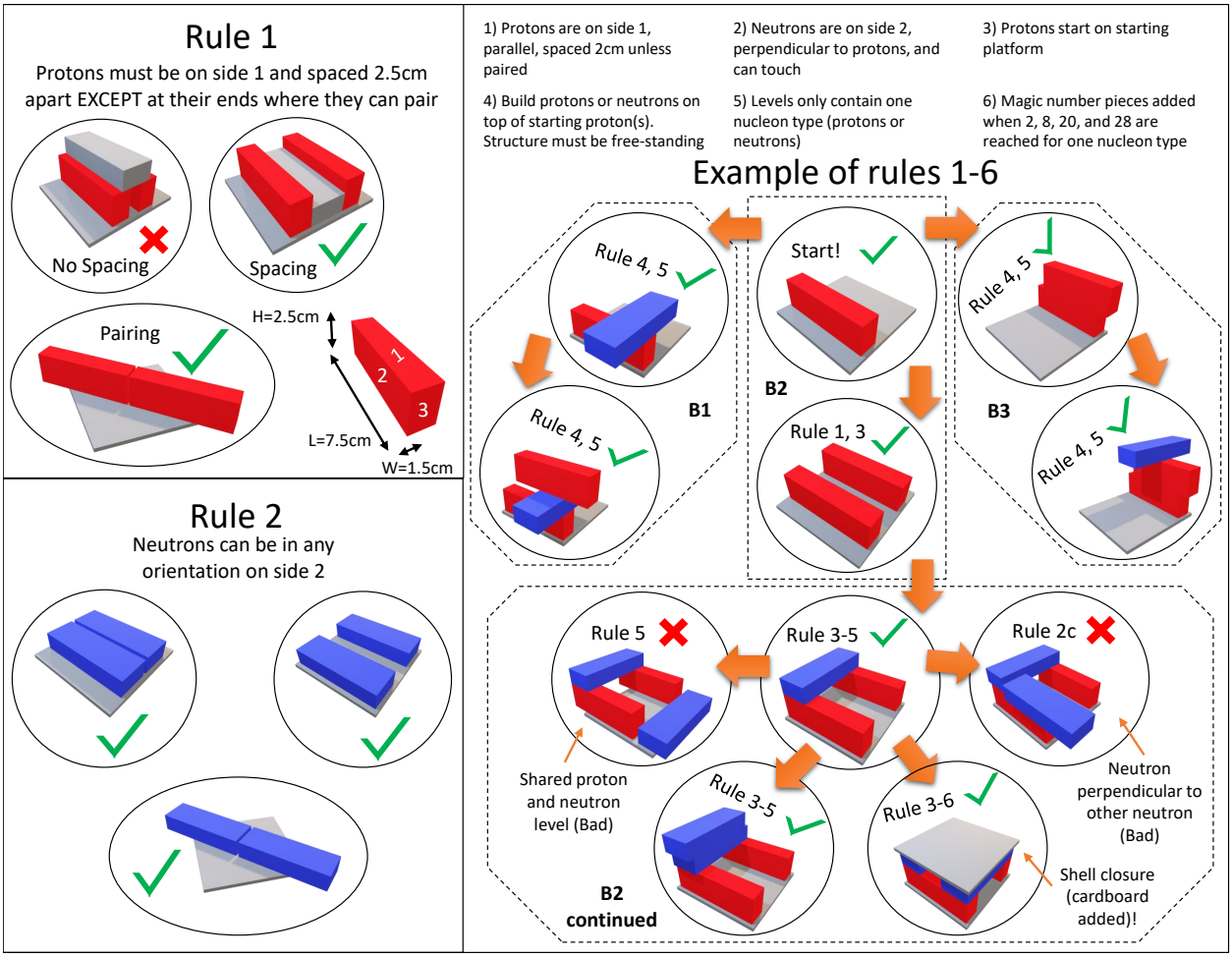


Figure 6.2: Rules of the demonstration accompanied by pictorial representations. We provide a few starting scenarios to illustrate allowed and forbidden actions within the rules.

Pairing between two protons is allowed by having sides 3 join together.

2. Neutrons: Must lay on side 2 and can touch in any configuration, but they must be parallel to one another *and* perpendicular to protons.
3. The demonstration must begin with placing one proton on the starting platform, shape A.
4. Subsequent nucleons may be added atop this platform or the starting proton respecting rules 1-3.
5. Each level can contain only one nucleon species, and no more than two sequential levels of nucleons of the same species can be on top of each other.
6. When enough nucleons have been added, a player may add a magic number cardboard stabilizer to the structure.
7. (Optional) Each level of protons or neutrons has a maximum number of blocks allowed.

Isospin symmetry and the presence, or lack, of Coulomb effects due to charge are represented in the first two rules. Rules 3 and 5 ensure that stable neutron matter or extremely neutron-rich matter is not a possible outcome of the demonstration. While rule 7 best mimics the general SM scheme, see Fig. 6.3, it can be complex for younger participants and left optional. We allow participants to vary the level order (regardless of adherence to rule 7) so they may represent other nuclear features like islands of inversion.

Finally, after a nucleus has been constructed, and assuming that the nucleus has not yet collapsed, one can introduce vibrations to the table the nucleus sits on to simulate the effects of quantum mechanics. The introduction of these effects might induce a decay, where a nucleon changes orientation, falls, or the entire structure collapses. It is recommended that participants use something which vibrates the table as a constant frequency and varying amplitudes to illustrate nucleon motion over time at different energies. If such a tools is

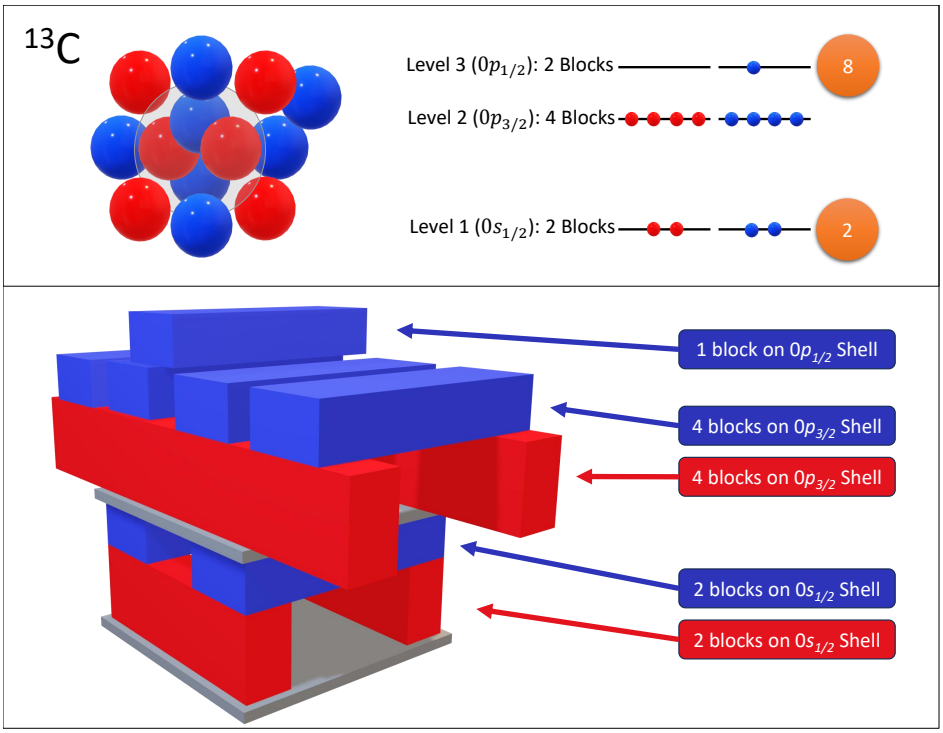


Figure 6.3: Example of $^{13}$C structure in relation to a schematic SM picture.

unavailable, participants can carefully shake or hit the table to accomplish the same purpose. After introducing quantum effects (vibrations) participants will notice some structure survive the process while others decay. The goals are to either (1) build the largest, most stable, nucleus or (2) build the most exotic nucleus. For the purposes of this demonstration, "exotic" is defined as nuclei with strong isospin asymmetry such as $^{8}$C or $^{28}$O. Excited states can be produced by promoting one nucleon to a higher level as depicted in the side branches B1 and B3 of Fig. 6.3.

Additional rules for a competitive version between multiple participants can also be implemented, and these rules are:

1. Using only one hand, and not touching any additional blocks, players may (a) place a new nucleon onto the nucleus or (b) excite an existing nucleon by moving it to a higher level than its current position.

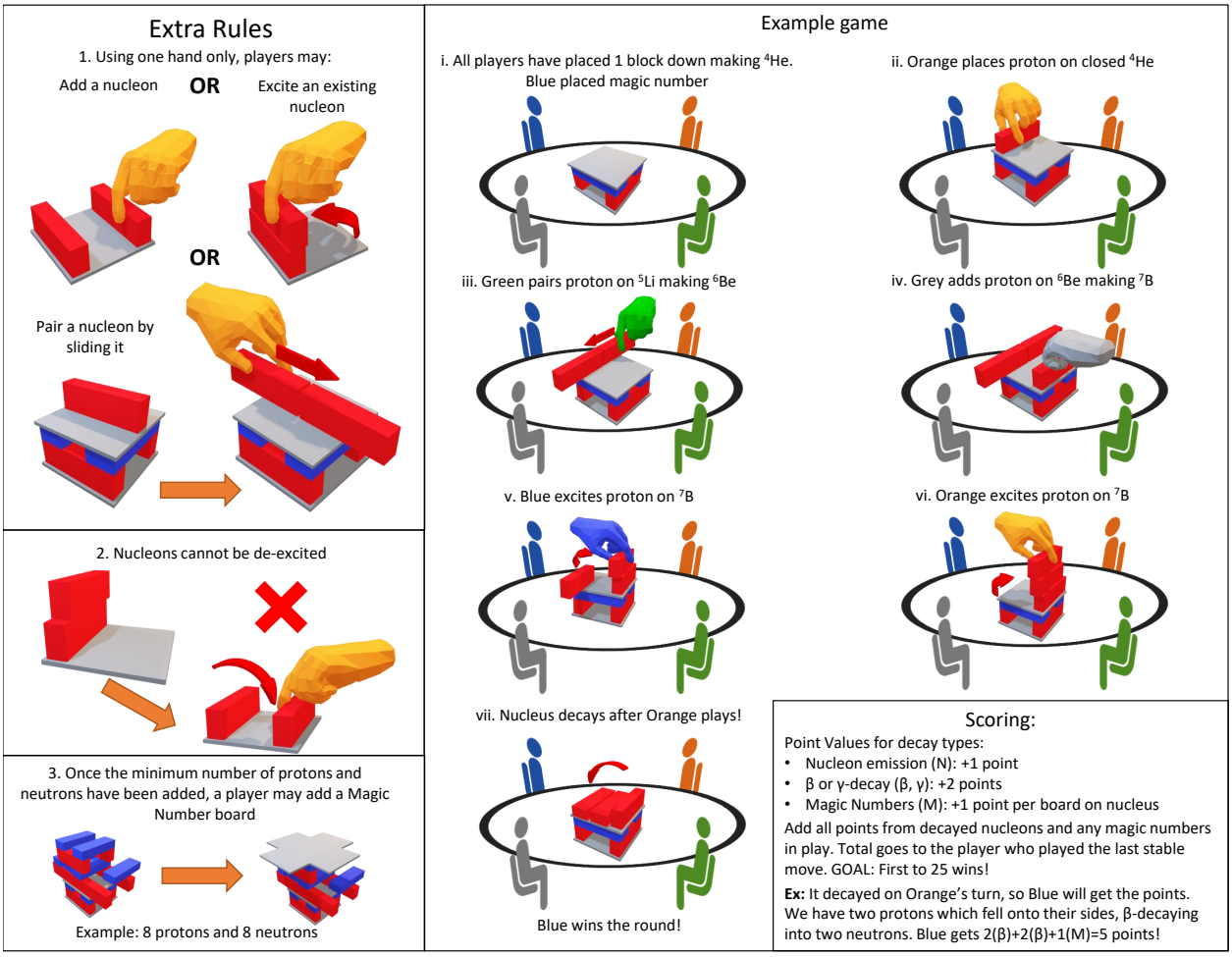


Figure 6.4: Depiction of additional competitive rules including an illustration of scoring a round.

2. Nucleons cannot be de-excited (moved to a lower level).
3. Once the proper nucleon number requirement is met, a player may use their turn to place a magic number board instead of a nucleon.
4. (Optional) Nucleons cannot be added to levels below a magic number board unless it is to replace a vacancy left by an excited nucleon.

Examples of these additional rules are provided in Fig. 6.4. A scoring mechanism is also included to encourage participants to play multiple rounds and to cleverly create unstable nuclei. Points are awarded to the player which made the last stable move. Points are assigned

as follows and ends once a player has reached 10 points:

- Nucleon emission: One or more nucleons fall completely off of the nucleus (1 point).
- $\beta$-decay: A nucleon falls down to a lower level of the opposite nucleon type or onto the opposite side it started on, i.e. a proton falls landing on side 2 changes to a neutron (2 points).
- $\gamma$-decay: A nucleon falls down to a lower level of the same nucleon type or falls onto the same side it started on, i.e. a proton falls landing on side 1 remains a proton (2 points).
- Additional points are added onto the decay score for each Magic Number board on the nucleus.

Extra points are assigned to decays which are less likely to occur based on the nature of the demonstration, as (multi-)nucleon emission is the most likely.

## 6.2 Concepts

As outlined in Sec. 6.1, we retain simple rules associated with protons and neutrons. This is done to avoid any misconceptions that nuclei form in a sterile environment, contrary to the dynamic processes in which they actually form, like in stars. Furthermore, capturing emergent behavior from simple rules highlights the ideal balance of maintaining model simplicity and predictability.

Nucleonic properties are the first focus of this demonstration. We assert that there are two species of nucleons, one of which can only be near others of the same species as pairs. Participants may easily recognize this importance as it is associated with electric charge, which can be compared to the repulsive effects when placing two magnets of the same alignment near each other. Starting from these Coulomb and general fermionic properties, one

can explore a variety of phenomena related to the nuclear chart. Participants frequently question why the nuclear chart bends to favor an excess of neutrons rather than a constant $N = Z$ trend. By imposing or neglecting the proton spacing rule (Coulomb effects), participants determine that the repulsive nature leads to favoring neutron excess when building larger nuclei ($^{40}$Ca or larger). We developed and provide a companion website [110] which includes a feature to highlight this deviation.

Aside from nucleon properties, nuclear shells are another incredibly important concept to nuclear structure. Since the introduction of the SM by Maria Goeppert Mayer [111] to address the presence of magic numbers (also highlighted in the companion website [110]), many other phenomena have been associated with the presence of shells. This demonstration allows participants to follow general shell structure to understand how specific shell orderings change the accessible nuclei. For example, following the exact level scheme provided, participants may be able to build $^{48}$Ca with ease, yet other exotic nuclei may be difficult to construct. When participants alter the shell ordering, creating islands of inversion, they find some nuclei are easier to build. By utilizing the shell structure in this demonstration, describing excited states becomes a natural extension by allowing lower-lying blocks to be moved to a higher level. The competitive version in particular encourages such promotion and can produce some nuclear structures that will not normally be constructed in an isolated (single-player) view. Promotion of nucleons, or other unstable moves, by other participants provides an ideal example of external environmental impacts on nuclear structure (OQS).

Lastly, decays are a natural feature of this demonstration. In the cases where the tower remains stable, requiring additional energy to break it, participants will identify that some configurations are stronger than others. Even for towers containing the same number of nucleons, different configurations (ground states or excited states) will be associated with

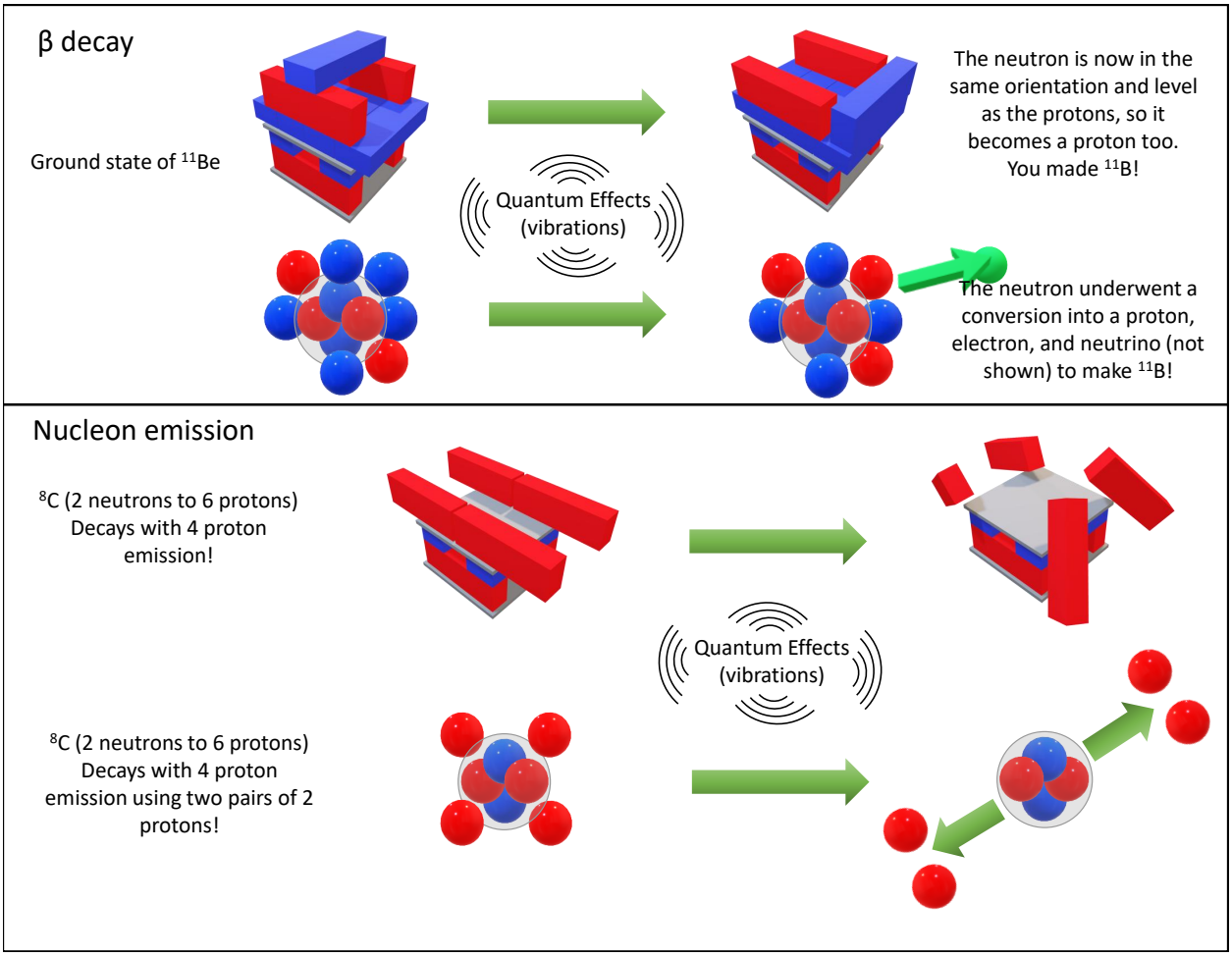


Figure 6.5: Depictions of two decay modes in the context of this demonstration and relation to the corresponding decay mode.

different levels of stability. For cases where the nuclear towers do undergo a decay, participants can learn more about the systems. By leaving holes in lower levels, participants may learn that some decays become more favorable, such as $\beta^{\pm}$ or $\gamma$-decays. They can recognize that different configurations are more likely to produce desired decay properties. These decays are illustrated in the context of the demonstration in Fig. 6.5. A full view of all decay modes in this demonstration are illustrated in Fig. 6.6 and found on the companion website [46]. $\gamma$-decays occur in the demonstration by a nucleon falling from an elevated level onto its original orientation, whereas a $\beta^{\pm}$-decay arises from a change in orientation. Both require

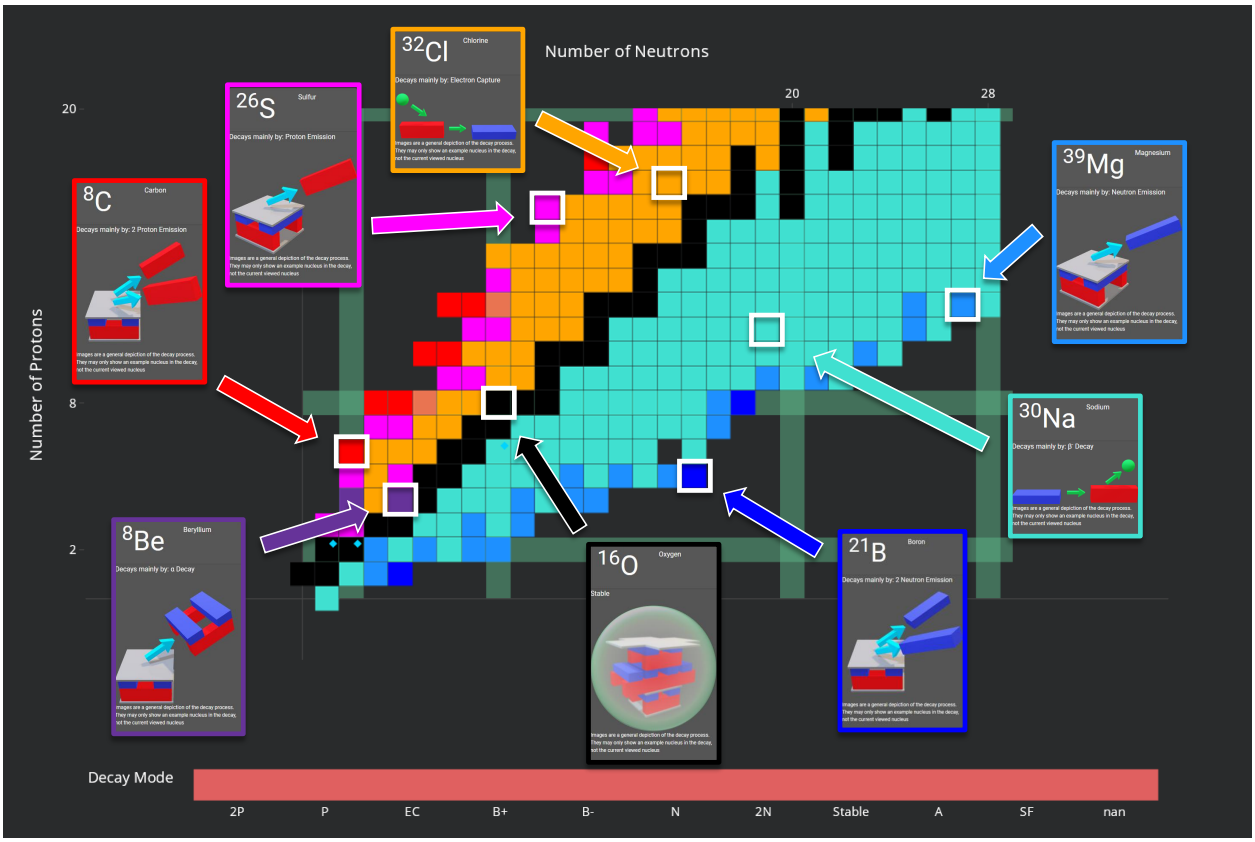


Figure 6.6: Screenshot of companion website with all decay modes higlighted for example nuclei.

that the nucleon remain on the nuclear tower. Conversely, (multi-)nucleon and $\alpha$-emission explicitly require the nucleons to fall completely off of the nucleus. We find these decay processes occur within the demonstration. A final mechanism which participants can consider is partial or total disintegration, whereby part or the entire nuclear tower collapses. This can be related to catastrophic events which will destroy much of the original nucleus such as photodisintegration. Typically such events will require significant energy from vibrating the surface the tower rests on.

## 6.3 Conclusions

As we have demonstrated in this work, nuclear shell effects and decay properties dramatically impact nuclear structure. This demonstration was inspired to describe both of these aspects, similar to how GSM describes structure and reaction properties simultaneously. Using simple rules mimicking nucleon properties such as Coulomb effects, the Pauli exclusion principle, and fermionic pairing we can reproduce many emergent behaviors seen in atomic nuclei. Through this hands-on activity, we aim to improve the accessibility of nuclear physics for the general public to improve scientific literacy and serve as a new tool for community engagement and outreach.

# BIBLIOGRAPHY


[1] *A New Era of Discovery: The 2023 Long Range Plan for Nuclear Science*. Tech. rep. USDOE Office of Science (SC) (United States), Oct. 2023. DOI: 10.2172/2280968.

[2] http://www.nndc.bnl.gov/ensdf. 2015.

[3] P. Daya. *What are Isotopes? — IAEA*. 2022. URL: https://www.iaea.org/newscenter/news/what-are-isotopes.

[4] L. Neufcourt et al. "Quantified limits of the nuclear landscape". In: *Phys. Rev. C* 101.4 (Apr. 2020), p. 044307. DOI: 10.1103/PHYSREVC.101.044307/.

[5] N. Michel and M. Płoszajczak. *Gamow Shell Model: The Unified Theory of Nuclear Structure and Reactions*. Vol. 983. Cham, Switzerland: Springer, 2021. DOI: https://doi.org/10.1007/978-3-030-69356-5.

[6] S. Liddick and A. Spyrou. *Powerful linear accelerator begins smashing atoms – 2 scientists on the team explain how it could reveal rare forms of matter*. 2022. URL: https://theconversation.com/powerful-linear-accelerator-begins-smashing-atoms-2-scientists-on-the-team-explain-how-it-could-reveal-rare-forms-of-matter-185754 (visited on 02/08/2025).

[7] A. Spyrou and S. Liddick. *Many stable atoms have 'magic numbers' of protons and neutrons – 75 years ago, 2 physicists discovered their special properties*. 2024. URL: https://theconversation.com/many-stable-atoms-have-magic-numbers-of-protons-and-neutrons-75-years-ago-2-physicists-discovered-their-special-properties-239690 (visited on 02/08/2025).

[8] B. A. Brown. "Lecture Notes in Nuclear Structure Physics". 2022. URL: https://people.frib.msu.edu/~brown/xx/brown-lecture-notes-2022.pdf.

[9] C. W. Johnson et al. "White paper: From bound states to the continuum". In: *J. Phys. G* (2020), pp. 1–57. DOI: 10.1088/1361-6471/abb129.

[10] M. Schlosshauer. "Quantum decoherence". In: *Physics Reports* 831 (2019), pp. 1–57. DOI: 10.106/j.physrep.2019.10.001.

[11] H. E. Brandt. "Qubit devices and the issue of quantum decoherence". In: *Prog. Quantum Electron* 22.5-6 (1999), pp. 257–370. DOI: 10.1016/S0079-6727(99)00003-8.

[12] A. Volya et al. "Superradiance in alpha clustered mirror nuclei". In: *Communications Physics 2022 5:1* 5.1 (Dec. 2022), pp. 1–6. DOI: 10.1038/s42005-022-01105-9.

[13] R. H. Dicke, P. Physical, and I. Aboratory. "Coherence in Spontaneous Radiation Processes". In: *Physical Review* 93.1 (Jan. 1954), p. 99. DOI: 10.1103/PhysRev.93.99.

[14] S. M. Wang et al. "Probing the nonexponential decay regime in open quantum systems". In: *Physical Review Research* 5.2 (Apr. 2023), p. 023183. DOI: 10.1103/PHYSREVRESEARCH.5.023183/.

[15] V. ZELEVINSKY and A. VOLYA. "SUPER-RADIANCE: FROM NUCLEAR PHYSICS TO PENTAQUARKS". In: *Key Topics in Nuclear Structure*. World Scientific Pub Co Pte Lt, 2005, pp. 585–594. DOI: 10.1142/9789812702265_0064.

[16] N. Michel et al. "Shell model in the complex energy plane". In: *J. Phys. G* 36.1 (2009). DOI: 10.1088/0954-3899/36/1/013101.

[17] J. Dobaczewski et al. "Shell structure of exotic nuclei". In: *Prog. Part. Nucl. Phys.* 59.1 (July 2007), pp. 432–445. DOI: 10.1016/J.PPNP.2007.01.022.

[18] J. Okołowicz, M. Płoszajczak, and I. Rotter. "Dynamics of quantum systems embedded in a continuum". In: *Phys. Rep.* 374.4 (2003), pp. 271–383. DOI: 10.1016/S0370-1573(02)00366-6.

[19] T. Berggren. "On the use of resonant states in eigenfunction expansions of scattering and reaction amplitudes". In: *Nucl. Phys. A* 109.2 (1968), pp. 265–287. DOI: 10.1016/0375-9474(68)90593-9.

[20] G. Gamow. "Zur Quantentheorie des Atomkernes". In: *Z. Phys.* 51.3-4 (Mar. 1928), pp. 204–212. DOI: 10.1007/BF01343196/METRICS.

[21] A. Bohm and J. D. Dollard. *The Rigged Hilbert Space and Quantum Mechanics*. Vol. 78. Springer Berlin Heidelberg, 1978. DOI: 10.1007/3-540-088431-1.

[22] A. Bohm et al. "Quantum mechanical irrebersibility". In: *Phys. A: Stat. Mech. Appl.* 236.3-4 (Mar. 1997), pp. 485–549. DOI: 10.1016/S0378-4371(96)00284-1.

[23] R. De La Madrid. "The role of the rigged Hilbert space in quantum mechanics". In: *European Journal of Physics* 26.2 (Feb. 2005), p. 287. DOI: 10.1088/0143-0807/26/2/008.

[24] A. J. Siegert. "On the Derivation of the Dispersion Formula for Nuclear Reactions". In: *Physical Review* 56.8 (1939), pp. 750–752. DOI: 10.1103/PhysRev.56.750.

[25] H. C. Ohanian, C. G. Ginsburg, and A. J. Phys. "Antibound 'States' and Resonances". In: *American Journal of Physics* 42.4 (Apr. 1974), pp. 310–315. DOI: 10.1119/1.1987678.

[26] A. C. Dassie et al. "Illustrations of loosely bound and resonant states in atomic nuclei". In: *American Journal of Physics* 90 (2022), pp. 118–125. DOI: 10.1119/10.0007045.

[27] N. Michel et al. "Gamow shell model description of weakly bound nuclei and unbound nuclear states". In: *Phys. Rev. C* 67.5 (2003), p. 17. DOI: 10.1103/PhysRevC.67.054311.

[28] N. Michel, W. Nazarewicz, and M. Płoszajczak. "Proton-neutron coupling in the Gamow shell model: The lithium chain". In: *Phys. Rev. C* 70.6 (Dec. 2004), p. 064313. DOI: 10.1103/PHYSREVC.70.064313/.

[29] N. Michel et al. "Gamow Shell Model Description of Neutron-Rich Nuclei". In: *Phys. Rev. Lett.* 89.4 (2002), p. 042502. DOI: 10.1103/PHYSREVLETT.89.042502.

[30] N. Michel et al. "Antibound states and halo formation in the Gamow shell model". In: *Phys. Rev. C* 74.5 (Nov. 2006), p. 054305. DOI: 10.1103/PHYSREVC.74.054305/.

[31] X. Mao et al. "Gamow-shell-model description of Li isotopes and their mirror partners". In: *Phys. Rev. C* 102.2 (2020), p. 24309. DOI: 10.1103/PhysRevC.102.024309.

[32] N. Michel, H. M. Aktulga, and Y. Jaganathen. "Toward scalable many-body calculations for nuclear open quantum systems using the Gamow Shell Model". In: *Computer Physics Communications* 247 (Feb. 2020), p. 106978. DOI: 10.1016/J.CPC.2019.106978.

[33] W. J. Romo. "Inner product for resonant states and shell-model applications". In: *Nucl. Phys. A* 116.3 (Aug. 1968), pp. 617–636. DOI: 10.1016/0375-9474(68)90395-3.

[34] O. Civitarese, M. Gadella, and R. I. Betan. "On the mean value of the energy for resonant states". In: *Nucl. Phys. A* 660.3 (Nov. 1999), pp. 255–266. DOI: 10.1016/S0375-9474(99)00405-4.

[35] H. Furutani, H. Horiuchi, and R. Tamagaki. "Structure of the Second $0^+$ State of $^4$He". In: *Progress of Theoretical Physics* 60.1 (July 1978), pp. 307–309. DOI: 10.1143/PTP.60.307.

[36] H. Furutani, H. Horiuchi, and R. Tamagaki. "Cluster-Model Study of the $T = 1$ States in $A = 4$ System: $^3He + p$ Scattering". In: *Prog. of Theor. Phys.* 62.4 (Oct. 1979), pp. 981–1002. DOI: 10.1143/PTP.62.981.

[37] Y. Jaganathen et al. "Quantified Gamow shell model interaction for *psd*-shell nuclei". In: *Phys. Rev. C* 96 (5 Nov. 2017), p. 054316. DOI: 10.1103/PhysRevC.96.054316.

[38] A. Mercenne, N. Michel, and M. Płoszajczak. "Gamow shell model description of $^4$He$(d, d)$ elastic scattering reactions". In: *Phys. Rev. C* 99.4 (Apr. 2019), p. 044606. DOI: 10.1103/PHYSREVC.99.044606/.

[39] M. D. Jones et al. "Search for excited states in $^{25}$O". In: *Phys. Rev. C* 96.5 (Nov. 2017), p. 054322. DOI: 10.1103/PHYSREVC.96.054322/.

[40] K. Fossez, J. Rotureau, and W. Nazarewicz. "Energy spectrum of neutron-rich helium isotopes: Complex made simple". In: *Phys. Rev. C* 98.6 (2018), pp. 1–6. DOI: 10.1103/PhysRevC.98.061302.

[41] R. J. Furnstahl and A. Schwenk. "How should one formulate, extract and interpret 'non-observables' for nuclei?" In: *J. Phys. G* 37.6 (Mar. 2010), p. 064005. DOI: 10.1088/0954-3899/37/6/064005.

[42] G. Racah. "Theory of Complex Spectra. II". In: *Phys. Rev.* 62 (9-10 Nov. 1942), pp. 438–462. DOI: 10.1103/PhysRev.62.438.

[43] P. Hansen and J. Tostevin. "Direct Reactions with Exotic Nuclei". In: *Ann. Rev. Nucl. Part. Sci.* 53.1 (2003), pp. 219–261. DOI: 10.1146/annurev.nucl.53.041002.110406.

[44] J. A. Tostevin and A. Gade. "Updated systematics of intermediate-energy single-nucleon removal cross sections". In: *Phys. Rev. C* 103 (5 May 2021), p. 054610. DOI: 10.1103/PhysRevC.103.054610.

[45] T. Aumann et al. "Quenching of single-particle strength from direct reactions with stable and rare-isotope beams". In: *Prog. Part. Nucl. Phys.* 118 (2021), p. 103847. DOI: 10.1016/j.ppnp.2021.103847.

[46] J. Wylie et al. "Spectroscopic factors in dripline nuclei". In: *Phys. Rev. C* 104 (6 Dec. 2021), p. L061301. DOI: 10.1103/PhysRevC.104.L061301.

[47] A. Gade et al. "Reduction of spectroscopic strength: Weakly-bound and strongly-bound single-particle states studied using one-nucleon knockout reactions". In: *Phys. Rev. C* 77 (4 Apr. 2008), p. 044306. DOI: 10.1103/PhysRevC.77.044306.

[48] J. A. Tostevin and A. Gade. "Systematics of intermediate-energy single-nucleon removal cross sections". In: *Phys. Rev. C* 90 (5 Nov. 2014), p. 057602. DOI: 10.1103/PhysRevC.90.057602.

[49] R. J. Charity, L. G. Sobotka, and J. A. Tostevin. "Single-nucleon knockout cross sections for reactions producing resonance states at or beyond the drip line". In: *Phys. Rev. C* 102 (4 Oct. 2020), p. 044614. DOI: 10.1103/PhysRevC.102.044614.

[50] A. Gade et al. "Reduced Occupancy of the Deeply Bound $0d_{5/2}$ Neutron State in $^{32}$Ar". In: *Phys. Rev. Lett.* 93 (4 July 2004), p. 042501. DOI: 10.1103/PhysRevLett.93.042501.

[51] C. Hebborn, F. M. Nunes, and A. E. Lovell. "New Perspectives on Spectroscopic Factor Quenching from Reactions". In: *Phys. Rev. Lett.* 131.21 (Nov. 2023), p. 212503. DOI: 10.1103/PHYSREVLETT.131.212503/.

[52] C. Hebborn, F. M. Nunes, and A. E. Lovell. "Erratum: New Perspectives on Spectroscopic Factor Quenching from Reactions [Phys. Rev. Lett. 131, 212503 (2023)". In: *Phys. Rev. Lett.* 132.13 (Mar. 2024), p. 139901. DOI: 10.1103/PHYSREVLETT.132.139901/.

[53] K. Riisager. "Halos and related structures". In: *Physica Scripta* 2013.T152 (Jan. 2013), p. 014001. DOI: 10.1088/0031-8949/2013/T152/014001.

[54] N. Michel, W. Nazarewicz, and M. Płoszajczak. "Threshold effects in multichannel coupling and spectroscopic factors in exotic nuclei". In: *Phys. Rev. C* 75.3 (Mar. 2007), p. 031301. DOI: 10.1103/PhysRevC.75.031301.

[55] N. Michel, W. Nazarewicz, and M. Płoszajczak. "Continuum coupling and single-nucleon overlap integrals". In: *Nucl. Phys. A* 794.1 (2007), pp. 29–46. DOI: 10.1016/j.nuclphysa.2007.07.004.

[56] Y. Tosaka and Y. Suzuki. "Structure of $^{11}$Li in the cluster-orbital shell model for the $^{9}$Li+$n$+$n$ system". In: *Nucl. Phys. A* 512.1 (May 1990), pp. 46–60. DOI: 10.1016/0375-9474(90)90003-5.

[57] P. Descouvemont. "Simultaneous study of the $^{11}$Li and $^{10}$Li nuclei in a microscopic cluster model". In: *Nucl. Phys. A* 626.3 (Nov. 1997), pp. 647–668. DOI: 10.1016/S0375-9474(97)00504-6.

[58] I. Brida, F. M. Nunes, and B. A. Brown. "Effects of deformation in the three-body structure of $^{11}$Li". In: *Nucl. Phys. A* 775.1-2 (Aug. 2006), pp. 23–34. DOI: 10.1016/J.NUCLPHYSA.2006.06.012.

[59] B. A. Brown et al. "Motivations for Early High-Profile FRIB Experiments". In: (Oct. 2024). URL: https://arxiv.org/abs/2410.06144v1.

[60] O. B. Tarasov et al. "Observation of New Isotopes in the Fragmentation of $^{198}$Pt at FRIB". In: *Phys. Rev. Lett.* 132.7 (Feb. 2024), p. 072501. DOI: 10.1103/PHYSREVLETT.132.072501.

[61] M. Thoennessen. "Reaching the limits of nuclear stability". In: *Reports on Progress in Physics* 67.7 (June 2004), p. 1187. DOI: 10.1088/0034-4885/67/7/R04.

[62] R. J. Charity et al. "Strong evidence for $^{9}$N and the limits of existence of atomic nuclei". In: *Phys. Rev. Lett.* 131.17 (Sept. 2023), p. 172501. DOI: https://doi.org/10.1103/PhysRevLett.131.172501.

[63] K. Fossez et al. "Nuclear rotation in the continuum". In: *Phys. Rev. C* 93.1 (Jan. 2016), p. 011305. DOI: 10.1103/PHYSREVC.93.011305/.

[64] M. Pfützner et al. "Radioactive decays at limits of nuclear stability". In: *Reviews of Modern Physics* 84.2 (Apr. 2012), pp. 567–619. DOI: 10.1103/REVMODPHYS.84.567/.

[65] M. Pfützner, I. Mukha, and S. M. Wang. "Two-proton emission and related phenomena". In: *Prog. Part. Nucl. Phys.* 123 (2023), p. 104050. DOI: 10.1016/j.ppnp.2023.104050.

[66] L. Neufcourt et al. "Beyond the proton drip line: Bayesian analysis of proton-emitting nuclei". In: *Phys. Rev. C* 101.1 (Jan. 2020), p. 014319. DOI: 10.1103/PHYSREVC.101.014319/.

[67] R. J. Charity et al. "Investigations of three-, four-, and five-particle decay channels of levels in light nuclei created using a $^{9}C$ beam". In: *Phys. Rev. C* 84.1 (July 2011), p. 014320. DOI: 10.1103/PHYSREVC.84.014320/.

[68] R. J. Charity et al. "Observation of the Exotic Isotope $^{13}$F Located Four Neutrons beyond the Proton Drip Line". In: *Phys. Rev. Lett.* 126 (13 Mar. 2021), p. 132501. DOI: 10.1103/PhysRevLett.126.132501.

[69] K. W. Brown et al. "Proton-decaying states in light nuclei and the first observation of $^{17}$Na". In: *Phys. Rev. C* 95.4 (Apr. 2017), p. 044326. DOI: 10.1103/PHYSREVC.95.044326/.

[70] D. Kostyleva et al. "Towards the Limits of Existence of Nuclear Structure: Observation and First Spectroscopy of the Isotope $^{31}$K by Measuring Its Three-Proton Decay". In: *Phys. Rev. Lett.* 123.9 (Aug. 2019), p. 092502. DOI: 10.1103/PHYSREVLETT.123.092502/.

[71] R. J. Charity et al. "$2p-2p$ decay of $^{8}$C and isospin-allowed $2p$ decay of the isobaric-analog state in 8B". In: *Phys. Rev. C* 82.4 (Oct. 2010), p. 041304. DOI: 10.1103/PHYSREVC.82.041304/.

[72] Y. Jin et al. "First Observation of the Four-Proton Unbound Nucleus $^{18}$Mg". In: *Phys. Rev. Lett.* 127.26 (Dec. 2021), p. 262502. DOI: 10.1103/PHYSREVLETT.127.262502/.

[73] A. M. Mukhamedzhanov et al. "Bound, virtual, and resonance S-matrix poles from the Schrödinger equation". In: *Phys. Rev. C* 81.5 (May 2010), p. 054314. DOI: 10.1103/PHYSREVC.81.054314.

[74] V. A. Babenko and N. M. Petrov. "Low-energy parameters of neutron-neutron interaction in the effective-range approximation". In: *Physics of Atomic Nuclei* 76.6 (June 2013), pp. 684–689. DOI: 10.1134/S1063778813060033/METRICS.

[75] L. P. Kok. "Accurate Determination of the Ground-State Level of the $^2$He Nucleus". In: *Phys. Rev. Lett.* 45.6 (Aug. 1980), p. 427. DOI: 10.1103/PhysRevLett.45.427.

[76] R. J. Charity and L. G. Sobotka. "Invariant-mass spectroscopy in projectile fragmentation reactions". In: *Phys. Rev. C* 108.4 (Oct. 2023), p. 044318. DOI: 10.1103/PHYSREVC.108.044318/.

[77] T. Al Kalanee et al. "Structure of unbound neutron-rich $^9$He studied using single-neutron transfer". In: *Phys. Rev. C* 88.3 (Sept. 2013), p. 034301. DOI: 10.1103/PHYSREVC.88.034301/.

[78] H. G. Bohlen et al. "Spectroscopy of $^9$He with the ($^{13}C$,$^{13}O$)-reaction on $^9$Be". In: *Z. Phys. A* 330.2 (June 1988), pp. 227–228. DOI: 10.1007/BF01293402/METRICS.

[79] D. Votaw et al. "Low-lying level structure of the neutron-unbound $N = 7$ isotones". In: *Phys. Rev. C* 102.1 (July 2020), p. 014325. DOI: 10.1103/PHYSREVC.102.014325/.

[80] L. Chen et al. "Evidence for an $\ell = 0$ ground state in $^9$He". In: *Phys. Lett. B* 505.1-4 (Apr. 2001), pp. 21–26. DOI: 10.1016/S0370-2693(01)00313-6.

[81] M. S. Golovkov et al. "New insight into the low-energy $^9$He spectrum". In: *Phys. Rev. C* 76.2 (Aug. 2007), p. 021605. DOI: 10.1103/PHYSREVC.76.021605/.

[82] H. T. Johansson et al. "The unbound isotopes $^{9,10}$He". In: *Nucl. Phys. A* 842.1-4 (Oct. 2010), pp. 15–32. DOI: 10.1016/J.NUCLPHYSA.2010.04.006.

[83] T. Aumann et al. "One-Neutron Knockout from Individual Single-Particle States of $^{11}$Be". In: *Phys. Rev. Lett.* 84.1 (Jan. 2000), p. 35. DOI: 10.1103/PhysRevLett.84.35.

[84] S. M. Wang et al. "Structure and decay of the extremely proton-rich nuclei $^{11,12}$O". In: *Phys. Rev. C* 99.54302 (May 2019). DOI: 10.1103/PHYSREVC.99.054302.

[85] N. Michel et al. "Shell model description of nuclei far from stability". In: *Acta Physica Polonica B* 35 (2004), pp. 1249–1261.

[86] A. Mercenne et al. "Gamow shell model description of the $^{40}$Ca$(d, p)$ transfer reaction". In: *Phys. Rev. C* 107.1 (Jan. 2023), p. L011603. DOI: 10.1103/PHYSREVC.107.L011603/.

[87] J. Rotureau, J. Okołowicz, and M. Płoszajczak. "Theory of the two-proton radioactivity in the continuum shell model". In: *Nucl. Phys. A* 767.1-4 (2006), pp. 13–57. DOI: 10.1016/j.nuclphysa.2005.12.005.

[88] H. Feshbach. "Unified theory of nuclear reactions". In: *Annals of Physics* 5.4 (Dec. 1958), pp. 357–390. DOI: 10.1016/0003-4916(58)90007-1.

[89] H. Feshbach. "A unified theory of nuclear reactions. II". In: *Annals of Physics* 19.2 (Aug. 1962), pp. 287–313. DOI: 10.1016/0003-4916(62)90221-X.

[90] K. Bennaceur et al. "A study of nuclei of astrophysical interest in the continuum shell model". In: *J. Phys. G* 24.8 (Aug. 1998), p. 1631. DOI: 10.1088/0954-3899/24/8/043.

[91] K. Bennaceur et al. "Study of the $^{7}$Be(p, $\gamma$)$^{8}$B and $^{7}$Li($n$, $\gamma$)$^{8}$Li capture reactions using the shell model embedded in the continuum". In: *Nucl. Phys. A* 651.3 (May 1999), pp. 289–319. DOI: 10.1016/S0375-9474(99)00133-5.

[92] K. Bennaceur et al. "Analysis of the $^{16}$O(p,$\gamma$)$^{17}$F capture reaction using the shell model embedded in the continuum". In: *Nucl. Phys. A* 671.1 (2000), pp. 203–232. DOI: https://doi.org/10.1016/S0375-9474(99)00851-9.

[93] J. Okołowicz, M. Płoszajczak, and W. Nazarewicz. "Convenient Location of a Near-Threshold Proton-Emitting Resonance in $^{11}$B". In: *Phys. Rev. Lett.* 124.4 (2020), pp. 1–5. DOI: 10.1103/PhysRevLett.124.042502.

[94] J. Okołowicz, M. Płoszajczak, and W. Nazarewicz. "$\beta$=$p$ and $\beta-\alpha$ decay of the $^{11}$Be neutron halo ground state". In: *J. Phys. G* 49.10 (Aug. 2022), 10LT01. DOI: 10.1088/1361-6471/AC8948.

[95] J. Okołowicz, M. Płoszajczak, and W. Nazarewicz. "On the origin of nuclear clustering". In: *Progress of Theoretical Physics Supplement* 196.196 (Oct. 2012), pp. 230–243. DOI: 10.1143/PTPS.196.230/5342456/196-230.PDF.

[96] P. O. Löwdin. "Quantum Theory of Many-Particle Systems. I. Physical Interpretations by Means of Density Matrices, Natural Spin-Orbitals, and Convergence Problems in the Method of Configurational Interaction". In: *Physical Review* 97.6 (Mar. 1955), p. 1474. DOI: 10.1103/PhysRev.97.1474.

[97] H. Horiuchi. "Chapter III. Kernels of GCM, RGM and OCM and Their Calculation Methods". In: *Progress of Theoretical Physics Supplement* 62 (Feb. 1977), pp. 90–190. DOI: 10.1143/PTPS.62.90.

[98] F. Plasser et al. "Efficient and Flexible Computation of Many-Electron Wave Function Overlaps". In: *Journal of Chemical Theory and Computation* 12.3 (2016), pp. 1207–1219. DOI: 10.1021/acs.jctc.5b01148.

[99] D. J. Griffiths and D. F. Schroeter. *Introduction to Quantum Mechanics*. Third. Cambridge University Press, 2018. DOI: 10.1017/9781316995433.

[100] D. H. McIntyre. *Quantum Mechanics: A Paradigms Approach*. Cambridge University Press, Sept. 2022. DOI: 10.1017/9781009310598.

[101] G. Hagen, M. Hjorth-Jensen, and N. Michel. "Gamow shell model and realistic nucleon-nucleon interactions". In: *Phys. Rev. C* 73.6 (June 2006), p. 064307. DOI: 10.1103/PHYSREVC.73.064307/.

[102] J. Rotureau and ·. U. Van Kolck. "Effective Field Theory and the Gamow Shell Model". In: *Few-Body Syst* 54 (2012), pp. 725–735. DOI: 10.1007/s00601-012-0455-6.

[103] M. V. Zhukov et al. "Bound state properties of Borromean halo nuclei: $^{6}$He and $^{11}$Li". In: *Physics Reports* 231.4 (Aug. 1993), pp. 151–199. DOI: 10.1016/0370-1573(93)90141-Y.

[104] N. Michel et al. "Open problems in the theory of nuclear open quantum systems". In: *J. Phys. G* 37.6 (2010), pp. 1–14. DOI: 10.1088/0954-3899/37/6/064042.

[105] E. P. Wigner. "On the Behavior of Cross Sections Near Thresholds". In: *Physical Review* 73.9 (May 1948), p. 1002. DOI: 10.1103/PhysRev.73.1002.

[106] J. P. Fernandez et al. "Description of $^{7}$Be and $^{7}$Li within the Gamow shell model". In: *Phys. Rev. C* 108.4 (Oct. 2023), p. 044616. DOI: 10.1103/PHYSREVC.108.044616/.

[107] J. Wylie et al. "Nuclear Beavers". In: *Under Review* (2025).

[108] Z. Constan. "Learning Nuclear Science with Marbles The Physics Teacher". In: *The Physics Teacher* 48 (2010), p. 377. DOI: 10.1119/1.3293660.

[109] J. Whittaker. "Hands-On Nuclear Physics". In: *The Physics Teacher* 51 (2013), p. 166. DOI: 10.1119/1.4792015.

[110] J. Wylie and K. Godbey. *Nuclear Building Blocks at http://shellmodel.ascsn.net/*. 2024. URL: http://shellmodel.ascsn.net/.

[111] M. G. Mayer. "On Closed Shells in Nuclei. II". In: *Physical Review* 75.12 (June 1949), p. 1969. DOI: 10.1103/PhysRev.75.1969.